SANDIA REPORT

SAND2014-18260
Unlimited Release
September 2014

Crystalline Nanoporous Frameworks: a Nanolaboratory for Probing Excitonic Device Concepts

Mark D. Allendorf, Jason D. Azoulay, Alexandra C. Ford, Michael E. Foster, Farid El Gabaly, François Léonard, Kirsty Leong, Vitalie Stavila, A. Alec Talin, Bryan M. Wong, Michael T. Brumbach, D. Van Gough, Timothy N. Lambert, Mark A. Rodriguez, Erik D. Spoerke, David R. Wheeler, Joseph C. Deaton, Andrea Centrone, Paul Haney, R. Adam Kinney, Veronika Szalai, Heayoung P. Yoon.

Prepared by
Sandia National Laboratories
Albuquerque, New Mexico 87185 and Livermore, California 94550

Sandia National Laboratories

Issued by Sandia National Laboratories, operated for the United States Department of Energy by Sandia Corporation.

NOTICE: This report was prepared as an account of work sponsored by an agency of the United States Government. Neither the United States Government, nor any agency thereof, nor any of their employees, nor any of their contractors, subcontractors, or their employees, make any warranty, express or implied, or assume any legal liability or responsibility for the accuracy, completeness, or usefulness of any information, apparatus, product, or process disclosed, or represent that its use would not infringe privately owned rights. Reference herein to any specific commercial product, process, or service by trade name, trademark, manufacturer, or otherwise, does not necessarily constitute or imply its endorsement, recommendation, or favoring by the United States Government, any agency thereof, or any of their contractors or subcontractors. The views and opinions expressed herein do not necessarily state or reflect those of the United States Government, any agency thereof, or any of their contractors.

Printed in the United States of America. This report has been reproduced directly from the best available copy.

Available to DOE and DOE contractors from
U.S. Department of Energy
Office of Scientific and Technical Information
P.O. Box 62
Oak Ridge, TN 37831

Telephone: (865) 576-8401
Facsimile: (865) 576-5728
E-Mail: reports@adonis.osti.gov
Online ordering: http://www.osti.gov/bridge

Available to the public from
U.S. Department of Commerce
National Technical Information Service
5285 Port Royal Rd.
Springfield, VA 22161

Telephone: (800) 553-6847
Facsimile: (703) 605-6900
E-Mail: orders@ntis.fedworld.gov
Online order: http://www.ntis.gov/help/ordermethods.asp?loc=7-4-0#online

SAND2014-18260
Unlimited Release
September 2014

Crystalline Nanoporous Frameworks: a Nanolaboratory for Probing Excitonic Device Concepts

Mark D. Allendorf, Jason D. Azoulay, Alexandra C. Ford, Michael E. Foster, Farid El Gabaly,
François Léonard, Kirsty Leong, Vitalie Stavila, A. Alec Talin
Sandia National Laboratories, Livermore, CA 94551-0969

Bryan M. Wong
Department of Chemical and Environmental Engineering
University of California Riverside
Riverside, CA 92521-0144

Michael T. Brumbach, D. Van Gough, Timothy N. Lambert, Mark A. Rodriguez, Erik D.
Spoerke, David R. Wheeler
Sandia National Laboratories, Albuquerque, NM 87185-1411

Joseph C. Deaton
Department of Chemistry, North Carolina State University, Raleigh, NC 27965

Paul Haney, Veronika Szalai, Andrea Centrone, R. Adam Kinney, Heayoung P. Yoon
Center for Nanoscale Science and Technology
National Institute of Standards and Technology, Gaithersburg, MD 20899

Andrea Centrone, R. Adam Kinney, Heayoung P. Yoon
Maryland Nanocenter
University of Maryland, College Park, MD 20742

Abstract

Electro-optical organic materials hold great promise for the development of high-efficiency devices based on exciton formation and dissociation, such as organic photovoltaics (OPV) and organic light-emitting devices (OLEDs). However, the external quantum efficiency (EQE) of both OPV and OLEDs must be improved to make these technologies economical. Efficiency rolloff in OLEDs and inability to control morphology at key OPV interfaces both reduce EQE. Only by creating materials that allow manipulation and control of the intimate assembly and communication between various nanoscale excitonic components can we hope to first understand

and then engineer the system to allow these materials to reach their potential. The aims of this proposal are to: 1) develop a paradigm-changing platform for probing excitonic processes composed of Crystalline Nanoporous Frameworks (CNFs) infiltrated with secondary materials (such as a complimentary semiconductor); 2) use them to probe fundamental aspects of excitonic processes; and 3) create prototype OPVs and OLEDs using infiltrated CNF as active device components. These functional platforms will allow detailed control of key interactions at the nanoscale, overcoming the disorder and limited synthetic control inherent in conventional organic materials. CNFs are revolutionary inorganic-organic hybrid materials boasting unmatched synthetic flexibility that allow tuning of chemical, geometric, electrical, and light absorption/generation properties. For example, bandgap engineering is feasible and polyaromatic linkers provide tunable photon antennae; rigid 1-5 nm pores provide an oriented, intimate host for triplet emitters (to improve light emission in OLEDs) or secondary semiconducting polymers (creating a charge-separation interface in OPV). These atomically engineered, ordered structures will enable critical fundamental questions to be answered concerning charge transport, nanoscale interfaces, and exciton behavior that are inaccessible in disordered systems. Implementing this concept also creates entirely new dimensions for device fabrication that could both improve performance, increase durability, and reduce costs with unprecedented control of over properties.

This report summarizes the key results of this project and is divided into sections based on publications that resulted from the work. We begin in Section 2 with an investigation of light harvesting and energy transfer in a MOF infiltrated with donor and acceptor molecules of the type typically used in OPV devices (thiophenes and fullerenes, respectively). The results show that MOFs can provide multiple functions: as a light harvester, as a stabilizer and organizer or the infiltrated molecules, and as a facilitator of energy transfer. Section 3 describes computational design of MOF linker groups to accomplish light harvesting in the visible and facilitate charge separation and transport. The predictions were validated by UV-visible absorption spectroscopy, demonstrating that rational design of MOFs for light-harvesting purposes is feasible. Section 4 extends the infiltration concept discussed in Section to, which we now designate as “Molecule@MOF” to create an electrically conducting framework. The tailorability and high conductivity of this material are unprecedented, meriting publication in the journal *Science* and spawning several Technical Advances. Section 5 discusses processes we developed for depositing MOFs as thin films on substrates, a critical enabling technology for fabricating MOF-based electronic devices. Finally, in Section 6 we summarize results showing that a MOF thin film can be used as a sensitizer in a DSSC, demonstrating that MOFs can serve as active layers in excitonic devices. Overall, this project provides several crucial proofs-of-concept that the potential of MOFs for use in optoelectronic devices that we predicted several years ago [3] can be realized in practice.

CONTENTS

FIGURES

TABLES

1. INTRODUCTION

Electro-optical organic materials hold great promise for the development of high-efficiency energy harvesting technologies, such as organic photovoltaics (OPV) [1] and dye-sensitized solar cells (DSSC).[2] Both technologies involve formation of an exciton (a bound excited-state electron-hole pair) by light absorption. Photocurrent generation occurs when the exciton splits at the interface between two semiconductors or when an electron is injected into a semiconducting oxide (typically TiO_2) in a DSSC. Advances in nanoscale materials and enhanced understanding of component interactions in PV have led to impressive improvements in efficiency. However, lack of control at key interfaces contributes to low open circuit voltages (V_{OC}) and high dark current, both of which reduce power conversion efficiency. It is now clear that nanoscale and molecular interactions in these systems control intrinsic properties such as work function, band gap, and carrier mobility, but also that intermolecular forces, disorder at material interfaces, and non-uniform morphologies and chromophore environments strongly affect light harvesting, exciton formation/dissociation, carrier recombination, and charge transport (CT). Consequently, it is very difficult to define a clear pathway to improvement. Only by creating materials that allow manipulation and control of the intimate assembly and communication between nanoscale excitonic components can we hope to first understand intrinsic properties and then tailor the system to optimize their performance.

Both fundamental probing of excitonic phenomena and significant improvements to exciton-based organic electronics are inhibited by the limitations of conventional material systems. Ideally, one would like the structural and synthetic flexibility to allow factors such as band alignment, intermolecular energy transfer, interface creation, and exciton diffusion distance to be independently tuned. This is extremely difficult to accomplish; for example, phase-separation methods commonly used to organize and assemble polymer blends in bulk heterojunction (BHJ) technologies lead to dead ends and interfacial morphologies that impede exciton diffusion and charge collection. Alternatively, current top-down methods intended to create highly ordered structures cannot uniformly reduce exciton diffusion distances to < 10 nm.[1] On a molecular level, rational design of energy transfer is very difficult to accomplish because of poorly defined local environments, and modifications to interacting groups (e.g. donor/acceptor (D/A) combinations such as P3HT/PCBM in OPV) to improve their properties may also change polymer or crystal packing, altering intermolecular interactions in unpredictable ways that affect critical properties such as color purity, charge balance, dark current, and V_{OC}. As a result, the relationship between nanoscale features and device performance are yet to be definitively determined.

The aims of this proposal are to: 1) develop a paradigm-changing platform for probing excitonic processes composed of Crystalline Nanoporous Frameworks (CNFs) infiltrated with secondary materials (such as a complimentary semiconductor); 2) use them to probe fundamental aspects of excitonic processes; and 3) perform a proof-of-concept demonstration of photocurrent using infiltrated CNF as the active components. By “platform” we mean the integrated CNF plus infiltrated components, which comprise a synthetically versatile hybrid. These platforms will allow detailed control of key interactions at the nanoscale, overcoming the disorder and limited synthetic control inherent in conventional PV materials. CNF are a revolutionary class of materials: highly ordered, inorganic-organic hybrids, they have unmatched synthetic flexibility, allowing tuning of chemical structure, electronic properties, and pore dimensions. We use this term here as a more general designation of a broad class of materials. However, for this project, the most relevant subcategory is metal-organic frameworks (MOFs), which have permanent porosity (0.5 – ~10 nm diameters). Organic ligands (also known as "linkers") serve as both structure-directing elements and to impart specialized properties such as luminescence and selective molecular adsorption. MOFs allow straightforward modification of intermolecular separation and orientation, so that excitonic interfaces created within them can be tuned. These properties could, for example, dramatically improve charge collection by creating donor-acceptor interfaces that are well within the exciton diffusion length (~ 10 nm in organic materials), increase the density of these within the absorption depth of light by orders of magnitude over traditional bulk heterojunction devices, and optimize D-A orientation for efficient energy transfer. Although MOFs are under intense investigation for applications such as gas storage and separations, their use in optoelectronic applications has received almost no attention. As part of this project, we recently reviewed the status of this aspect of MOF science.

This report summarizes the key results of this project and is divided into sections based on publications that resulted from the work. We begin in Section 2 with an investigation of light harvesting and energy transfer in a MOF infiltrated with donor and acceptor molecules of the type typically used in OPV devices (thiophenes and fullerenes, respectively). The results show that MOFs can provide multiple functions: as a light harvester, as a stabilizer and organizer or the infiltrated molecules, and as a facilitator of energy transfer. Section 3 describes computational design of MOF linker groups to accomplish light harvesting in the visible and facilitate charge separation and transport. The predictions were validated by UV-visible absorption spectroscopy, demonstrating that rational design of MOFs for light-harvesting purposes is feasible. Section 4 extends the infiltration concept discussed in Section to, which we now designate as "Molecule@MOF" to create an electrically conducting framework. The tailorability and high conductivity of this material are unprecedented, meriting publication in the journal *Science* and spawning several Technical Advances. Section 5 discusses processes we developed for depositing MOFs as thin films on substrates, a critical enabling technology for fabricating MOF-based electronic devices. Finally, in Section 6 we summarize results showing that a MOF thin film can be used as a sensitizer in a DSSC, demonstrating that MOFs can serve as active layers in excitonic devices. Overall, this project provides several crucial proofs-of-concept that the potential of MOFs for use in optoelectronic devices that we predicted several years ago [3] can be realized in practice.

2. ENERGY AND CHARGE TRANSFER BY DONOR-ACCEPTORS PAIRS CONFINED IN A METAL-ORGANIC FRAMEWORK: A SPECTROSCOPIC AND COMPUTATIONAL INVESTIGATION

2.1. Introduction

Organic photovoltaics (OPVs) are excitonic devices in which the absorption of light by an organic semiconductor with a low dielectric constant generates bound electron-hole pairs (excitons) that are subsequently dissociated in a charge transfer (CT) event at the interface with a second, electron-accepting organic semiconductor. The mechanism of charge separation in polymeric bulk hetero-junction photovoltaic cells is described as electron transfer from the absorbing polymer to an electron acceptor via an excited D^{+}-A^{-} CT state,[4] potentially involving resonance energy transfer (RET) between the donor and acceptor.[5, 6] Two factors limiting the performance efficiency of OPV devices are the nature of the donor-acceptor (D-A) interface and the exciton diffusion length, which in conjugated polymers is typically < 10 nm before recombination occurs.[7] Much OPV research is directed toward ensuring that the D-A materials form continuous nanoscale networks within the entire photoactive layer, that their interfacial area is maximized, and that they have the proper orientation for efficient exciton splitting.[8-10],[11] A nanoscale interpenetrating network with crystalline order of both constituents is, therefore, a desirable architecture for the active layer in photovoltaic devices.[12, 13] Unfortunately, control over both the intermolecular (D-A) and meso (exciton diffusion) length scales is difficult to achieve in conventional bulk heterojunctions due to the inherent disorder of polymeric and/or molecular species in a (typically) amorphous matrix. Further complicating this situation is the need for proper alignment of the D and A electronic bands to enable efficient harvesting of the solar spectrum as well as exciton splitting[14], which limits further modification of the chemical structure of D and A to promote local ordering.

Metal-organic frameworks (MOFs) are crystalline nanoporous materials that offer a new approach to solving these challenging problems. MOFs are a class of hybrid supramolecular materials formed from metal cations or clusters serving as “nodes” connected to multi-topic, electron-donating organic ligands, creating ordered networks with permanent nanoporosity.[15-17] MOFs possess three critical properties relevant to controlling donor-acceptor interfaces. First, they are crystalline materials, which create a highly ordered and well-defined structure in which the position of all framework atoms is known with sub-angstrom precision. Second, they incorporate both inorganic and organic components, providing an unprecedented ability to tune the electronic structure. This also enables the pore size and chemical environment to be tailored; a number of isoreticular series are now known that enable systematic variation of structural and chemical properties.[18-20] Third, the rigid MOF structure creates permanent nano-porosity (1 – 10 nm diameter), which enables the fabrication of hybrid composites by filling the pores with guest molecules. Conceivably, D-A pairs could be co-located within a highly ordered, well-characterized structure. The high degree of organic linker ordering achievable within crystalline MOFs therefore provides a basis for systematically relating structure and composition to photon capture, energy transport, and delivery.[21]

The vast majority of MOFs are dielectric materials with wide band gaps.[22-25] This suggests that MOFs can serve as passive hosts to maintain close proximity and proper intermolecular alignment between donor and acceptor for efficient energy or charge transfer. In addition, however, many frameworks display linker-based luminescence,[26] enabling the framework to function as a photon antenna that increases light absorption. This concept was recently demonstrated using a pillared-paddlewheel MOF in which linker-to-linker energy transfer enabling broad coverage of the visible spectrum.[21] Lin and co-workers also reported facile intracrystal site-to-site energy migration dynamics in Ru(II)/Os(II) (2,2′-bipyridine)$_3$-based MOFs through luminescence quenching measurements.[27-29] Jin and co-workers reported an enhancement of light harvesting via energy transfer from QDs (coated on the surface of the framework) to the MOFs.[30] These works show the potential of appropriately designed MOFs functioning as light-harvesting and energy-transport structures.

Energy transfer involving guest molecules within the MOF pores is also feasible, as shown by Streit et al. using MOF thin film loaded with a europium β-diketonate complex.[31] These authors assumed that Dexter energy transfer was occurring, although no evidence for a ground-state complex required by this mechanism was provided. Nevertheless, they pointed out that efficient energy transfer by this quantum-mechanical effect requires the donor HOMO and acceptor LUMO to be energetically matched. Reasoning from these results, we hypothesized that MOFs could be used to overcome critical problems associated with the classical bulk heterojunction as a result of the following features. First, confinement within the pores allows donor-acceptor separations that are within critical distances at three key length scales important to efficient energy and/or charge transfer: 1) the exciton diffusion distance (typically $\leq$ 10 nm for organic materials); 2) the Förster radius for classical fluorescence resonance energy transfer (FRET; ~ 5 nm for many fluorescent molecules); and 3) the π-stacking distance (~ 3.5 Å) for Dexter energy transfer. Second, proper alignment of the donor and acceptor orbitals with the MOF band structure, which is essential for efficient energy or charge transfer regardless of the mechanism, can be achieved by tuning the MOF linker and/or metal ion. This tunability can also promote efficient use of the solar spectrum by allowing the band gap of semiconducting MOFs to be adjusted. Finally, the co-location of donor and acceptor eliminates problems associated with phase segregation, which in bulk heterojunctions reduce efficiency by creating dead ends or disordered boundaries between materials that quench excitons or trap charge.

Here, we describe an important step toward realizing the use of MOFs as components of OPV active layers, presenting spectroscopic data and electronic structure calculations demonstrating that the advantages described above can be realized using a MOF that functions as both a host for immobilizing donor and acceptor molecules and a photon antenna to scavenge and transfer energy to these guest species. As donor and acceptor we selected two molecules representative of those typically used in bulk heterojunctions: as acceptor, α,ω-Dihexylsexithiophene (DH6T), a thiophene oligomer similar to the polymer P3HT, and as donor, [6,6]-phenyl-C_{61}-butyric acid methyl ester (PCBM), among the most effective acceptors used in OPV active layers. Obtaining significant loading levels with either of these large molecules requires a MOF with large pores, so we selected MOF-177, which can accommodate large polycyclic organic dye molecules and C_{60}.[32] This MOF has a 1-D channel and one unique cavity (9:4 ratio), labeled channel A and cavity B in Figure 1. The diameters of these pores are approximately 14 Å for channel A and 24 Å for cavity B and can accommodate individual donor or acceptor molecules, placing them in close proximity to each other, but preventing phase segregation. The resulting multi-molecular-MOF hybrid harvests energy and efficiently transfers it to the infiltrated molecules.

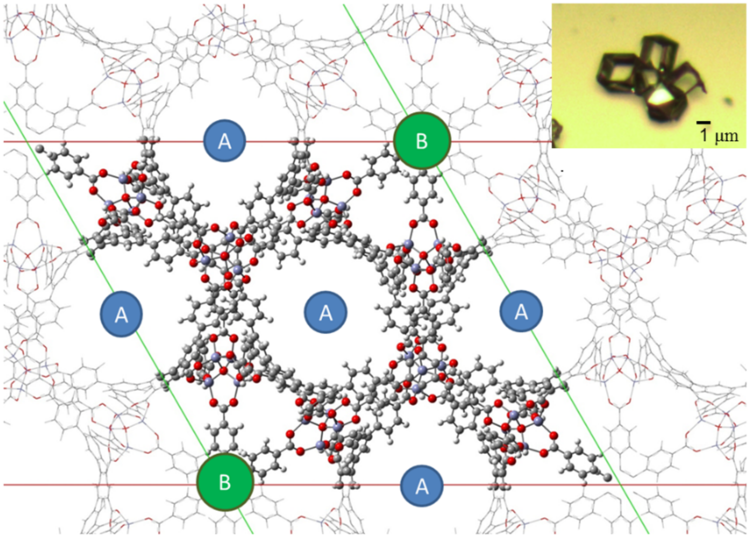

Figure 1. DFTB+ optimized structure shows 1-D pore channel (channel A) and a cavity (cavity B) (9:4 ratio). The insert shows an optical image of MOF-177 crystals.

2.2. Experimental and computational methods

2.2.1. Electronic structure calculations.

The electronic and structural properties of MOF-177 were modeled using the self-consistent charge density-functional tight-binding[33-35] (SCC-DFTB) method. The SCC-DFTB method is an approximation to Kohn-Sham density functional theory (KS-DFT) utilizing a parameterized Hamiltonian Matrix; therefore, the accuracy of the method ultimately depends on the parameters (Slater-Koster files) used. This method was chosen for its balance between computational efficiency and accuracy. An efficient computational method is required to circumvent the large sizes of the MOF systems (1628+ atoms) considered which are computationally demanding for traditional DFT methods. Here, the Zn-X (X= H, C, N, O, S, and Zn)[36] and O-N-C-H[35] SCC-DFTB Slater-Koster files developed for metal-organic molecules and solids were used, which are well suited for modeling MOF-177. All SCC-DFTB calculations were carried out using the DFTB+ simulation package.[37]

A geometry optimization using periodic-boundary-conditions (PBC) was carried out on MOF-177 using SCC-DFTB and employing the Lennard-Jones dispersion correction within DFTB+. During the optimization both the cell and atom positions were relaxed until a maximum force component of 0.001 au was reached. A single gamma point was used for sampling the Brillouin zone during the optimization due to the large size of the unit cell. The k-space sampling was increased to a 3 x 3 x 3 grid to improve the accuracy of the total and partial density-of-states (DOS). SCC-DFTB calculations were also performed on isolated PCBM and DH6T molecules in 50 Å^3 boxes. These calculations enable direct comparison to the MOF's electronic properties.

Potential energy curves of the infiltration of MOF-177 with PCBM and DH6T were generated to determine whether infiltration is energetically favored. For PCBM infiltration, a slab consisting of approximately 50 Å of vacuum space (total cell length of 80 Å) in the z-direction was created from the optimized MOF-177 unit cell. For infiltration with DH6T, which is a longer molecule than PCBM, a 1 x 1 x 2 supercell slab was created with approximately 60 Å of vacuum space (total cell length of 120 Å) in the z-direction. To maintain proper atomic valences within the periodic slabs, the appropriate atoms were terminated with hydrogen atoms. The constructed slabs consisted of a total of 820 and 1628 atoms respectively. Finally, the atom positions within the slabs were optimized before adding the infiltrating molecule to the calculation. The centers-of mass of the infiltrating molecules were placed along an arbitrary axis passing through the small pore of MOF-177 (pore A, see Figure 1). The molecules were then translated in increments of 1 Å and rotated around this axis in increments of 15° and 30°, generating a total of 663 and 637 starting structures mapping the infiltration of PCBM and DH6T, respectively. Ten-step geometry optimizations were performed with SCC-DFTB to remove any close contacts that might have been created.

Time-dependent density functional theory (TDDFT) was employed to probe the interactions between the organic linker (H_3BTB) and PCBM and DH6T. These calculations were carried out using the range-separated wB97xD functional[38] and the 6-31G(d,p) valence double-zeta polarized basis set. This functional is a well-tested method for capturing van der Waals interactions and long-range charge-transfer, which are essential for this system. For consistency with experiment, a polarizable continuum model (PCM) was used to incorporate solvent effects of chloroform ($\varepsilon = 11.00$). Full ground-state geometry optimizations using the respective functional were performed for all complexes, followed by TDDFT (using the linear-response formalism) calculations considering the first 100 singlet excitations. All DFT and TDDFT calculations were performed with Gaussian 09[39] using the default convergence criteria.

2.2.2. MOF synthesis and infiltration.

All reagents, 2,2':5',2"-terthiophene (3T), 3,3'''-Dihexyl-2,2':5',2'':5'',2'''-quaterthiophene (DH-4T), and α,ω-Dihexylsexithiophene (DH6T) were purchased from Sigma-Aldrich (St. Louis, MO) and used as received unless stated otherwise. Phenyl-C_{61}-butyric acid methyl ester (PCBM) was purchased from American Dye Source (Quebec, Canada). Solvents used for MOF activation and exchange were stored over dried molecular sieves (4 Å).

MOF-177 was synthesized using a previously published protocol.[40] Briefly, zinc nitrate hexahydrate (0.368 g) and 4,4',4'-benzene-1,3,5-triyl-tribenzoic acid (H_3BTB) (0.180 g) were dissolved in DEF (10 mL) in a 20mL vial, capped tightly and heated to 100˚C for 20 hours. The solution was decanted and the crystals thoroughly washed with DMF, then exchanged with $CHCl_3$ for three days. The material was evacuated at 125˚C for 6 hours. MOF-177 crystals were infiltrated by soaking in saturated solutions of DH6T (1.0×10^{-4} M), PCBM (20mg/mL), or a mixture of 3T, DH-4T, or DH6T + PCBM in chlorobenzene for one week. After soaking for one week, the crystals were thoroughly washed and rinsed with chlorobenzene. The solvent washings were analyzed for PCBM and DH6T using UV-Vis spectroscopy; none was detected. Then the material was activated at 125˚C for 6 hours. An SEM image taken of the as-synthesized crystals show they are approximately 100-200 μm in size (see Supporting Information Figure 2).

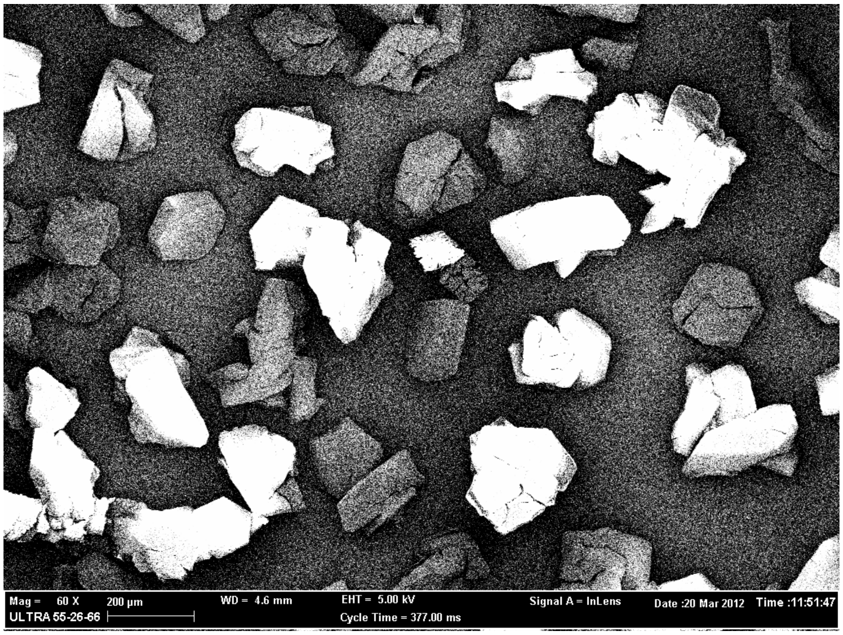

Figure 2. SEM image of MOF-177 crystals used for infiltration with guest molecules.

2.2.3. Characterization methods.

The loading of DH6T and PCBM in MOF-177 was quantified by digesting a known sample mass in a 1.0 M sodium hydroxide (NaOH) solution. DH6T and PCBM were extracted from this solution using a known volume of chlorobenzene, in which both molecules are highly soluble, which was then washed with water. The amounts of DH6T and PCBM were quantified using UV-Vis spectroscopy and calibration curves obtained from known concentrations of DH6T and PCBM.

Scanning electron microscopy (SEM) was performed using a Zeiss Gemini Ultra-55 Analytical Scanning Electron Microscope with 1 nm resolution; images were collected at 30 kV.

Steady-state and time-resolved photoluminescence measurements were collected using a Horiba Jobin-Yvon Fluorolog 3-21 fluorimeter, employing a 450 W Xe arc lamp and 341nm nano-LED, respectively. Photoluminescence experiments were conducted on crystalline powder samples of MOF contained in a powder stage holder. Absolute photoluminescence quantum yields of the crystalline MOF-177 and H_3BTB linker were measured in the integrating sphere system of a Hammamatsu Model C11347-11 Absolute Pholuminescence Quantum Yield Spectrometer. Diffuse reflectance UV-Vis-NIR spectra were recorded on a Cary 5000 spectrophotometer equipped with a reflectance sphere. The Kubelka-Munk conversion, $F(R)$ vs wavenumber, of the raw diffuse reflectance spectrum (R vs wavenumber) was obtained by applying the formula:

$$F(R) = (1 - R)^2/2R \qquad \text{(Eq.1)}$$

This transform creates a linear relationship for the spectral intensity relative to sample concentration and assumes an infinitely dilute, infinitely thick sample in the non-absorbing (Spectralon) matrix, and that the sample had a constant scattering coefficient. From the diffuse reflectance spectrum, the band gap energy of MOF-177 was experimentally determined using following equation:

$$E_g = hc/l = (1240\ \text{eV}\bullet\text{nm})/l \qquad \text{(Eq.2)}$$

where h is Planck's constant (4.13×10^{-15} eV•s), c is the speed of light (2.998×10^{8} m/s) and l is the absorption edge (λ in nm).

Powder X-ray diffraction experiments were carried out using a PANalytical Empyrean™ diffractometer equipped with a PIXcel-3D detector operating in scanning line detector mode with Cu K-alpha radiation (λ_α = 1.54187 Å). The samples were activated and then ground to a fine powder in ambient air, applied to a low background sample holder and mounted to a flat sample stage. Raw data were then evaluated using the X'Pert HighScore Plus™ software V 3.0.0 (PANalytical, The Netherlands).

2.3. Results: Electronic structure calculations

2.3.1. *MOF-177.*

Using a combination of first-principles electronic structure calculations and UV-visible spectroscopy, we confirmed that the band gap and band alignment of MOF-177 are such that neither energy nor charge transfer are feasible from infiltrated molecules to the framework. Based on SCC-DFTB calculations, the band gap of MOF-177 is predicted to be 3.35 eV, with a valence band (VB) maximum at -6.15 eV and conduction band (CB) minimum at -2.80 eV. The predicted band gap is in excellent agreement with the value of 3.3 eV which we determined by diffuse reflectance measurements, based on a band cutoff at 380 nm.

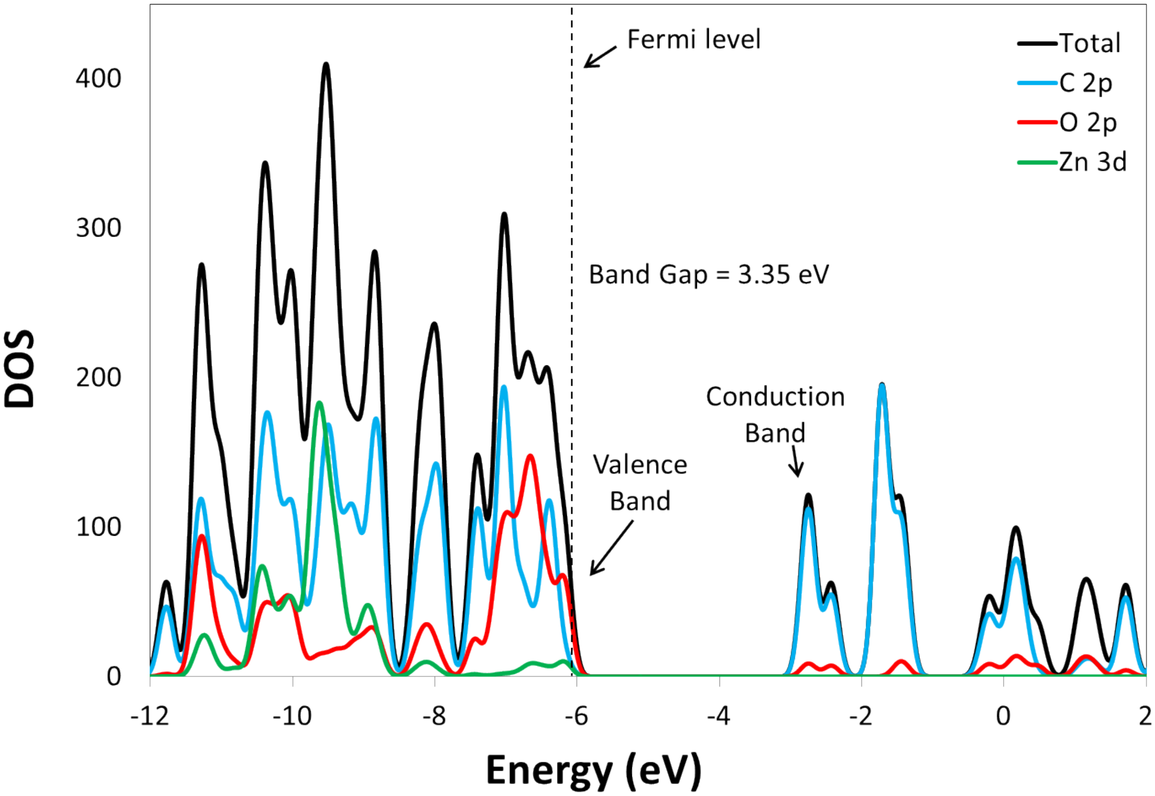

Figure 3. Partial Density of States (PDOS) - Density Functional Tight-Binding (DFTB) calculations of MOF-177.

The partial density of states (PDOS) (Figure 3) indicates that the composition of the MOF-177 band edges are dominated by the H_3BTB linker, with minimal contribution from the zinc clusters (Zn-O). Therefore, we expect that the electronic structure of the linker governs the MOF absorption and emission properties. Steady-state luminescence spectroscopy and timing analysis of MOF-177 and the H_3BTB linker in dilute solution confirm this conclusion. As seen in Figure 4, the excitation and emission spectra of MOF-177 are very similar to those of H_3BTB. The MOF-177 excitation and emission maxima occur at 345 and 380 nm, respectively, whereas these maxima occur at 345 nm and 390 nm for H_3BTB in dilute solution. The slight (10 nm) blue shift in the MOF-177 emission spectrum is similar to what is observed in other Zn-carboxylate MOFs.[41] The emission decay curves of MOF-177 and H_3BTB in dilute solution can both be fitted to a bi-exponential decay curve (Table 1), yielding similar average lifetimes (τ_{avg}) of 20.9 ns and 20.7 ns, respectively. This is consistent with our previous spectroscopic investigations of zinc-carboxylate MOFs, which indicate there is little charge transfer between the organic linker and the closed d shell of the metal ion.[41],[42]

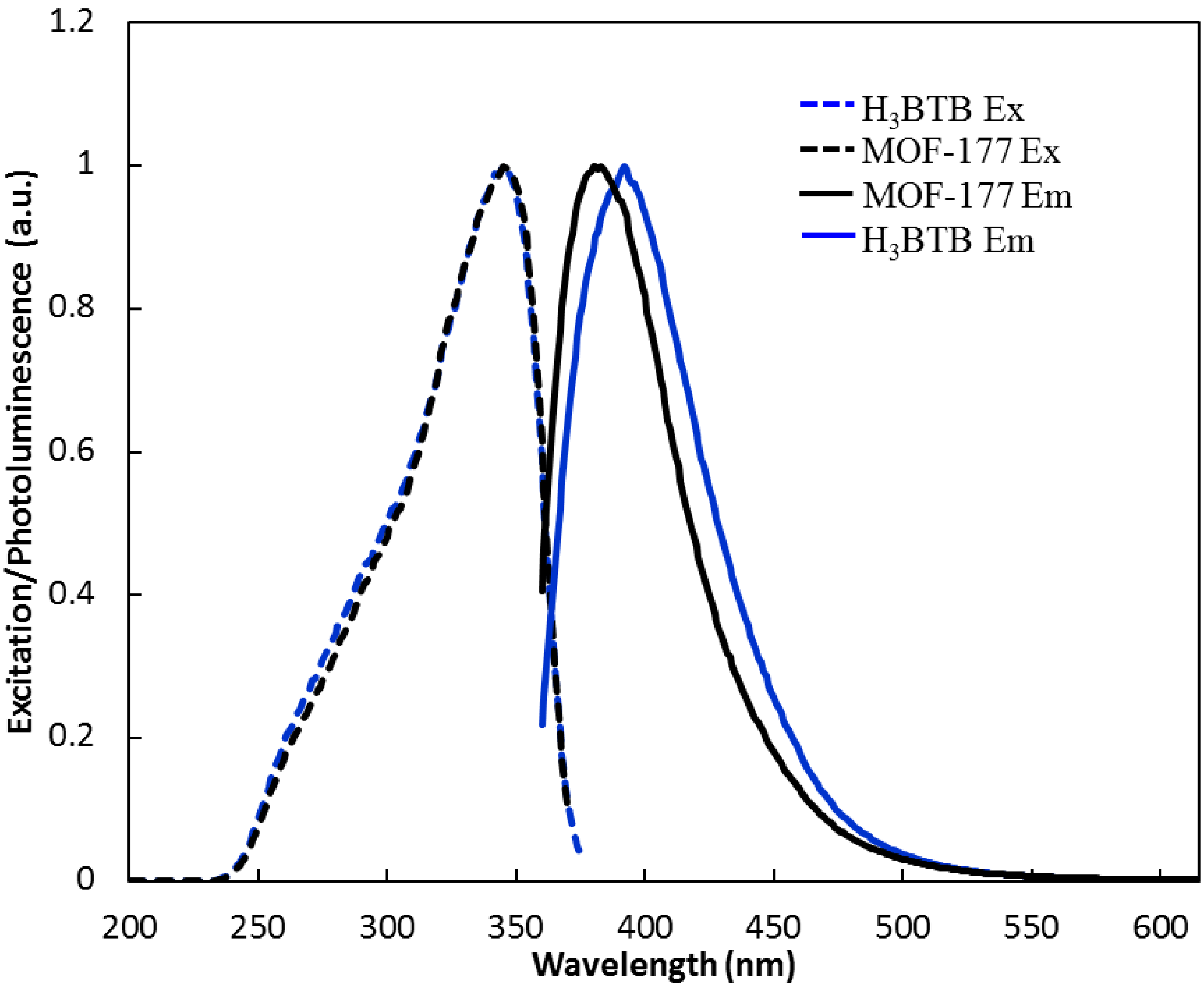

Figure 4. Solid state excitation and emission of MOF-177 (black) and dilute solution of H3BTB (blue) in DMF (1.0 x 10-6M). MOF-177: λ(ex)max= 345 nm; λ(em)max= 380 nm. H3BTB: λ(ex)max= 345 nm; λ(em)max= 390 nm.

Table 1. Solid state lifetimes of MOF-177, infiltrated MOF-177, H_3BTB, and DH6T.

	τ_0 (ns)	τ_1 (ns)	τ_2 (ns)	τ_{avg}
MOF-177	10 ± 0.28 (22%)	24 ± 0.09(78%)	-	20.9
DH6T@MOF-177	8 ± 0.20 (25%)	15 ± 0.11 (75%)	-	13.3
PCBM@MOF-177	1 ± 0.04 (22%)	9 ± 0.39 (78%)	-	7.2
DH6T+PCBM@MOF-177	0.4 ± 0.001(92%)	4 ± 0.02 (6%)	15 ± 0.72 (2%)	2.5
H_3BTB (solid)	8 ± 0.39 (10%)	17± 0.04 (90%)		16.1
H_3BTB (in DMF)	5 ± 0.32 (2%)	21 ± 0.05 (98%)		20.7
DH6T	0.5 ± 0.01 (87%)	2 ± 0.002 (13%)		0.7

*Average lifetimes were calculated using the equation $\tau_{avg} = \Sigma A_i\tau_i / \Sigma A_i$.

2.3.2. (Guest molecule)@MOF-177.

SCC-DFTB calculations show that MOF-177 can accommodate both DH6T and PCBM and that infiltration is energetically very favorable, both of which agree with experimental results described in the next section. Boltzmann averages of the total energies (SCC-DFTB, see above for computational details) created upon rotation are plotted versus the translational increments in Figure 5. The nature of the potential energy curves implies that the DH6T molecule, in spite of its rather large size (36.7 Å by 6.8 Å), and PCBM (11.7 Å by 12.1Å) are capable of diffusing through the MOF pores. As the molecules enter the pore, the total energy of the system decreases, indicating that a more stable system resulted. Moreover, no indications of an energy barrier are observed upon either PCBM or DH6T entering, suggesting that infiltration is feasible. Guest molecules infiltrating MOF-177 will likely enter and travel through Channel A because the cavity of B is blocked by the H_3BTB linker (no direct route through the MOF); however, diffusion into Cavity B is feasible, but expected to be less energetically favorable than traveling through channel A. The diffusion of DH6T into Cavity B is not plausible due to its long chain length and rigid backbone which severely hinders its ability to make the required 90º turn. This explains the decreased loading of DH6T observed compared to PCBM.

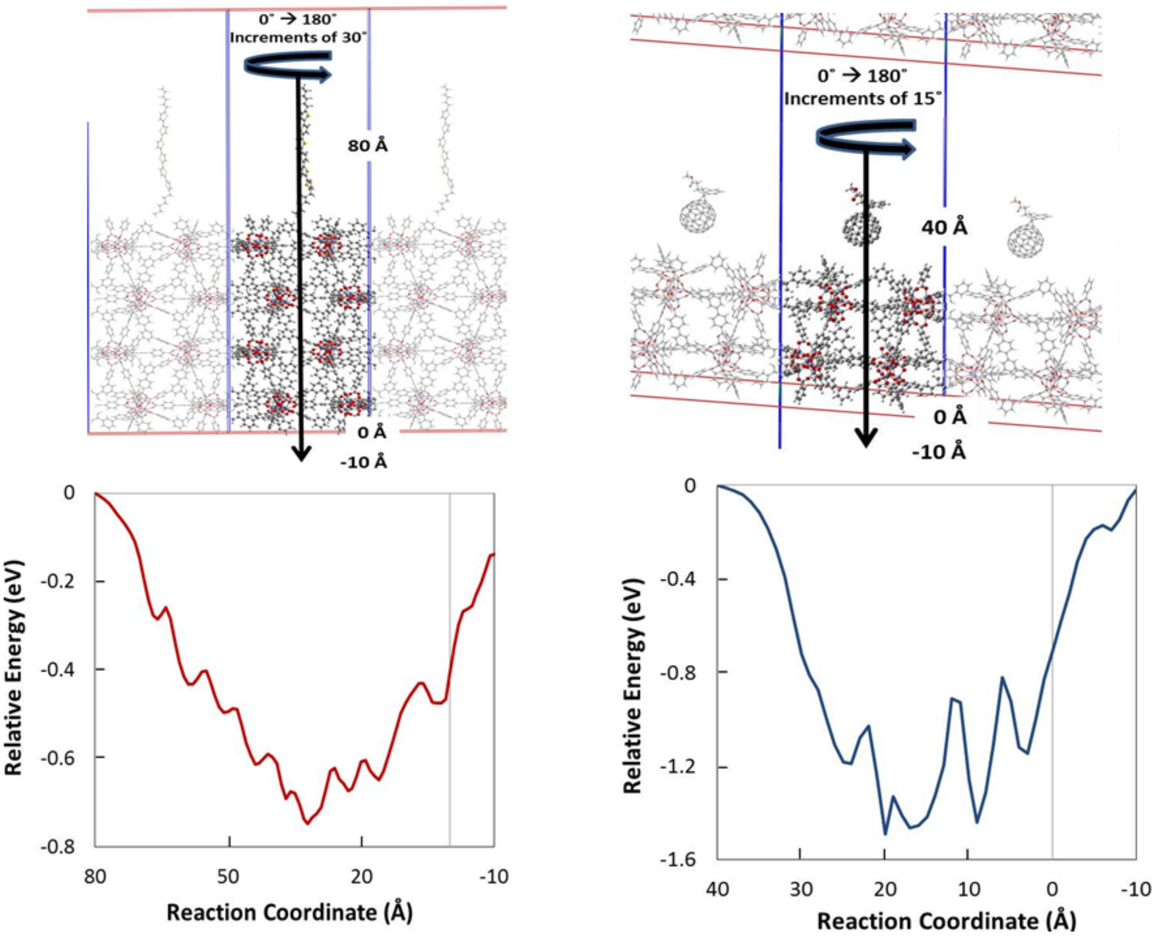

Figure 5. (a) Schematics showing the infiltration of MOF-177 with DH6T (left) and PCBM (right). (b) Potential energy curves of the infiltration process with DH6T (left) and PCBM (right) determined at the SCC-DFTB level of theory. The reaction coordinate corresponds to the distance between the bottom of the unit cell and the center-of-mass of DH6T or PCBM.

SCC-DFTB calculations indicate that DH6T and PCBM are strongly bound within the MOF-177 pore; the predicted binding energies (total energy of the system minus the optimized energy of the slab and the isolated infiltrating species) are 55 kcal/mol and 57 kcal/mol, respectively. (Note: the predicted binding energies neglect solvent effects, therefore, the actual values may differ.) The preferred orientation of the two molecules within MOF-177 was predicted by carrying out full geometry optimizations for the structures corresponding to the energy minimum of each curve in Figure 5b. The calculations indicate that DH6T absorbs onto the side wall of the MOF with pi-pi stacking observed between many different H_3BTB linkers. We also find that PCBM orients within the MOF between two H_3BTB linkers, such that the π orbitals of the linkers overlap with the fullerene ring of PCBM. This suggests the possibility of charge transfer between the MOF linker and PCBM, prompting us to perform time-dependent DFT (TDDFT) calculations (see Discussion).

2.4. Experimental Results

2.4.1. DH6T and PCBM Infiltration.

Immersing MOF-177 crystals (Figure 1) in saturated chlorobenzene solutions containing DH6T, PCBM, and mixtures of the two molecules produces rapid, visually discernable color changes after a few hours of exposure. This contrasts with the report by Chae et al., in which infiltration with C_{60} was reported to occur after one week,[32] and is most likely due to the higher solubility of PCBM relative to C_{60}. After one week, the translucent, colorless MOF crystals immersed in the DH6T solution become pale yellow, while those exposed to PCBM become dark violet. PXRD of MOF-177 and infiltrated MOF-177 shows no changes to the framework or the presence of new phases, indicating that the framework maintains its integrity in the presence of DH6T and PCBM. Small changes in the relative peak intensities may suggest some modification of the preferred orientation upon infiltration, but it is difficult to draw firm conclusions on this basis.

DH6T and PCBM loadings were quantified using both UV-Vis spectroscopy and elemental analysis. We obtained a DH6T content of ~0.1 wt%, corresponding to ~1 DH6T molecule for every 11 unit cells, and a PCBM loading of 22 wt%, corresponding to 2 – 3 PCBM molecules per unit cell. When exposed to an equimolar mixture of DH6T and PCBM, the loadings were ~0.04 wt% for DH6T and ~11 wt% for PCBM, corresponding to one DH6T molecule per 28 unit cells and 1 PCBM molecule per unit cell. Although these PCBM loadings are high (comparable to those used in PCBM-polymer blends used for bulk heterojunction devices), there is no evidence for a luminescence peak at ~500 nm exhibited by PCBM films,[43] suggesting that the post-infiltration washing procedure effectively removes any residual PCBM on the surface of the crystals. The low DH6T loading can be attributed to the linear backbone and rigidity of the

DH6T molecule. Elemental analysis reported a 0.1 sulfur wt% on DH6T@MOF-177, 58.5 carbon wt% on PCBM@MOF-177, and <0.005 sulfur wt% in DH6T+PCBM@MOF-177. The loadings using UV-Vis spectroscopy and elemental analysis are consistent with one another.

We find that shorter thiophene oligomers also penetrate the MOF, but the loadings clearly illustrate the steric constraints imposed by the MOF-177 pore dimensions relative to the kinetic diameter and further side groups on the parent chain of an infiltrating molecule. The elemental analysis results of terthiophene (3T) and quarterthiophene (DH-4T) infiltrated MOF-177 crystals report a sulfur content of < 0.005 wt% for 3T@MOF-177 and 1.25 ± 0.02 wt% for DH-4T@MOF-177. These loading contents correspond to less than one 3T molecule in a unit cell and three DH-4T molecules per unit cell. We attribute the lower loading of 3T in MOF-177 compared to both DH-4T and DH6T to steric hindrance by the alkyl side chains on DH-4T and DH6T with the MOF framework.

2.4.2. Luminescence spectroscopy.

The emission spectrum of DH6T@MOF-177 excited within the MOF-177 excitation spectrum (345 nm) exhibits quenching of the linker-associated emission and the simultaneous appearance of a weak, broad emission band at lower energy (450-700 nm; Figure 6a). Small shifts to shorter wavelength (~16 nm) in both the excitation and emission maxima relative to uninfiltrated MOF-177 suggest that the linker environment is modified by the presence of DH6T molecules within the framework. Both are blue shifted relative to H_3BTB in DMF, for which λ_{em} is 390 nm (Figure 4). Hypsochromic shifts are consistent with a less polar environment within the MOF pores compared with DMF.[44]

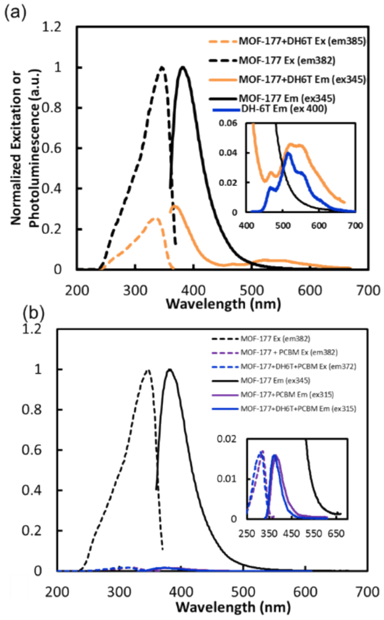

Figure 6. Photoluminescence spectra of (a) solid state MOF-177 and DH6T@MOF-177; DH6T emission (blue curve) and (b) solid state MOF-177, PCBM@MOF-177, and DH6T+PCBM@MOF-177..

These results demonstrate that fluorescence resonance energy transfer (FRET) occurs from the framework linker groups to DH6T. Spectral overlap between the MOF-177 emission and DH6T and PCBM absorbance is a requirement for efficient FRET to occur between emitting and absorbing molecules; this clearly exists for all three guest@MOF-177 samples (Figure 6). The weak band at lower energy in the emission spectrum of DH6T@MOF-177 corresponds to the emission of DH6T, excited by pumping the absorption of the BTB linkers. In the solid state, the emission spectrum of DH6T (overlaid in Figure 6a) shows a λ_{em} maximum at 512 nm and vibronic structure attributed to coupling with the C=C stretching mode[45] at 460 and 548 nm. The same structure is evident in the DH6T@MOF-177 spectrum. Similar quenching is observed when the linker and DH6T are present in solution. The magnitude of the H_3BTB quenching in solution increases as the concentration of DH6T increases, as does the DH6T emission intensity; the isosbestic point shows that the two are correlated. These results not only confirm that energy transfer occurs between the H_3BTB linker and DH6T, but also that DH6T must be present as guest molecules within the MOF pores. FRET is not typically effective at distances > 10 nm (discussed below), which is far shorter than the typical crystallite size in these samples (~ 100 - 200μm).

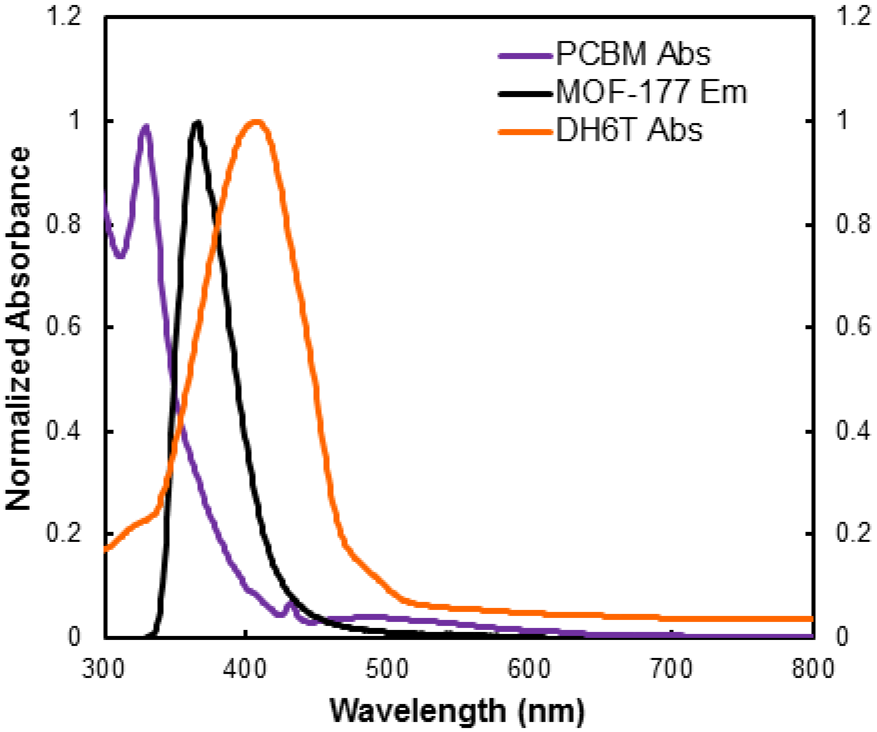

Figure 7. Spectral overlap of MOF-177 emission (neat powder) with DH6T and PCBM absorption (dilute solutions in chlorobenzene).

Infiltration of MOF-177 with PCBM also quenches the MOF emission (Figure 6b). Since no emission from PCBM is observed, however, it is not immediately clear whether this is due to non-emissive fluorescence quenching or energy transfer. However, the very strong overlap between the MOF-177 emission and the absorption by PCBM makes it very likely that FRET is occurring. A shift of the excitation spectrum to shorter wavelength is observed here as well, which may indicate that PCBM modifies electronic interactions with the linkers that stabilize the emitting excited state. The presence of both DH6T and PCBM in the MOF leads to an emission spectrum similar to PCBM@MOF-177, as seen in Figure 6b.

2.4.3. Lifetime measurements and FRET properties.

Decreased luminescence decay time constants show that quenching in all three guest@MOF systems is caused by interactions between the linker excited state and the quenching guest molecule and not by the formation of a ground-state complex between the linker and guest. Diffuse reflectance spectra of the infiltrated materials do not indicate the formation of a ground state guest-linker complex, confirming that Dexter energy transfer is not active here. Luminescence decay curves obtained from lifetime measurements of MOF-177 and guest@MOF-177 were fitted to bi-exponential expressions for DH6T@MOF-177 and PCBM@MOF-177 and a tri-exponential expression for DH6T+PCBM@MOF-177 (Table 1). Both the average lifetime (τ_{avg}) of the MOF-177 PL and the individual component lifetimes decrease upon infiltration with DH6T, PCBM, and (DH6T+PCBM).

Distances for effective energy transfer and average donor-acceptor distances computed from the quenching data show that FRET is required to account for the quenching extents observed here. The Förster radii R_0 are 39 Å and 27 Å for DH6T and PCBM, respectively, which were determined from the measured MOF-177 quantum efficiency Φ_d (24.3%) and spectral overlap J. Using these values and τ_{avg} for MOF-177 and its infiltrated versions, we computed energy transfer rate constants (k_T), quantum yields (φ_{eng}), and donor-acceptor distances r (Table 2).[44] For DH6T@MOF-177, φ_{eng} is 37%; PCBM is an even more effective quencher of MOF-177 luminescence, with a φ_{eng} of 65%. Not surprisingly, infiltrating with both DH6T and PCBM results in the highest quenching, with φ_{eng} of 88%. The corresponding energy transfer rates k_T are 2.6×10^7 sec^{-1} for DH6T@MOF-177 and 8.2×10^7 sec^{-1} for PCBM@MOF-177. The distances r at which these quenching extents occur are ~43Å for DH6T and 24Å for PCBM and are nearly the same as the Förster radii.

Table 2 Energy transfer quantities computed from steady-state luminescence decay curves.

	τ_{avg} Guest@MOF / τ_{avg} MOF		
	DH6T@MOF-177[a]	PCBM@MOF-177[a]	(DH6T+PCBM)@MOF-177[b]
J value (cm^6)	2.5 x 10^{-14}	2.7 x 10^{-15}	--
R (Å)	39	27	--
φ_{eng} (%)	36	66	88
***k* (1/s)**	2.6 x 10^{7}	8.2 x 10^{7}	
r (Å)	43	24	

[a] Computed using PhotochemCAD. [b] Computed from Equation S8 in the Supporting Information; PhotochemCAD cannot compute quantities for three-component luminescent systems.

2.5. Discussion

2.5.1. Energy transfer pathways.

The luminescence results described above establish that FRET is responsible for the observed quenching rates in DH6T-infiltrated MOF-177, which is likely also the case for PCBM@MOF-177. In contrast with collisional quenching processes that occur in solution, the MOF strongly immobilizes guest molecules within the pores, which can then interact with only a limited number of linkers in their immediate vicinity. Relaxed geometries for DH6T@MOF-177 and PCBM@MOF-177 predicted by DFTB indicate that the closest interatomic distances are 3.6 Å and 3.5 Å, respectively, which are close enough for interaction between their electron clouds that could produce nonradiative energy transfer (i.e. charge transfer). Such interactions fall off exponentially with distance, however.[44] Thus, energy transfer must occur over longer distances (> 10 Å) in guest@MOF-177 materials to achieve the observed quenching levels. It is clear that this occurs for DH6T@MOF-177, for which the loading is very low, ~ 1 DH6T molecule per 11 unit cells. The greatest distance to any linker in a cube of 11 unit cells is 64 Å, which is significantly larger than the 39 Å Förster radius. This is consistent with the measured quenching quantum yield of 37% (Table 2). At the higher loading in PCBM@MOF-177, ~ 2.5 PCBM per unit cell, the maximum linker-PCBM distance is only ~15 Å, which is well within the 27 Å Förster radius. Notably, the PCBM@MOF-177 loading here (22 wt%) is comparable to typical PCBM loadings in polymer-fullerene blends (~20 wt%), where energy transfer is dominated by fluorescence resonance energy transfer (FRET) at loadings of 20 wt%.[6] However, this is achieved without phase segregation prevalent in bulk heterojunctions that increases the exciton diffusion distance.[6]

These results also suggest the possibility that some of the quenching observed in the DH6T+PCBM@MOF-177 system is due to a "FRET cascade," in which MOF-177 is the donor, PCBM is the acceptor (Figure 8). This process (*i.e.* MOF-177 → DH6T → PCBM) consists of multiple individual FRET processes from MOF-177 → DH6T, DH6T → PCBM, and MOF-177 → PCBM. Thus, DH6T would play a dual role, serving as an acceptor for MOF-177 and a donor for PCBM and facilitating the energy transfer. The broad emission at longer wavelengths corresponding to DH6T, which was previously observed in DH6T@MOF-177, is absent in DH6T+PCBM@MOF-177, consistent with PCBM quenching the emission of DH6T and energy transfer from DH6T to PBCM. This mechanism is feasible in DH6T+PCBM@MOF-177 because of favorable spectral overlap between the donor (linker) emission and the absorption spectrum of the acceptors. Band gaps obtained from periodic SCC-DFTB calculations of MOF-177 and the isolated guest molecules show that there is sufficient excitation energy within the MOF linker and appropriate band alignment to enable FRET with both DH6T and PCBM (Figure 8). As a consequence, MOF-177 is not merely a passive host for guest molecules, but plays an active role in this infiltrated system by harvesting additional photons from the solar spectrum that are efficiently transferred to DH6T and PCBM. A detailed assessment of the importance of a FRET cascade is outside the scope of this paper, however.

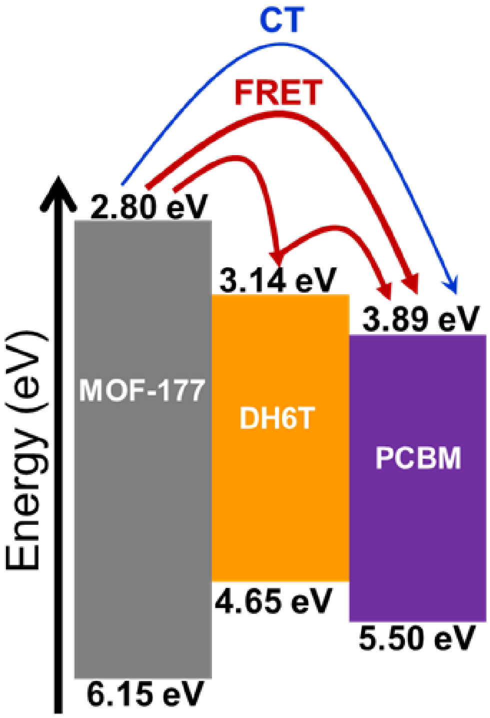

Figure 8. MOF-177, DH6T, & PCBM band alignment predicted by SCC-DFTB.

A remaining question concerns the origin of the multi-exponential luminescence decays produced by both MOF-177 and the guest@MOF-177 samples. The τ_1 of MOF-177 (24 ns) can be assigned to emission from individual linkers, since it closely resembles that of H_3BTB in dilute solution (21 ns) and the excitation and emission spectra are nearly identical (Figure 4). This indicates that, within the MOF-177 structure, a given linker is largely isolated from others in the framework. However, the presence of a second, fast component with τ_0 of 10 ns indicates that additional interactions exist. The origin of this component is unclear, but possibilities include interlinker interactions, a distribution of occupied and unoccupied sites in these infiltrated MOFs, and, as was previously suggested for a porphyrin MOF system, exciton-exciton annihilation.[21]

2.5.2. Charge transfer.

The possibility that charge transfer occurs in these guest@MOF systems cannot be completely ruled out, since this mechanism is not fully probed by our techniques. The spectral overlap between MOF-177 and DH6T, the observed luminescence quenching, and the favorable DH6T-PCBM band alignment could promote charge separation between these two molecules. These alone are not sufficient to demonstrate that it occurs here, however.

We therefore assessed the potential that charge-transfer between the MOF linker (H_3BTB), DH6T, and PCBM could occur by using TDDFT (wB97XD/6-31G(d,p)) calculations to predict the optical absorption spectra and electron density difference maps (EDDMs[46] also known as the charge difference density (CDD) maps) between various excitations. This approach is similar to that used previously to identify a CT band in another zinc based MOF.[47] The optical absorption spectra of the two donor-acceptor clusters H_3BTB@DH6T and H_3BTB@PCBM, considering the first 100 excited states, are shown in Figure 9. In addition, EDDMs for several of the excited state transitions with appreciable oscillator strengths are shown as inserts. EDDMs visually represent electron transfer effects upon excitation, which is determined by subtracting the ground state electron density from the excited state. These calculations show that the introduction of PCBM to create H_3BTB@PCBM leads to the formation of linker-to-guest charge transfer states. This is evident in several of the dominant optically active excited states (S_{34} and S_{51}) in the 300-250 nm spectral region (Figure 9 top). For these transitions, the EDDMs show increased electron density on the PCBM molecule upon excitation, as represented by the light blue lobes. The purple regions represent decreased electron density and are absent on PCBM, giving evidence that charge transfer can occur.

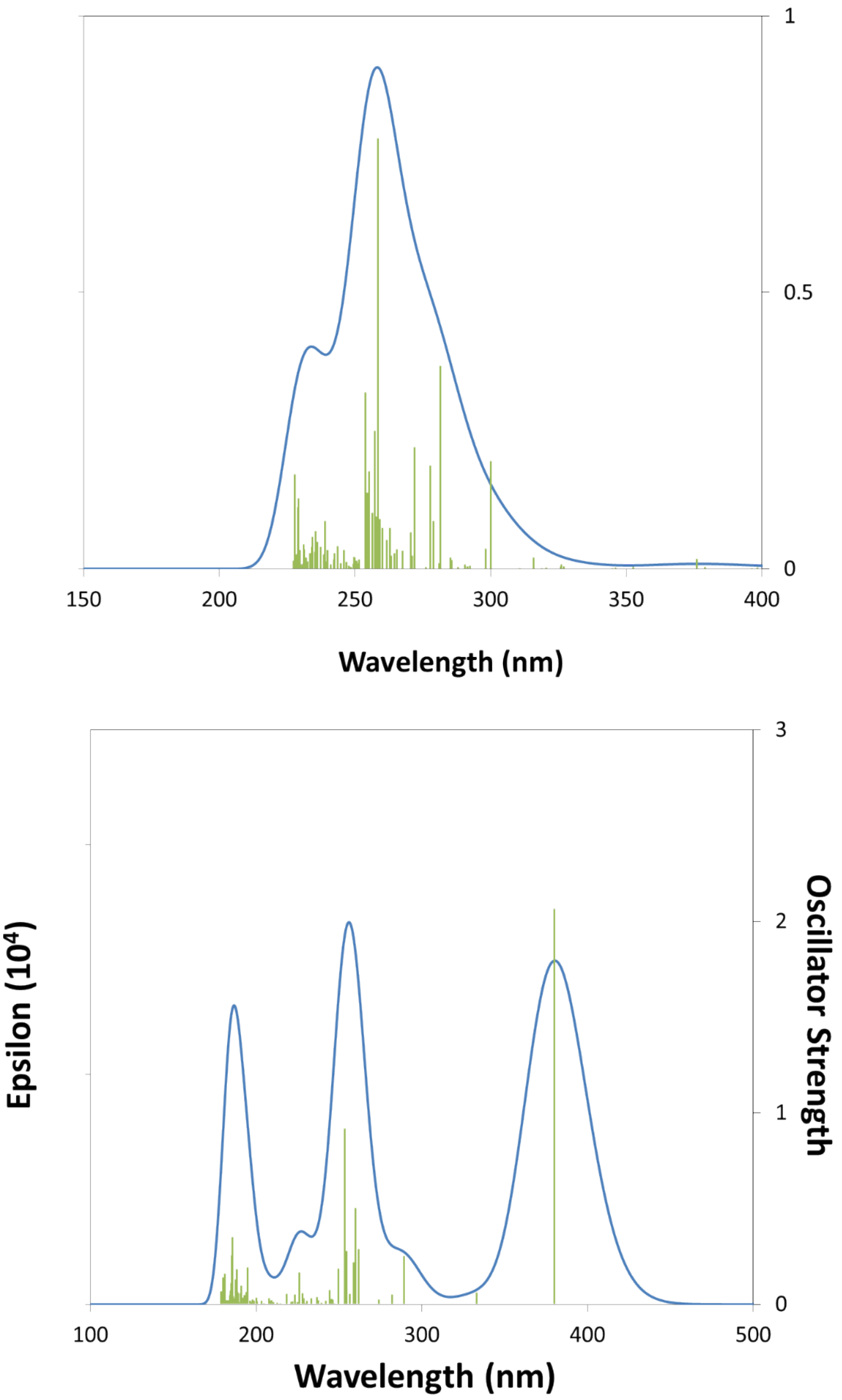

Figure 9. Optical absorption spectra of H_3BTB/PCBM (top) and H_3BTB/DH6T (bottom) computed using TDDFT at the wB97xD/6-31G(d,p) level of theory. The molecular images show the change in electron density upon excitation. The purple and light blue regions represent a decrease (holes) and increase (electrons) in the electron density respectively. For clarity, S_3 and S_{30} transitions have been omitted. All EDDMs plots were constructed using the same isosurface contour value.

In contrast, charge transfer states are not clearly evident in the H_3BTB@DH6T cluster, based on the EDDM analysis of several of the optically active transitions. Here, the change in electron density is either localized on the individual molecules or evenly distributed across both molecules. However, the LUMO of H_3BTB lies above that of DH6T, which implies that upon excitation of H_3BTB, charge transfer to DH6T should be feasible. These results and those for PCBM@MOF-177 indicate direct parallels between guest@MOF systems and conventional bulk heterojunctions, in that proper composition of the linker group and guest molecular orbitals, as well as their energy alignment, are needed to enable charge transfer.

2.6. Conclusions

The results presented here indicate that MOFs can function as hosts for organic donor and acceptor molecules typical of those used in excitonic devices, such as bulk heterojunctions and solid-state lighting. The spectroscopy of DH6T and PCBM confined within MOF-177 indicates that efficient quenching of the MOF-177 luminescence by FRET occurs, which recent work indicates is an important, possibly dominant, mechanism of energy transfer in polymer-fullerene blends.[6] Although the nature of their constituents and bonding makes most MOFs nominally insulators, even these can play an active role by serving as a photon antenna to harvest light that is not efficiently absorbed by the donor and transfer it to guest acceptor molecules. Our results suggest that, by taking full advantage of MOF porosity, as well as their inherent structural order, one can create MOF-donor-acceptor hybrids in which all constituents play an active role. This not only allows the chemical environment of the donor and acceptor molecules to be clearly defined, it also enables the use of accurate first-principles theoretical methods that would be difficult to implement in disordered polymeric systems. By way of illustration, TDDFT calculations presented here indicate that some PCBM@MOF-177 excited states involve linker-to-guest charge transfer, suggesting that photoconductivity might be achievable in an appropriately designed guest@MOF system.

3. NOVEL METAL-ORGANIC FRAMEWORK LINKERS FOR LIGHT HARVESTING APPLICATIONS

3.1. Introduction

Metal-organic frameworks (MOFs) are receiving considerable attention due to their large surface area to volume ratios and tunable pore sizes. To date, research has primarily focused on applications relating to gas storage[48-51], gas purification and separation[52-56], chemical sensing,[57-59] and catalysis.[60-62] Recently, the light harvesting and intrinsic charge transport properties of MOFs have become of interest for electronic and photonic applications.[63-69] These efforts stem from both the success and shortcomings of current approaches based on organic materials, such as organic photovoltaics based on a bulk-heterojunction (BHJ) architecture. Although organic and organic-inorganic hybrid materials demonstrate exceptional promise for next-generation optoelectronic applications, the donor-acceptor interfaces in these systems are typically poorly ordered, leading to inefficient charge separation upon photoexcitation.[70] The potential utility of MOFs arises from a combination of their nanoporosity, which can accommodate guest molecules, and the ability to control donor-acceptor interactions and phase separation at the nanoscale, enabled by the long-range order inherent in these porous crystalline frameworks. For example, we recently showed that fullerenes and thiophenes, organic molecules typically used in OPV devices, can be stabilized within a MOF without phase segregation. The MOF host used in that investigation was MOF-177, a nominally passive (i.e. not charge conducting) structure that nevertheless performed the additional functions of light harvesting and energy transfer to the guest molecules by Förster resonance energy transfer (FRET).[69]

In theory, however, MOFs can also be designed to play an *active* role, serving as one half of a donor-acceptor interface (the other half residing as guest molecules in the pores), thereby facilitating charge separation and transport in the device active layer. This requires the MOF to have specific electronic properties, including high charge-carrier mobility, broad spectral coverage, large absorption coefficients, and the appropriate orbital alignment with the opposing material residing in the pores, while retaining relevant geometrical parameters.[71-73] The MOF cavities or channels must also be sufficiently large to allow diffusion and accommodation of the infiltrated species (e.g. PCBM) in ample quantities. To date, nearly all MOFs are dielectric materials, particularly those with appreciable porosity; therefore, expansion of MOF applications to include optoelectronic devices requires the design and synthesis of new porous MOFs with semiconducting attributes.

Creating a functional MOF-based electronic device is a major challenge given the synthetic complications and challenges associated with the integration of these materials in a structurally controlled manner. Several strategies have been proposed for designing electrically conducting MOFs (e.g., using transition metals, redox-active linkers, and hetero-bimetallic structures), but limited success has been achieved.[74, 75] Nevertheless, the synthetic versatility of MOFs is encouraging and allows for facile tuning of their structural and electronic properties. There are three general approaches for altering the structural and electronic properties of MOFs: i) changing the metal ion(s), ii) modification of the organic linker(s) and/or iii) infiltration of select molecules into the framework, resulting in the formation of new metal-to-ligand (ligand-to-metal) charge-transfer (MLCT (LMCT)) states. To our knowledge, the first reported porous, intrinsically conducting MOF is Cu[Ni(pdt)$_2$] (pdt^{2-} = pyrazine-2,3-dithiolate),[76] which is a *p*-type semiconductor with a conductivity of 1 x 10^{-4} S/cm enabled by a redox mechanism. More recently, Sun and co-workers[66] disclosed a manganese based MOF utilizing a thiophenol linker (2,5-disulfhydrylbenzene-1,4-dicarboxylic acid), referred to as Mn$_2$(DSBDC), a variant of IRMOF-74[77-79] (Figure 10), that exhibits high intrinsic charge mobility. The same group[65] also reported a tetrathiafulvalene (TTF) zinc-based MOF that exhibits a charge mobility of 0.2 cm^2/V·s. The proposed charge transfer (CT) mechanisms for these two systems are reportedly different. It is proposed that Mn$_2$(DSBDC) exhibits band transport through the infinite metal-oxide secondary building units (SBUs).[80] In contrast, charge hopping through the organic linkers is suggested as the conduction mechanism operative in the TTF MOF, since these groups are spaced ~3.8 Å apart.

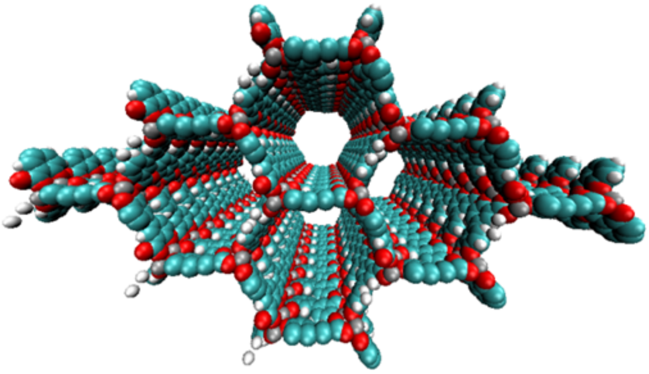

Figure 10. A supercell representation of the periodic PBE optimized IRMOF-74-II(Mg) structure.

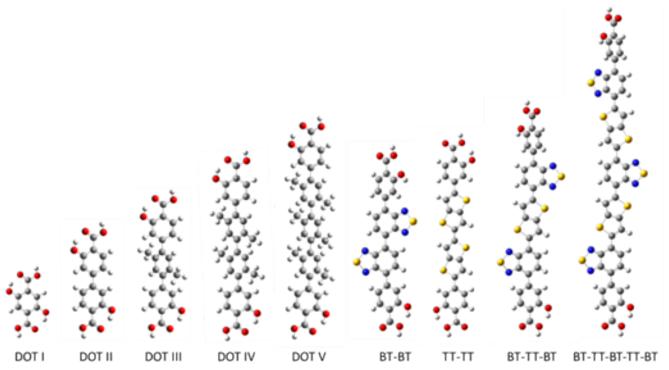

Figure 11. The LC-BLYP/6-311G(d,p) optimized DOT I-VI linkers and proposed BT/TT linker series.

Here, we propose a new modular series of conjugated organic linkers (Figure 11) that are capable of forming the same infinite metal-oxide SBU as IRMOF-74 and acting as electron donors to well-known electron acceptors used in OPV, such as PCBM. Due to the nature of the proposed linkers and SBU, this new MOFs series allows for the formation of a continuous π-π stacking network potentially providing a direct route to facilitate charge transport. Synthesizing MOFs with these proposed linkers is feasible based on a previous study showing that the pore aperture of IRMOF-74 can be systematically increased. In that case, the organic linker (dioxidoterephthalate (DOT)) was lengthened to include up to 11 phenylene rings (DOT I-XI), creating an isoreticular series termed IRMOF-74-I to XI.[81] IRMOF-74 can also be readily synthesized with several different coordinating metals (IRMOF-74(M); M = Mg, Mn, Fe, Co, Ni, and Zn),[77, 82] providing an unusually high degree of synthetic versatility (IRMOF-74-II(Mg) is shown in Figure 10). We consider the Mg variant (IRMOF-74(Mg)) for its simple electronic structure (no *d* electrons); Mg^{2+} precludes MLCT or LMCT resulting in the localization of the frontier orbitals (HOMO and LUMO) entirely on the linkers and not on the metal. As a result, there is no competing CT state, enabling charge transfer and separation to occur only between the linker and the corresponding infiltrated electron acceptor. The electronic properties of the MOF, therefore, will be largely governed by the linker moiety. In addition, the high oxidation and low reduction potentials of Mg should prevent the metal ions in the framework from acting as charge carrier traps within an electrical device.

Here, we use a novel non-empirically tuned long-range corrected density functional theory (DFT) method[83-86] to demonstrate that these new linkers result in MOFs with the appropriate optoelectronic criteria and band-alignments with well-known electron acceptor components (i.e. PCBM) for light harvesting applications. To our knowledge, this is the first time that a non-empirically tuned density functional has been used to guide experimental MOF design. Specifically, we demonstrate that these MOF linkers are capable of absorbing light in the visible region and have large oscillator strengths compared to the parent DOT linker series. We validated our computational approach by synthesizing the BT-TT-BT linker and comparing its optical properties to several of the DOT linkers used in the IRMOF-74 series. These results and the corresponding synthetic protocol serve to demonstrate that the proposed linkers are chemically accessible in a straightforward manner using conventional synthetic methodologies and that the predicted and measured optical properties are in good agreement. In addition, we carried out periodic calculations for several of the extended MOF systems, confirming that the coordinating metal (Mg) does not interfere with the band edge. Consequently, useful information can be obtained by modeling the isolated linker allowing for rapid screening of potential organic linkers with desirable electronic properties. Finally, we discuss the confinement of electron acceptor materials within the MOF framework, showing that this can dramatically reduce the exciton diffusion length, an important factor governing efficiency in organic photovoltaics (OPV) and other optoelectronic devices.[71]

3.2. Computational Details and Methodology

All density functional theory and time-dependent DFT (TDDFT) molecular orbital calculations were carried out using a non-empirically tuned long-range corrected (range-separated) density functional (LC-DFT) method. Recent theoretical work shows that range-separated functionals[87] are essential for modeling long-range charge-transfer and Rydberg states.[88-91]

In addition, non-empirically tuned LC-DFT methods yield dramatic improvements for predicting fundamental and optical gaps over pure (nonhybrid) and hybrid functionals, when compared to experimental and/or results from more computational rigorous quantum mechanical methods.[83-85] The fundamental gap is defined as the difference in energy between the first ionization potential (IP) and the first electron affinity (EA), whereas the optical gap is the difference in energy between the lowest dipole-allowed excited state and the ground state. In general, the optical gap is smaller than the fundamental gap due to the Coulombic attraction between the excited electron and hole within the molecule. The improvements stem from the way the local DFT and nonlocal Hartree-Fock exchange are admixed. Range-separated functionals, in contrast with conventional hybrid functionals (i.e. B3LYP) that include a fixed percentage of Hartree-Fock exchange, incorporate nonlocal electron exchange as a function of the inter-electronic distance. As a result, the correct asymptotic behavior at large interelectronic distances is achieved. In LC-DFT, the electron repulsion operator $1/r_{12}$ is separated into short-range (1st term) and long-range (2nd term) contributions:

$$\frac{1}{r_{12}} = \frac{1-\mathrm{erf}(\mu \cdot r_{12})}{r_{12}} + \frac{\mathrm{erf}(\mu \cdot r_{12})}{r_{12}}, \qquad (1)$$

where "erf" denotes the standard error function, r_{12} is the interelectronic distance between electrons 1 and 2, and μ is the range-separation parameter in units of Bohr^{-1}. It has been demonstrated that μ is system dependent, but can be non-empirically tuned for a given system by minimizing the following function:[86, 88]

$$J^2(\mu) = [\varepsilon_{HOMO}(N,\mu) + \mathrm{IP}(N,\mu)]^2. \qquad (2)$$

Here, $\varepsilon_{\mathrm{HOMO}}(\mathrm{N},\mu)$ is the energy of the HOMO, and IP is the ionization potential of the N electron system determined from the difference between the total energies of the N and N-1 electron systems. In other words, the optimal μ value ensures that the negative of the HOMO energy is equal to the ionization potential. This is a fundamental condition within the Kohn-Sham DFT formalism (i.e., Janak's theorem[92]), which justifies this self-consistent tuning of μ. Several slight variations of Eq. 2 have been proposed (i.e. including the N+1 system);[88] however, the approach presented here carries the lowest computational burden. More importantly, the different approaches tend to produce similar results.[93] For example, for the BT-TT-BT linker considered here (see below), the optimal μ value differs by only 0.2% when the N+1 state is included in the tuning procedure.

For the DOT-type linkers of the known IRMOF-74 series and new linkers proposed here, as well as for PCBM ($PC_{61}BM$), $PC_{71}BM$, P3HT (8 repeat units) and 2xBT-TT-BT@$PC_{71}BM$ (a molecular cluster containing 2 BT-TT-BT linkers and $PC_{71}BM$), the optimal range-separated parameter was determined by varying μ from 0.1 to 0.4 Bohr^{-1} in increments 0.1 Bohr^{-1}. For each value, full geometry optimizations were performed on the N-electron system followed by a single-point calculation of the +1 cation state (i.e., the N-1 electron system). Plots of J^2 as a function of μ for all molecules are shown in Figure 2; the minimum of each curve was determined by cubic spline interpolation (optimal μ values are reported in Table 1). Finally, full geometry optimizations were carried out with the corresponding optimal μ value, followed by determination of the first 20 singlet excitations (10 singlet excitations for 2xBT-TT-BT@$PC_{71}BM$) using TDDFT within the linear response formalism. Absorption spectra were determined by Gaussian convolution (full width at half-maximum of 3000 cm^{-1}) of the excitation energies and oscillator strengths to account for vibrational broadening of the spectrum at room temperature. All calculations were carried out within the Gaussian 09 package[94] using the LC-BLYP functional and the polarized 6-311G(d,p) basis set (6-31G(d,p) for 2xBT-TT-BT@PC$_{71}$BM) with default SCF convergence criteria (density matrix converged to at least 10^{-8} Hartree) and DFT integration grid (75 radial and 302 angular quadrature points). For 2xBT-TT-BT@PC$_{71}$BM, a smaller basis set was used, and fewer excitations were computed due to computational limitations associated with the size of the system (222 atoms). In addition, Grimme's empirical dispersion correction (S_6=1.20 and S_{R6}=1.10)[95] was used in order to take van der Waals interactions into consideration which are essential for modeling intermolecular interactions. During the geometry optimization of this cluster, the linkers (2xBT-TT-BT) were fixed in the orientation obtained from the optimized periodic structure (see below) to maintain the configuration of the linkers within the MOF.

Table 3. Optimal μ values, HOMO/LUMO energies, fundamental gaps (HOMO-LUMO), optical gaps ($S_0 \rightarrow S_1$ transition) and oscillator strengths of DOT I-V and the BT/TT series predicted at the LC-BLYP/6-311G(d,p) level of theory. All values are in eV; oscillator strengths are unitless.

Linker	Optimal μ	HOMO	LUMO	Fundamental Gap	Optical Gap	Oscillator Strength
DOT I	0.2715	-7.9	-0.6	7.3	3.3	0.115
DOT II	0.2507	-8.4	-0.5	7.9	4.1	0.304
DOT III	0.2089	-7.9	-0.4	7.5	4.1	0.407
DOT IV	0.2021	-7.8	-0.3	7.6	4.1	0.367
DOT V	0.1811	-7.7	-0.4	7.3	4.0	0.350
TT-TT	0.1829	-6.9	-1.0	5.8	3.1	2.161
BT-BT	0.1825	-7.4	-1.8	5.6	2.8	0.813
BT-TT-BT	0.1655	-6.7	-1.9	4.8	2.4	1.384
BT-TT-BT-TT-BT	0.1420	-6.2	-2.2	4.1	1.9	2.066
PCBM	0.1958	-7.4	-2.1	5.3	2.3	0.002
PC$_{71}$BM	0.1724	-7.1	-2.2	4.9	2.2	0.006
P3HT	0.1419	-5.9	-1.0	4.9	2.6	2.434

Density functional theory calculations employing periodic boundary conditions were carried out on three MOFs (IRMOF-74-II(Mg), IRMOF-74-TT-TT(Mg) and IRMOF-74-BT-TT-BT(Mg)) using the Vienna Ab initio simulation 5.2.12 package (VASP).[96-99] The Perdew-Burke-Ernzerhof (PBE) exchange-correlation functional[100] with an energy cutoff of 500 eV was used for all geometry optimizations. Interactions between ions and electrons were described using projector-augmented-wave (PAW) [101, 102] pseudo-potentials and a Γ-centered Monkhorst–Pack[103] *k*-point grid of 4×4×12 was used for sampling the Brillouin zone. The structures were relaxed until all forces were smaller than 0.01 eV/Å. The tetrahedron method with Blöchl-corrections was used to determine the partial occupancies for each wavefunction.[104] Single-point calculations were carried out on the optimized PBE structures using the HSE06 hybrid functional[105, 106] with a *k*-point grid of 2×2×6 using the Gaussian smearing method with a smearing width of 0.05 eV.

3.3. Results

The predicted HOMO and LUMO energies, fundamental gaps (HOMO - LUMO), optical gaps ($S_0 \rightarrow S_1$ transition), and oscillator strengths of DOT I-V (see Figure 11) illustrate that the electronic structure of the IRMOF-74 series is not well suited to PV applications. Values of these properties are tabulated in Table 1 and were determined using the non-empirically tuned LC-BLYP functional. The predicted fundamental gaps for DOT I-V are all ~ 7.5 eV. These values correspond to the molecule in the gas phase; thus, the large gaps are not unexpected. It has been shown that non-empirically tuned LC functionals predict fundamental gaps that are in very good agreement with experimental gas-phase measurements, as well as with more computationally intensive techniques such as many-body GW and CASPT2 (complete active-space second-order perturbation theory) methods.[83] The optical gaps, which are of primary importance for light harvesting, tend to be of similar energy in the gas and solid states and with the exception of DOT-I are ~ 4 eV. The large difference between the fundamental and optical gaps can be attributed to the magnitude of the exciton binding energy (fundamental gap – optical gap). For example, the experimental exciton binding energy of C_{60} in the gas phase is 3.0 eV and is reduced to 1.4-1.6 eV in the solid state.[107]

The TDDFT predicted optical gap of DOT I is 3.3 eV; this value is in near perfect agreement with the experimental absorption maximum occurring at 372 nm (3.3 eV; see Figure 12). The predicted optical gaps for DOT II-V are blue shifted from this value, occurring at approximately 4.0 eV, again in near perfect agreement with experiment (see SI for all experimental details and absorption spectra; DOT V was not experimentally considered here). Comparing the experimental and Gaussian convoluted TDDFT absorption spectra (Figure 12), the accuracy of the non-empirically tuned range-separated functional is clearly evident. The correlation between the spectra extends beyond the $S_0 \rightarrow S_1$ transition. For example, the $S_0 \rightarrow S_3$ transitions are predicted to be stronger than the $S_0 \rightarrow S_1$ transition for DOT II-IV, which is consistent with the experimental spectra. Although the DOT linkers allow for systematic control over the pore diameter of IRMOF-74, they absorb little, if any, of the visible spectrum, making them of little use for PV applications.

To create frameworks having the IRMOF-74 topology that are capable of harvesting visible light, chemical intuition and DFT suggest that modification of the organic linker is essential to achieving the desired optoelectronic characteristics. Although the literature of organic semiconductors provides many possibilities, the desire to incorporate these within the IRMOF-74 structure constrains the design process in two ways. In particular, IRMOF-74-*n* linkers must be linear and relatively rigid (Figure 11), with intramolecular rotation largely confined to rotations of phenyl groups around the primary axis. They must also include the *para*-CO_2^- and *ortho*-OH^- functionalities that can coordinate with the metal ions to preserve the original topology. Among the many light-absorbing donor materials reported, those featuring electron-deficient benzo[*c*][1,2,5]thiadiazole (BT) and alternating thiophenes are among the most promising.[108-111] Fused and rigidified thiophene based building blocks lead to extended conjugation, narrower band gaps and stronger intermolecular interactions. We therefore considered a new series of organic linkers composed of BT and/or alternating electron-rich thieno[3,2-*b*]thiophene (TT) moieties terminated with 2-hydroxybenzoic acid (see Figure 11) for initial examination. The fused TT building block serves to enforce the geometrical parameters required for the formation of the same SBU as the IRMOF-74 series while simultaneously narrowing the optical gap.

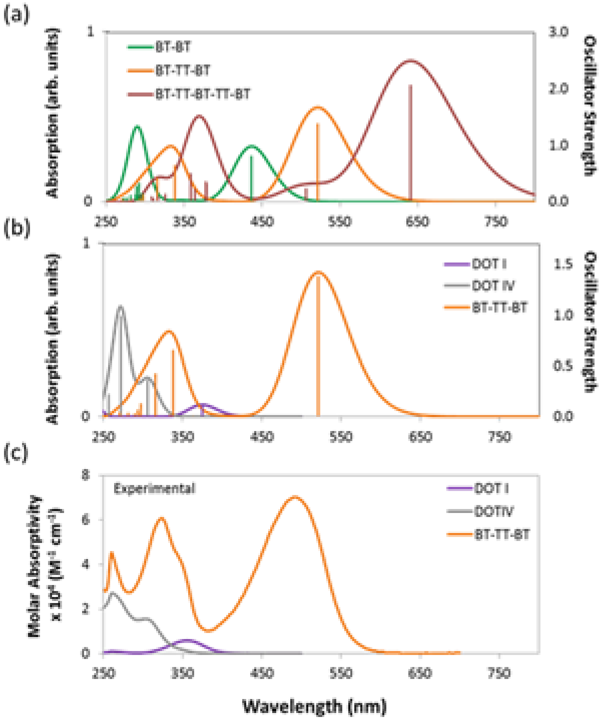

Figure 12. The TD/LC-BLYP/6-311G(d,p) predicted absorption spectra and oscillator strengths (represented by the vertical lines) of BT-BT, BT-TT-BT and BT-TT-BT-TT-BT (a). Figures (b) and (c) compare the predicted and experimentally determined absorption spectra of DOT I, DOT IV and BT-TT-BT (see SI for experimental details) respectively. The TDDFT predicted absorption spectra curves were determined by Gaussian convolution using a FWHM of 3000 cm^{-1}.

The predicted electronic properties of the proposed linkers (i.e. BT-BT, TT-TT, BT-TT-BT, and BT-TT-BT-TT-BT) (Table 1) demonstrate that this series provides the ability to tune relevant optoelectronic features, such as the optical gap, while maintaining overall linker symmetry. Due to the conjugated nature of these molecules, they exhibit optical gaps that are significantly reduced relative to their DOT counterparts and also larger oscillator strengths for the $S_0 \rightarrow\rightarrow S_1$ transition (see Table 1) compared to the DOT linker series. The emerging pattern indicates a decrease in the optical gap and an increase in the $S_0 \rightarrow\rightarrow S_1$ oscillator strength as the number of alternating BT/TT moieties increases. This is consistent with the frontier orbital energies becoming more closely spaced as the delocalization length increases. As a result, the BT-TT-BT-TT-BT linker has the smallest optical gap (1.9 eV) of the linkers considered. The predicted absorption spectra of BT-TT, BT-TT-BT and BT-TT-BT-TT-BT (Figure 12) illustrate that as the BT/TT length increases, the absorption shifts to the red with a concomitant increase in the oscillator strength, equivalent to an increase in molar absorptivity. The oscillator strength for the $S_0 \rightarrow S_1$ transition of BT-TT-BT-TT-BT ($f = 2.06$) is more than fivefold higher than DOT V ($f = 0.35$) and more than 17 times that of DOT I ($f = 0.11$), indicating considerably enhanced photon absorption efficiency. Notably, the TT-TT linker has a larger oscillator strength ($f = 2.16$) for the

$S_0 \rightarrow S_1$ transition than BT-BT ($f = 0.81$), but similar fundamental and optical gaps, owing to the more electron rich nature of the moiety. This demonstrates that a rapid increase in oscillator strength, hence increased photon absorption efficiency, can be achieved through linking just two TT moieties.

To validate our theoretical approach, we synthesized the BT-TT-BT linker (as its protected methyl ester) and characterized its optical properties (see SI for experimental details). This provides an essential benchmark for our theoretical predictions and represents a critical first step toward the rational design of this new class of MOFs. The experimental absorption spectrum of BT-TT-BT relative to the predicted non-empirically tuned LC-BLYP spectrum are compared in Figure 12. The experimentally determined absorption maximum (in dimethylformamide (DMF) at room temperature) for BT-TT-BT occurs at 490 nm, which is in good agreement with the predicted $S_0 \rightarrow S_1$ excitation occurring at 2.4 eV (521 nm). Although not directly related to the absorption maximum, the predicted optical gap is consistent with these spectra, differing from the experimental maximum by only 0.15 eV (31 nm).

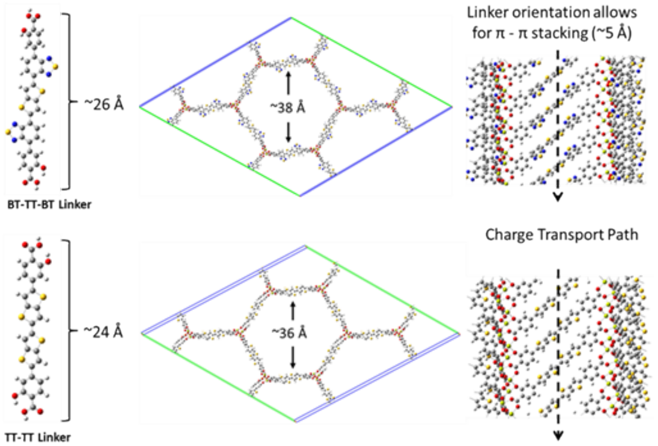

Figure 13. A schematic showing the BT-TT-BT and TT-TT optimized linkers, MOFs, linker length and pore cavity diameter, and the pi-pi stacking network.

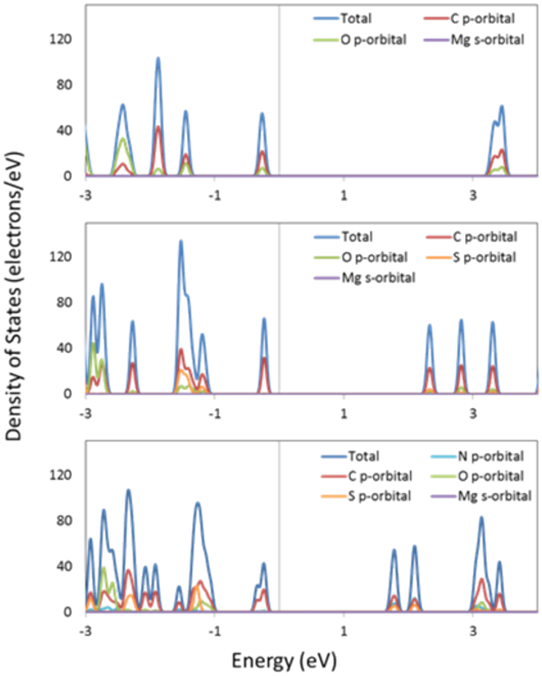

Figure 14. The total and partial density of states of IRMOF-74-II (top), IRMOF-74-TT-TT (middle), and IRMOF-74-BT-TT-BT (bottom). The Fermi energy has been placed at zero.

To ascertain whether the analysis of the isolated linkers can be related to the bulk MOF, we performed periodic DFT calculations for IRMOF-74-II(Mg), IRMOF-74-TT-TT(Mg), and IRMOF-74-BT-TT-BT(Mg). These systems were fully optimized at the DFT/PBE level of theory (optimized structures are shown in Figure 10 and Figure 13), followed by single-point calculations using the hybrid HSE06 functional. Hybrid functionals are well-known to more accurately predict bandgaps than GGA functionals (e.g. PBE); however, their use comes at significantly higher computational cost. The HSE06 (PBE) predicted bandgaps are 3.5 (2.5) eV, 2.5 (1.9) eV, and 2.0 (1.4) eV for IRMOF-74-II(Mg), IRMOF-74-TT-TT and IRMOF-74-BT-TT-BT respectively. The HSE06 values are systematically ~0.5 eV smaller than the predicted optical gaps of the isolated linkers; this difference can in part be attributed to the surrounding dielectric (solid vs. gas phase) but is also an artifact of the functionals themselves. Not unexpectedly, the PBE predicted bandgaps are even smaller; upwards of 1 eV compared to the HSE06 results. Importantly, however, the pattern is consistent between the different methods. The total and partial densities of states, shown in Figure 14, indicate that the frontier orbitals (valence and conduction band wavefunctions) are composed of C *p*-orbitals and have no contributions from the Mg valence *s*-orbital subshell. This indicates that the frontier orbitals are localized on the linkers; therefore, results predicted by considering the isolated linkers should provide an adequate representation of the electronic structure of the MOF. In the case of other metals that can be used to construct IRMOF-74 (Mn, Fe, Co, Ni, and Cu), however, the *d*-orbitals will likely be near the band edge, rendering this approximation invalid.

3.4. Discussion

The nanoporous nature of MOFs creates the potential to form a "nano-heterojunction," in which the framework serves as an electron-donating light absorber that is infiltrated with an electron acceptor. The advantage of this configuration is that it confines both the donor and acceptor within a highly ordered chemical environment that, in principle, can be synthetically tuned to optimize light harvesting, exciton splitting, and charge transport. The IRMOF-74 topology is an excellent starting point for designing semiconducting MOFs with appreciable porosity because of its proven synthetic modularity and structural properties that should promote charge transport. A key feature of its structure is that the linkers stack (~ 5 Å apart) in a perpendicular arrangement to form the sidewalls of the pores (see Figure 10), in contrast with other well-known frameworks where the linkers are electronically isolated from each other (e.g. MOF-5, MOF-177, and HKUST-1).[112] This provides a potential route for charge transport through the organic linkers of the MOF. Supporting this proposed mechanism are prior studies demonstrating charge transfer between MOF linkers that are closely spaced.[113-116] However, as our calculations show, the linkers comprising the IRMOF-74 series (DOT I-XI) have large optical gaps, small oscillator strengths, and improper orbital alignments with known electron donor materials. For example, the HOMO and LUMO orbitals of PCBM lie between that of the DOT linkers (see Figure 15); as a result, the IRMOF-74 series lacks the ability to absorb light in the visible region and transfer charge to PCBM. Recently, an alternative approach for predicting MOF band alignments, based on periodic DFT calculations, was proposed that allows for the conduction and valence bands of the MOF to be referenced to vacuum by taking advantage of the porous nature of the material.[117] Both methods provide only approximate values. Nevertheless, these carboxylate-based frameworks are expected to be insulators based on the magnitude of their band gaps, making it impossible to conduct charge into or out of the framework.

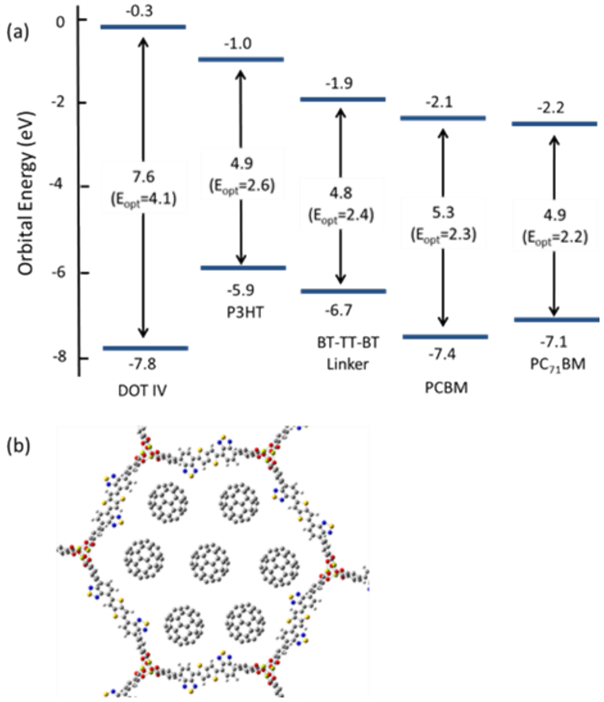

Figure 15. (a) HOMO/LUMO energies and fundamental and optical gaps of DOT IV, P3HT, BT-TT-BT, PCBM and PC$_{71}$BM predicted at the LC-BLYP/6-311G(d,p) level of theory (b) and a schematic illustrating how ample loading of PCBM or PC$_{71}$BM (C$_{60}$ was used for illustrative purposes) within the 1D pore channels of IRMOF-74-BT-TT-BT(Mg) is plausible.

In contrast, the electronic structure of the linkers in the series proposed here is designed for efficient light harvesting and to promote charge transport within the IRMOF-74 network. These molecules have the proper band alignment with known electron acceptors such as PCBM and PC$_{71}$BM, in that the HOMO (LUMO) of the linker, acting as an electron donor, is positioned below (above) the HOMO (LUMO) of the acceptor. We focus in this discussion regarding band alignment and CT on the BT-TT-BT linker for two reasons. First, its length will create large channels that facilitate infiltration of guest molecules and second, it has more favorable electronic properties than the linkers containing only the BT and TT moieties. As seen in Figure 15, the predicted band alignments of the BT-TT-BT linker with respect to PCBM and PC$_{71}$BM indicate that this linker can act as an electron donor to either of these acceptors. Its light-absorbing properties (optical gaps and oscillator strengths) are also similar to those of P3HT (see Table 1), a well-known electron donor used in OPV. Notably, the linker/fullerene offset is close to the "ideal" donor/acceptor LUMO offset[73, 118] of 0.3 eV (0.2 and 0.3 eV for PCBM and PC$_{71}$BM respectively), which is important for efficient exciton splitting. In contrast, the predicted LUMO offset between P3HT is much too large (1.1 eV for PCBM, which is in excellent agreement with the experimental value of 1.0 eV[73]). The predicted BT-TT-BT optical gap (2.4 eV) is also somewhat smaller than that of P3HT (2.6 eV), which is heading closer to the optimal bandgap of 1.5 eV for polymer absorbers used in OPV applications.[73] As our calculations show, the proposed BT-TT-BT-TT-BT linker approaches this ideal value. Together, these properties support our hypothesis that rigid MOF linkers comprised of alternating BT and TT groups are a promising strategy for synthesizing MOFs for exciton-based light harvesting and charge separation.

Additional evidence that charge transfer can occur between IRMOF-74-BT-TT-BT(Mg) and a fullerene derivative was obtained from TDDFT calculations of the 2xBT-TT-BT@ $PC_{71}BM$ cluster model, which is representative of a fullerene guest within the MOF pore. The constrained optimized structure is shown in Figure 16 along with images of the HOMO and LUMO. The localization of the HOMO on the linkers and the LUMO on $PC_{71}BM$ indicates that charge transfer will occur upon absorption of photons with wavelengths of ~ 500 – 700 nm. In addition, charge difference density (CDD)[46] maps were generated for several of the dominant optically active transitions (see images within the absorption spectrum plot of Figure 16). CDD maps enable visualization of the change in electron density upon excitation. These images show an increase in electron density on $PC_{71}BM$ upon excitation, as represented by the light blue lobes, and a decrease in electron density on the linkers, as represented by the purple lobes. This is a clear indication that charge transfer should occur between IRMOF-74-BT-TT-BT(Mg) and $PC_{71}BM$.

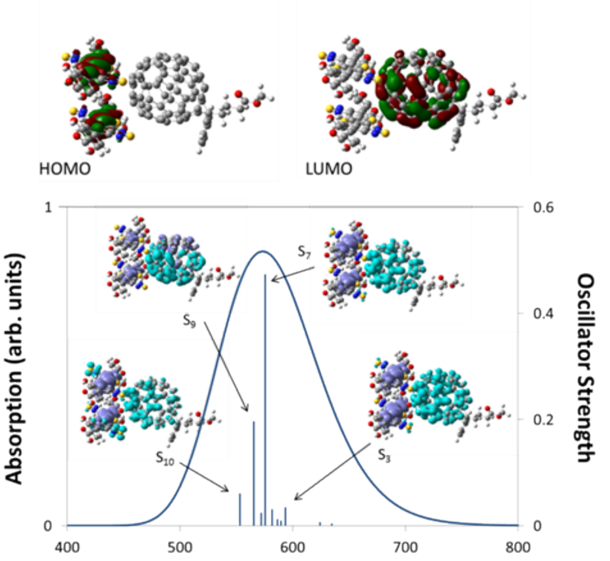

Figure 16. The HOMO, LUMO and the TDDFT (LC-BLYP/6-31G(d,p)) predicted absorption spectrum of 2xBT-TT-BT@$PC_{71}BM$. The molecular images with the absorption spectrum plot show the change in electron density upon excitation (CCD maps). The purple and light blue regions represent a decrease (holes) and increase (electrons) in the electron density respectively.

In addition to proper band alignment, access to the pores and the ability to achieve high loading of electron acceptor molecules within them must be achievable to create an effective nano-heterojunction structure using a MOF. A dense acceptor loading is also needed to achieve the good orbital overlap between infiltrated acceptor molecules required for high charge mobility. The proposed IRMOF-74 variants have large 1D pore diameters, measuring ~38 Å and ~36 Å for IRMOF-74-BT-TT-BT and IRMOF-74-TT-TT, respectively (Figure 13), which is sufficient to accommodate several fullerene molecules within the horizontal plane perpendicular to the pore channel (Figure 15b). As these pores are one-dimensional channels, the pore limiting diameter (PLD) is the same as the largest cavity diameter (LCD). Diffusion of molecules this size into the pores should thus be rapid, as we demonstrated in a previous investigation of PCBM infiltration into MOF-177.[69] In that case, the MOF LCD was ~24 Å, but the PLD was only ~16 Å, less than half that of IRMOF-74-BT-TT-BT and IRMOF-74-TT-TT. Nevertheless, nearly immediate PCBM uptake was observed upon exposure to a saturated solution, producing high loadings (22 wt%) comparable to those in BHJ OPV devices. We therefore expect that fullerene domains will form that are similar to those in conventional BHJ systems, but with more long-range order because the fullerene is confined within the 1D channels of the MOF. In a hypothetical thin-film BHJ device having a structure in which the MOF pore channels are perpendicular to the terminal contacts (anion/cathode), all the fullerene/acceptor and MOF/donor domains will have a continuous and direct path out of the active layer. In addition, the pores will confine the acceptors to be at most 20 Å (2 nm) from a donor, well within the maximum exciton diffusion length of 10 nm,[73] which is a major benefit of a MOF-based photovoltaic devices. Using the MOF as the electron donor, there would be virtually no exciton diffusion required if the pore channels are packed with fullerenes or any other acceptable electron acceptor with appropriately aligned electronic properties.

3.5. Conclusions

The proposed BT/TT series of linkers represent a new, previously unexplored class of MOFs that can be tailored specifically for light-harvesting with properties similar to those of well-studied organic semiconductors. Quantum mechanical periodic and molecular orbital calculations, including TDDFT using novel non-empirically tuned range-separated functionals, were used to extensively characterize their properties. This approach, which combines high-level theoretical treatments with bottom-up material design, represents an important step towards the synthesis of MOFs tailored for optoelectronic applications. We demonstrated that this modular BT/TT series is capable of forming the same infinite metal-oxide SBU as IRMOF-74, allowing a continuous π-π stacking network to be formed that could provide a route for high charge mobility. In these IRMOF-74 analogues, the linker is not merely structural, but is tuned to enable it to function as both a light harvester and an electron donor to electron acceptor molecules infiltrated within the pores. We expect, therefore, that light harvesting by these MOFs will be considerably more efficient than in typical carboxylate-type MOFs, which absorb primarily in the UV. As demonstrated, these linkers absorb visible light due to their relatively small optical gaps and large oscillator strengths, both of which agree well with experimentally determined trends and measured values. In addition, our results show that proper band alignment exists with well-known acceptor molecules, such as PCBM, to enable exciton splitting. Finally, the confinement of the acceptor molecules within the MOF should reduce the exciton migration distance considerably compared with typical bulk heterojunctions, a current factor that limits OPV performance.

The proposed MOF series and theoretical analysis represent a rational approach for predicting trends and guiding experimental efforts to develop MOF-based photovoltaic devices and functional electronic materials. The modularity of the proposed linker series allows for any BT/TT combination and pore diameter to be readily synthesized, affording the ability to systematically tune both the structural and electronic properties. Our results also demonstrate that accurate trends can be predicted from calculations based solely on the linkers, as long as the system is comprised of closed-shell metal ions such as Mg(II) that do not make orbital contributions near the band edges. Further modeling and experimental analyses are also underway to determine the charge transport characteristics of these MOFs. We are currently extending our approach to other potential organic linkers and MOF architectures that are expected to have favorable electronic properties for light harvesting, enhanced charge carrier mobility, minimal exciton diffusion distances, and high orbital overlap between adjacent linkers. Such architectures are promising not only for MOF-based solar cells, but also as well-controlled platforms for obtaining valuable fundamental knowledge regarding donor-acceptor interfaces, exciton diffusion lengths, and carrier mobility, due to the inherent structural order and nanoconfinement available in MOFs. Synthesis of these MOFs is currently underway in our laboratory.

4. TUNABLE ELECTRICAL CONDUCTIVITY IN METAL-ORGANIC FRAMEWORK THIN-FILM DEVICES

4.1. Main Text

MOFs (*1-3*) are crystalline materials with a nanoporous, supramolecular structure consisting of metal ions connected by multitopic organic ligands. These materials are typically poor electrical conductors because of the insulating character of the organic ligands and poor overlap between their π orbitals and the d orbitals of the metal ions. Combining the crystalline order of MOFs with an ability to conduct electrical charge has the potential to create a new class of materials that would open applications such as conformal electronic devices, reconfigurable electronics, and sensors. Although strategies to engineer electrically conducting MOFs have been proposed (e.g., the use of second- or third-row transition metals, redox-active linkers, and hetero-bimetallic structures), few of these approaches have been realized (*4*). Until recently, only one example of an intrinsically conducting framework with permanent porosity was known, a p-type semiconducting MOF in which conductivity occurs via a redox mechanism (*5*). Very recently, Gandara *et al.* described a series of metal triazolate MOFs, one of which exhibits ohmic conductivity (*6*). The mechanism of conductivity in that case is not known, but it appears to be highly specific to the presence of Fe(II) in the structure, as MOFs in this series with the same structure but different divalent metals are not conducting. Importantly, there have been no reports of conducting MOF thin-film devices.

An alternative approach is to use the MOF pores themselves as a venue for modulating the electrical transport properties. We reasoned that infiltrating MOFs having open metal sites with molecules capable of charge transfer that can coordinate to these sites would create a mechanism for carrier mobility. Binuclear Cu(II) paddlewheel MOF structures, such as $Cu_3(BTC)_2$ (*7*) (also known as HKUST-1), are attractive candidates for testing this strategy. The coordination positions located on opposite ends of the Cu(II) axis of the paddlewheel, which are occupied by solvent (often water) in the as-synthesized material, can be exchanged with redox-active molecules such as TCNQ. Moreover, electron paramagnetic resonance (EPR) spectra suggest a somewhat delocalized electronic structure enabled by additional spin exchange among the copper dimers, which results from the carboxylates interconnecting the paddlewheel subunits (*8*).

Here, we describe the realization of this strategy using a thin-film device comprised of $Cu_3(BTC)_2$ (*7*) grown on electrodes and demonstrate control of ohmic electrical conductivity over six orders of magnitude. Silicon wafers covered with 100 nm of SiO_2 were pre-patterned with 100 nm-thick Pt pads (dimensions of 800 μm by 400 μm) and gaps of 100 μm, 150 μm, and 200 μm. $Cu_3(BTC)_2$ films with 100 nm nominal thickness were grown on the wafers from the liquid phase, as described previously (*9*). Grazing incidence XRD measurements and SEM imaging (Figure 17, B and C) indicate a polycrystalline $Cu_3(BTC)_2{\cdot}xH_2O$ film with preferred orientation along the (111) direction (*10*). Current-voltage (I-V) characteristics obtained on as-grown thin-film devices in air (Figure 18A) exhibited very low conductivity (~ 10^{-6} S/m), consistent with the expected insulating nature of $Cu_3(BTC)_2$.

The as-grown films were infiltrated with TCNQ by first heating in vacuum at 190 ºC for 30 min to remove coordinated water molecules, then immediately transferred to a saturated TCNQ/CH_2Cl_2 solution. I-V curves for four such devices after 72 hours of exposure to the TCNQ solution [Figure 18A and supplemental online materials (*11*)]. The infiltration led to dramatic increases in current, with a linear I-V curve and conductivity of 7 S/m, six orders of magnitude greater than the un-infiltrated device. Measurements as a function of channel length (Figure 18B) revealed a monotonic increase in resistance with increasing electrode separation. The TCNQ-infiltrated devices were stable in ambient up to at least 40 days (Figure 18C). The conductivity increases with temperature (Figure 18, D and E), following a thermally activated relation $\sigma \sim \exp(E_a/T)$ with a low activation energy E_a of 41±1 meV, similar to values reported for high-mobility organic polymeric semiconductors such as poly-3-hexylthiophene (P3HT) (*12*).

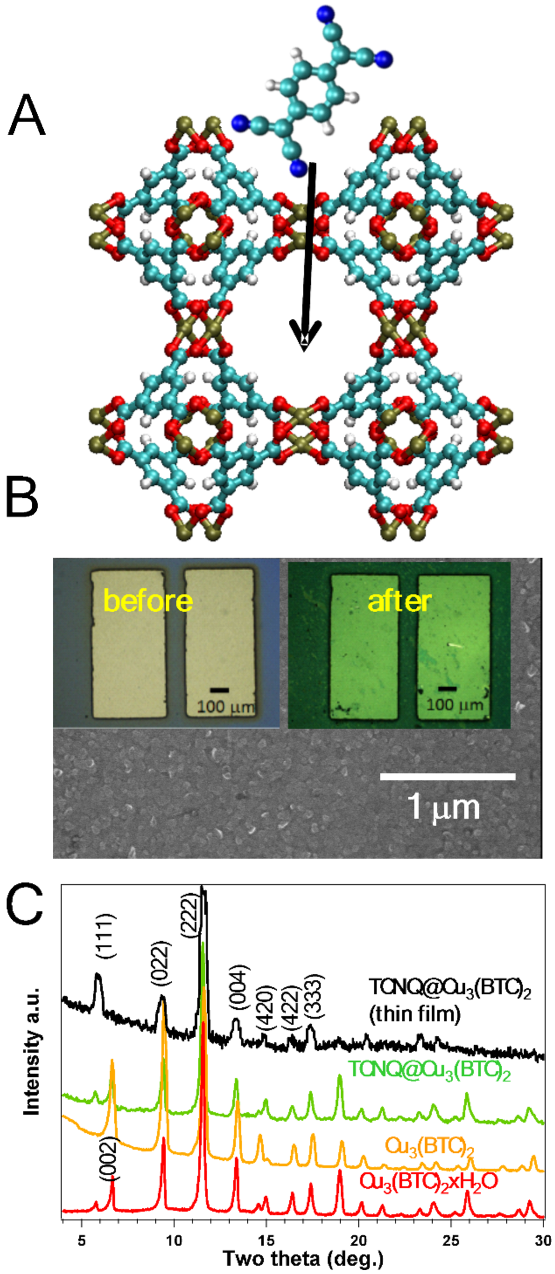

Figure 17. Fabrication of conductive MOF thin-film devices and structural characterization. (A) TCNQ molecule shown above a $Cu_3(BTC)_2$ MOF; arrow points into the pore. White – hydrogen; blue – nitrogen; cyan – carbon; red – oxygen; light brown – copper. (B) SEM image of MOF-coated device, with optical images of devices before and after TCNQ infiltration. (C) XRD data for powders and grazing incidence XRD for a thin film.

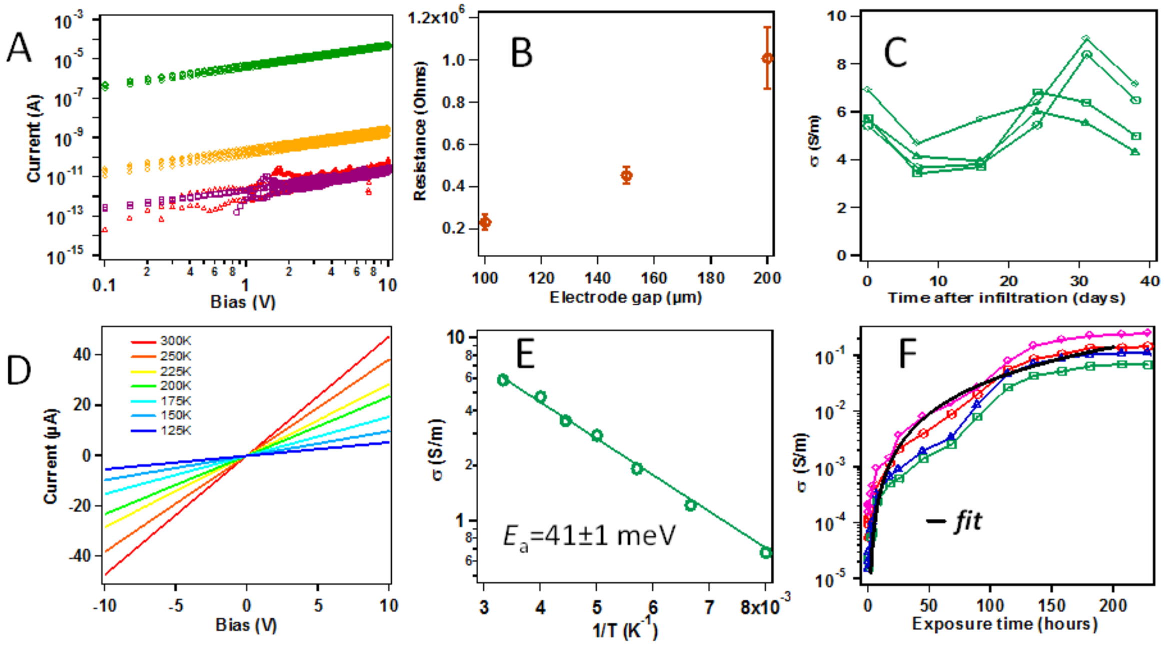

Figure 18. Electronic transport characteristics of MOF thin-film devices. (A) I-V curves before (red) and after infiltration with: TCNQ (green); F4-TCNQ (gold); H4-TCNQ (purple). (B) Channel-length dependence of conductivity for TCNQ-infiltrated devices. (C) Stability of conductivity over time for several devices. (D) I-V curve temperature dependence. (E) Arrhenius plot of the conductivity. (F) Conductivity vs. exposure time for several devices. Black line: fit to percolation theory, $\sigma = 4\times10^{-6}(t-0.5)^2$ where t is exposure time.

In contrast to previously reported, non-porous conducting coordination polymers, such as CuTCNQ (*12-15*), we could tune the device conductivity by changing the TCNQ exposure time. As seen in Figure 18F, conductivity variation over several orders of magnitude was achievable. Furthermore, the increase in conductivity could be described by classic percolation theory (black solid line) (*16*), suggesting that TCNQ forms localized conducting regions, rather than acting as a dopant.

Chemical and physical characterization of MOF films and powders exposed to TCNQ verify that TCNQ resides in the MOF pores without altering the MOF crystal structure. Powder XRD patterns of as-synthesized $Cu_3(BTC)_2{\cdot}xH_2O$, $Cu_3(BTC)_2$ (activated), and $Cu_3(BTC)_2$ infiltrated with TCNQ [hereafter TCNQ@ $Cu_3(BTC)_2$] showed that the MOF crystalline structure (face-centered cubic) was unaffected by the infiltration process (Figure 17B) (*7*). Rietveld refinement yielded lattice parameters of 2.617 nm ± 0.001 nm and 2.635 nm ± 0.001 nm for $Cu_3(BTC)_2$ and TCNQ@ $Cu_3(BTC)_2$ powders, respectively. The peak at 2θ=5.759° seen in the patterns of both $Cu_3(BTC)_2{\cdot}xH_2O$ and TCNQ@$Cu_3(BTC)_2$ (but absent from that of activated MOF) is diagnostic for guest molecule binding to the open metal sites in the large pores, and indicates long range order *(17)*. The surface area of the activated $Cu_3(BTC)_2$ powder, obtained from N_2 adsorption isotherms using the Brunauer, Emmett, and Teller (BET) method, is 1844 m2 g-1 ± 4 m2 g-1. This value is typical of high-quality $Cu_3(BTC)_2$ 3*Fm*_*m* material with little or no pore collapse or residual reactant (*18*). After infiltration and drying in air, the TCNQ@$Cu_3(BTC)_2$ material displays a BET surface area of 214 m2 g-1 ± 0.5 m2 g-1, suggesting high TCNQ loading. This result is confirmed by elemental analysis indicating a $Cu_3(BTC)_2$:TCNQ ratio of 2 based on carbon, nitrogen, and hydrogen content. This corresponds to about 8 TCNQ molecules per unit cell or 1 TCNQ molecule per MOF pore. The presence of nitrogen in the TCNQ@$Cu_3(BTC)_2$ films was further corroborated by x-ray photoelectron spectroscopy (XPS). Furthermore, visual examination of the powdered MOFs reveals the expected turquoise-blue color for the as-synthesized material and the violet-blue hue for the activated (dehydrated) MOF. Upon exposure to TCNQ, the color of the crystals changes to teal, indicating a perturbation of the MOF electronic structure. The color of TCNQ@$Cu_3(BTC)_2$ does not change upon exposure to air suggesting that TCNQ is not displaced by atmospheric water vapor; XPS also showed a significantly lower oxygen concentration in the infiltrated specimen consistent with reduced water occupation of the pores. In contrast, the color of the activated MOF prior to TCNQ infiltration reverts almost instantly to that of the as-synthesized (hydrated) material when exposed to atmospheric moisture.

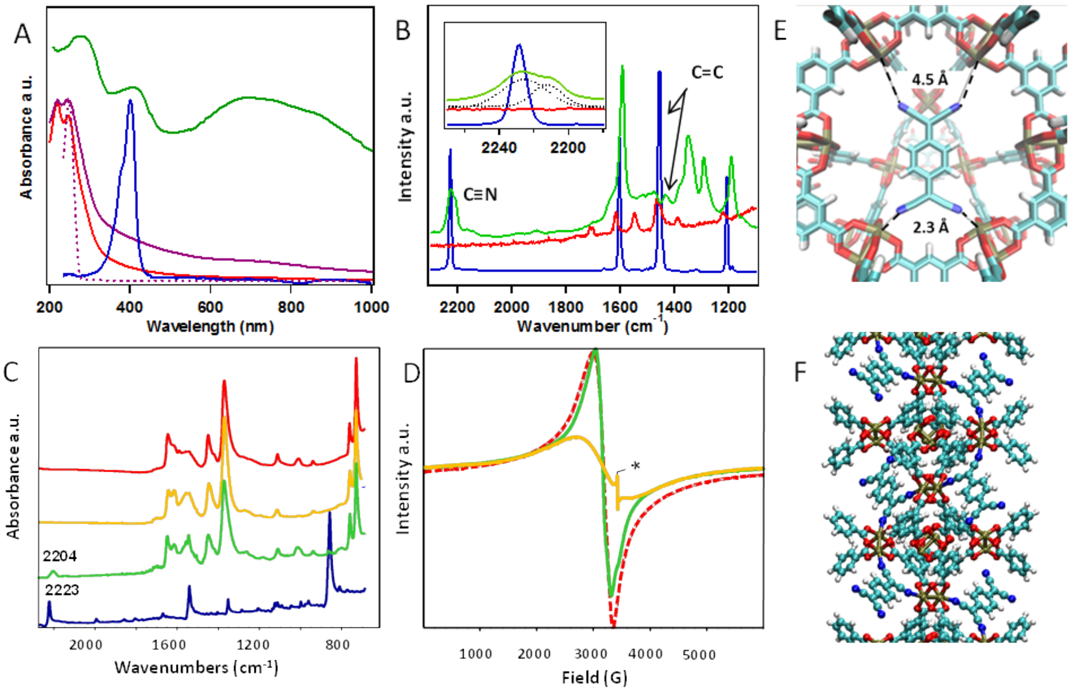

Figure 19. Evidence for interaction between TCNQ and the MOF. (A) Transmission UV-Vis spectra collected for a $Cu_3(BTC)_2 \cdot xH_2O$ film on borosilicate substrate before (red) and after adsorption with TCNQ (green) and H4-TCNQ (purple), and for TCNQ in methanol (blue); (B) Raman spectra collected for a $Cu_3(BTC)_2 \cdot xH_2O$ film on borosilicate substrate before (red) and after adsorption of TCNQ (green), and for TCNQ crystals deposited onto a glass slide (blue); (C) infrared spectra collected for $Cu_3(BTC)_2 \cdot xH_2O$ (red), $Cu_3(BTC)_2$ (yellow), TCNQ@$Cu_3(BTC)_2$ (green), and TCNQ powder (blue); (D) room temperature continuous wave EPR spectra of activated $Cu_3(BTC)_2$ (yellow), $Cu_3(BTC)_2$ stirred in methanol (red dashed), and $Cu_3(BTC)_2$ stirred in methanol containing TCNQ (green). The asterisk (*) denotes an unidentified organic radical signal observed only in the activated $Cu_3(BTC)_2$ sample. (E) Minimum energy configuration for TCNQ@$Cu_3(BTC)_2$ obtained

from ab initio calculations. (F) Possible configuration that would provide a conductive channel through the MOF unit cell (atom color code for E and F as in Figure 17).

The realization of these new hybrid electronic materials raises a question concerning the nature of the interaction between the framework and TCNQ and the mechanism of charge transport. We probed the TCNQ/MOF interaction several ways. Ultraviolet-visible (UV-Vis) spectra were collected from films of the uninfiltrated $Cu_3(BTC)_2{\cdot}xH_2O$, TCNQ@$Cu_3(BTC)_2$, and TCNQ in dilute solution. The absorption spectrum of the TCNQ@$Cu_3(BTC)_2$ film (Figure 19A) exhibits the expected MOF peak at 340 nm, a peak at 410 nm associated with neutral TCNQ,(*18*), and broad new absorption bands centered at ~700 nm and ~850 nm that are absent in both $Cu_3(BTC)_2{\cdot}xH_2O$ and TCNQ in CH_2Cl_2. These additional bands are well-known signatures for charge transfer (*13, 19*). Note that reacting either copper acetate or copper sulfate with TCNQ in methanol generated no precipitates or new absorption bands, indicating that confinement in the MOF pore is essential to the formation of a charge transfer complex between Cu(II) and TCNQ. TCNQ complexes have been characterized extensively by vibrational spectroscopies, where the frequencies of C=C and C≡N stretching modes are particularly sensitive to the extent of charge transfer (*13, 20, 21*). Raman spectra of TCNQ@$Cu_3(BTC)_2$ (Figure 19B) indicate that the TCNQ C=C stretching frequency shifted from 1456 cm-1 to 1437 cm-1 and new peaks appeared at 1352 cm-1 and 1296 cm-1, a strong indication that TCNQ interacts with the available coordination sites on the Cu^{2+} ions in the framework. A shift of 19 cm-1 for the C=C wing stretching mode suggests a partial charge transfer of ~0.3e^- between the framework and TCNQ(*20*). The nitrile stretch at 2229 cm-1 is split into two peaks at 2226 cm-1 and 2213 cm-1 (see inset), indicating two non-equivalent C≡N bonding environments, in close agreement with our calculated vibration spectra *(11)*. IR spectra (Figure 19C) also show that the C≡N stretch of TCNQ is affected by adsorption into the framework with a shift from 2223 cm-1 to 2204 cm-1 accompanied by significant peak broadening. According to Chappell *et al.* (*21*), this shift corresponds to a charge transfer of ~0.4e- between the framework and TCNQ, in reasonable agreement with the value inferred from the Raman spectra. The observation of partial charge transfer is further supported by room temperature EPR spectra obtained from TCNQ@$Cu_3(BTC)_2$ (Figure 19D), which display no evidence of TCNQ radical anions (*22*). Partial charge transfer is characteristic of many conducting TCNQ salts; however, in contrast to the well-studied CuTCNQ, in which Cu(+1) predominates, Cu in $Cu_3(BTC)_2$ remains in (+2) state after infiltration, as revealed by XPS.

The importance of guest/host interactions was further probed by replacing TCNQ with its fully hydrogenated counterpart, H4-TCNQ (cyclohexane-1,4-diylidene)dimalononitrile), which lacks a conjugated π electron network, and F4-TCNQ (2,3,5,6-tetrafluoro-7,7,8,8-tetracyanoquinodimethane), which has a similar HOMO-LUMO gap but higher electron affinity compared to TCNQ. Elemental analysis indicates that the loading of H4-TCNQ is similar to that of TCNQ, i.e., about 1 H4-TCNQ molecule per pore. The I-V curve (Figure 18A) for H4-TCNQ@$Cu_3(BTC)_2$ is essentially the same as the uninfiltrated, non-conducting MOF. The UV-Vis spectrum also lacks the characteristic bands indicative of charge transfer in TCNQ@ $Cu_3(BTC)_2$ (Figure 19A). These results illustrate that the availability of guest molecule orbitals that can accept charge, as is the case in TCNQ but not H4-TCNQ, is important for achieving high conductivity. F4-TCNQ@ $Cu_3(BTC)_2$ is not as conductive as TCNQ@$Cu_3(BTC)_2$. We view this result as semi-quantitative, however, because F4-TCNQ is volatile and unlike TCNQ@

$Cu_3(BTC)_2$, the conductivity was not stable with time. Nevertheless, the lower conductivity measured immediately after infiltration suggests that the high electron affinity of this molecule inhibits electron mobility.

Finally, ab initio calculations suggest a possible mechanism for the appearance of conductance in TCNQ@ $Cu_3(BTC)_2$ hybrids. As illustrated in Figure 19E, the calculations predict that TCNQ binds strongly to the MOF (binding energy of 83.9 kJ/mol) and four such molecules create a continuous path through the unit cell (Figure 19F). Furthermore, our calculations using molecular clusters comprised of two copper dimer groups (MOF SBUs) bridged by a TCNQ molecule show that: 1) the bridging TCNQ inserts unoccupied molecular orbitals into the MOF HOMO-LUMO gap (discussion), producing the new charge transfer band in the visible and enabling electronic coupling between the MOF and TCNQ. 2) Computed values of HAB, the electronic coupling matrix element for electron transfer from the MOF cluster to TCNQ (i.e. TCNQ@$Cu_3(BTC)_2^-$ → $TCNQ^-$@$Cu_3(BTC)_2$)), combined with the value of ΔG^* obtained from the temperature dependence of the conductivity, allow us to evaluate the extent of donor-acceptor coupling using the quantity $2H$AB/λ defined by Brunschwig *et al.* (λ is the reorganization parameter) (*19*). We find $2H$AB/$\lambda = 1.21$ for TCNQ@$Cu_3(BTC)_2$, identifying this material as a Class III system according to the Robin-Day classification scheme *(19*). These calculations also predict that electronic coupling in F4-TCNQ@$Cu_3(BTC)_2$ is intermediate between H4-TCNQ and TCNQ itself. The order of HAB values is H4-TCNQ < F4-TCNQ < TCNQ (0.19 eV < 1.03 eV < 2.32 eV), a trend that is consistent with the observed conductivities.

5. CONTROLLED NUCLEATION AND GROWTH OF PILLARED PADDLEWHEEL FRAMEWORK NANOSTACKS ONTO CHEMICALLY MODIFIED SURFACES

5.1. Introduction

Metal organic frameworks (MOFs) are porous crystalline structures formed from the highly ordered co-assembly of metal cations with coordinating ligands on functional or structural organic molecules. These materials are attractive for numerous applications, including gas storage,[119, 120] gas separation,[120, 121] catalysis,[121, 122] and sensors[120, 121] due to their high surface areas and specific and tunable chemical functionalities. Fully realizing the potential utility of these versatile materials, however, requires their effective integration onto optically or electrically-addressable substrates.[121, 123] In the present work, demonstrate the surface-nucleated, solvothermal growth of a model porphyrin-based MOF, porphyrin paddlewheel framework 5 (PPF-5), using versatile surface chemistries to mediate PPF-5 nucleation on acid-functionalized surfaces. PPF-5 is a member of a family of pillared MOFs containing metalloporphyrin paddlewheel linkers that introduce additional metal centers to control ligand binding and framework topology.[124] The introduction of porphyrins into these assemblies adds potentially valuable optically active or catalytic character.[125] Although porphyrin-containing MOFs have been synthesized and explored as bulk crystals,[124, 126-129] and their properties explored[130-132] and modified,[129, 133] the solvothermal growth of these materials on functionalized semiconducting surfaces represents a new extension of this PPF-5 growth.

The controlled nucleation of MOFs on surfaces is a non-trivial endeavor, and the extent of this emerging field has been reviewed in considerable detail by Betard and Fischer.[134] Many of the approaches for growing MOF coatings on surfaces for device applications are focused on layer-by-layer deposition techniques;[125, 135-138] however, straightforward approaches, such as the direct nucleation and growth of MOF crystals and thin films onto chemically functionalized substrates, remain attractive due to their simplicity and potential scalability. Reported demonstrations of solvothermal nucleation and growth of MOFs on functionalized surfaces are relatively scarce, although there has been some demonstrated success growing MOFs such as HKUST-1 ($Cu_3(btc)_2$),[139, 140] MOF-5 ($Zn_4O(bdc)$),[141] CAU-1 ($(Al_4(OH)_2(OCH_3)_4(H_2N\text{-}bdc)_3 \cdot xH_2O)$)[142] and Fe-MIL-88B[143] on gold surfaces coated with acid-terminated self-assembled monolayers (SAMs).

Here, we extend the surface functionalization concept to porphyrin paddlewheel MOFs, using PPF-5 as a model compound and demonstrate nucleated growth on silicon and titanium dioxide, two technologically relevant substrates. Selective PPF-5 nucleation and growth was enabled by carboxylate surface chemistries produced using diazonium and catechol chemistries to modify Si and titania surfaces, respectively. Without the resulting surface carboxylate groups, no PPF-5 growth occurs, showing that selective growth should be feasible using a variety of surface patterning methods. These chemical approaches also expand the repertoire of surface functionalization chemistries for MOF nucleation beyond self assembled monolayers attached to gold or covalently bound using siloxane chemistry.[134] Using these alternative chemical approaches to surface modification broadens the potential applicability of MOF thin films as they allow for functionalization of a diverse range of metal,[144, 145] semiconductor,[144, 146, 147] and oxide surfaces.[147-149] Moreover, we describe how the synthesis temperature affects the morphology of the MOF architectures and correlate the variation in morphology with changes in the optical properties of these supramolecular materials.

5.2 Experimental

Materials: Palladium (II) meso-tetrakis(4-carboxyphenyl)porphine (Pd-TCPP) was obtained from Frontier Scientific. Cobalt nitrate hexahydrate ($Co(NO_3)$□$6H_2O$), 4,4'-bipyridine (bipyridine), N,N-diethyl formamide (DEF), and 3,4-Dihydroxybenzoic acid (DHBA) and phosphate buffered saline (PBS) salts were purchased from Sigma Aldrich and used as received.
Substrate preparation: All silicon wafers were piranha cleaned (3:1 H_2SO_4:30%H_2O_2) prior to use or further functionalization. After piranha cleaning, silicon wafers were then immersed in a 5% hydrofluoric acid solution for at least 20 minutes to remove the oxide and expose the bare Si surface. The wafers were then thoroughly rinsed with deionized water, dried with nitrogen, and used within 10 minutes of preparation. Modification of silicon surfaces with p-carboxyphenyldiazonium tetrafluoroborate was performed according to previously published protocols.[144] The substrates were then rinsed with water and ethanol and dried with nitrogen.
Approximately 20 nm of titania were deposited onto Si wafers using atomic layer deposition (Savannah ALD System, Cambridge Nanotech) of alternating $TiCl_4$ and H_2O pulses. After deposition, the titania was heated to 300 °C for 30 minutes in air and then ozone treated for 10 minutes prior to use. DHBA-functionalization was performed by immersion in a 10 mM solution of DHBA in pH 7 PBS for 2 hours. The substrates were then washed in deionized water and dried with nitrogen.

PPF-5 synthesis: Synthesis of PPF-5 crystals was performed using a previously published method.[124] In a typical synthesis, a substrate was inserted vertically into a solution consisting of 9.2 mg (0.01 mmole) Pd-TCPP, 8.8 mg (0.03 mmole) $Co(NO_3)$□ $6H_2O$, and 2.8 mg (0.01 mmole) 4,4'-bipyridine dissolved in a solvent mixture containing 1.5 mL DEF and 0.5 mL ethanol. This solution was then heated to 60, 80, or 100°C for 24 hours. After growth, the samples were removed from the growth solution and rinsed with DEF and ethanol to remove remnant reagent and any sedimented PPF-5 crystals.

Characterization: Static contact angle measurements were collected on a Kruss DSA Mk1 Instrument. Scanning electron microscope (SEM) analysis was performed on a Zeiss Supra 55VP Field Emission SEM. Micro-photoluminescence was collected during fluorescence imaging under green band excitation (510-550nm) and collection of light with wavelengths longer than 590nm on an optical microscope fitted with a spectrometer. A Siemens model D500 □-2□ powder diffractometer (Bruker AXS, Inc. Madison, WI) was used for Grazing-Incidence X-ray Diffraction (GIXRD) data collection with samples maintained at room temperature (25°C). Monochromatic Cu K□ (0.15406 nm) radiation was produced using a diffracted-beam curved graphite monochromator. Fixed 0.3° incident beam and scatter slits were used (goniometer radius = 120 mm), and the instrument power settings were 40 kV and 30 mA. Datascan V4.3 (Materials Data Inc.; Livermore, CA) software was used to operate the diffractometer. Powder diffraction patterns were collected using a fixed q angle of 1° and scans were collected as follows: 2-40° 2□

range, step-size of 0.04° 2□ and a count time of one second. Each PFF5 sample (grown on a Si substrate) was drawn directly out of solvent solution and mounted on an XRD sample holder within 1 minute and subsequently loaded onto a diffractometer for XRD analysis. Diffraction patterns were collected with a thin layer of N,N-diethylformamide covering the surface to prevent structural collapse of the MOF due to drying effects. X-ray photoelectron spectroscopy (XPS) was performed with a Kratos Axis Ultra DLD instrument with base pressures less than 5 x 10^{-9} Torr. A monochromatic Al Kα (1486.7 eV) source was used at 300 W. The analyzer was used in Hybrid mode with a pass energy of 160 eV for survey spectra and 20 eV for high resolution spectra. The analysis area was an elliptical 300 x 700 microns for each sample. Survey spectra were taken with 1000 meV step sizes and 100 ms dwell times. The C 1s peaks were recorded with 30 meV step sizes and 100 ms dwell times. Data processing was performed with CasaXPS. C 1s peak fitting was performed with a Shirley background and Gaussian/Lorentzian (70/30) peaks.

5.3 Results & Discussion

PPF-5 consists of planes of carboxylic acid-decorated palladium-containing metalloporphyrins coordinated to Co^{2+} and 4,4'-bipyridine pillars linking parallel planes. Since PPF-5 contains metal ions coordinated to electron-donating and/or anionic groups, we hypothesize that acid-decorated surfaces will to promote the nucleation and growth of MOFs containing these functional groups on their linkers.[3] In this work, we examine the effects of carboxylic acid functionalities on the nucleation and growth of PPF-5 on both Si and titania surfaces. Si was modified with p-carboxyphenyldiazonium tetrafluoroborate. Titania, deposited by atomic layer deposition on Si wafers, was functionalized using 3,4-dihydroxybenzoic acid (DHBA). Effective surface modification was verified by contact angle measurements, Table S1 in supporting information. The presence of carboxylic acid moieties on these functionalized surfaces was confirmed by XPS, determined by examination of the C 1s spectra. In addition to the major XPS peak at 284.6 eV expected for the C-C environment in these samples, the XPS spectra revealed peaks at 288.7 eV and 288.8 eV for the DHBA-modified titania and carboxyphenyl-modified Si, respectively, indicating the presence of carboxylic acids.[150-152] Deconvoluted XPS spectra taken from these samples may be seen in supporting information.

Heterogeneous nucleation and growth of PPF-5 was performed on vertically oriented substrates immersed within a reagent solution for solvothermal crystal growth. Figure 20 shows SEM images of PPF-5 crystals grown at 80^{o}C for 24 hours onto carboxyphenyl-modified Si (a, b) and DHBA-modified titania (c,d). On both substrates, crystals grown at 80^{o}C appeared as stacks of rectangular plates. Although the majority of crystals were nucleated directly on the substrate surfaces, there was some evidence of secondary crystal nucleation off existing crystals. The dimensions of these plates vary from ca. $1\mu m^2$ to ca. $100\mu m^2$, while the height of the stacks approaches ca. 3-5µm. In contrast to the acid-modified surfaces, unmodified Si and titania surfaces (Figure 20e, Figure 20f) show no significant PPF-5 crystal growth. Fluorescence emission is also observed throughout the PPF-5 crystals, seen in the fluorescence microscope image insets of Figure 20a and Figure 20c, which verifies the incorporation of the photoactive Pd-containing metalloporphyrin throughout the crystals. That the PPF-5 growth is selective for the modified surfaces, and that pronounced crystal growth is observed on two different substrate types, each acid functionalized with different chemistries, provides strong evidence for the acid-mediated nucleation and growth of the PPF-5.

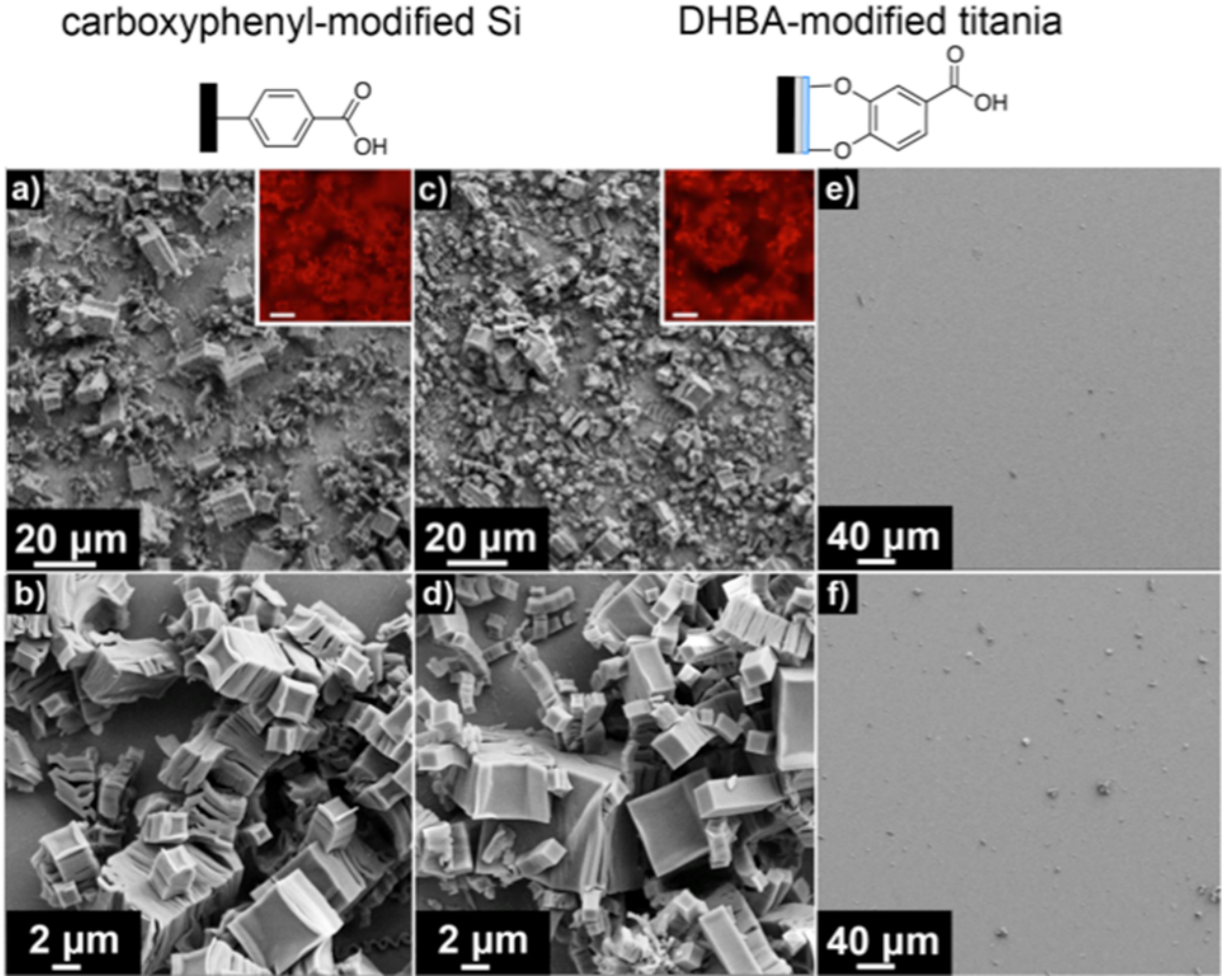

Figure 20. Scanning electron microscope images of PPF-5 crystals grown at 80°C for 24 hours onto carboxyphenyl-functionalized Si (a,b) and DHBA-modified TiO_2 (c,d); Control surfaces of unmodified Si (e) and unmodified titania (f) produced no PPF-5 growth. (Insets: Fluorescence images of PPF-5 crystals, λ_{Ex}: 510-550 nm; inset scale bars correspond to 10µm.) Above: molecular schematics of the acid functionalization chemistries employed.

Figure 21a presents grazing incidence x-ray diffraction (GIXRD) patterns for PPF-5 grown for 24 hours on carboxyphenyl-modified Si (blue) and DHBA-modified titania (red) compared to the pattern calculated for unoriented (i.e., random) PPF-5 (black). Figure 21b contains a schematic of the PPF-5 crystal structure, in which the c-axis is parallel to the vertical bipyridine pillars, while the a-b plane is defined by the horizontal porphyrin linking the bipyridine pillars. The patterns for PPF-5 grown on the carboxylic acid-modified substrates match well with the calculated XRD pattern for the tetragonal PPF-5,[124] verifying that heterogeneous nucleation and growth of PPF-5 is occurring during solvothermal synthesis. Careful examination of these diffraction patterns, however, reveals notable crystallographic orientation of the PPF-5. In the patterns taken of PPF-5 grown on DHBA-modified titania, and to a lesser degree for PPF-5 on carboxy-modified Si, there are strong (110) reflections and the (001), (111), (002), (003), (222), and (004) reflections appear significantly enhanced, relative to the calculated pattern shown in black. Interestingly, the (100), (101), and (210) reflections are not observed or are strongly suppressed on both samples substrates as well. These observations indicate preferential growth of the PPF-5 along the [001], [110], and [111] directions. The scanning electron micrographs in Figure 21c, 21d, and 21e show remarkable examples of PPF-5 nanostacks growing along these preferred [001], [111], and [110]/[111] directions, respectively. In interpreting these images, it is reasonably assumed that the crystal structure correlates with the morphology of the nanostacks, such that the porphyrin-containing a-b plane lies parallel to the plane of the sheets in the nanostacks. The lower magnification images in Figure 20 show a polycrystalline composite of nanostacks with these crystal orientations, though it should be noted that a portion of the relatively jumbled appearance of these crystals may be attributed to crystal stacks that have either broken and fallen or simply tilted over during drying (in preparation for the SEM). Flexibility of the largely organic sheets may also contribute to tilting or bending of the stacks, as well as the apparently loose packing of the sheets in the stacks (Figure 21c-21e).

In previous reports, other MOFs grown on carboxylate-rich SAM-coated surfaces have been shown to induce oriented crystal growth.[137, 139, 153] In previously reported cases, the demonstrated heterogeneous nucleation and growth of MOFs involves using surface-bound coordinating ligands to bind the metal cations of the MOF, forming a molecular seed layer capable of promoting subsequent MOF crystallization.[121] In the present system, we expect that surface-functionalized carboxylate binding concentrates Co^{2+} on the substrate surface, providing a metal-rich environment to seed the binding of the bipyridine pillars or porphyrins. We speculate that how the porphyrins, bipyridine molecules, and Co^{2+} ions cooperatively interact and bind to the acid-modified surfaces determines the crystallographic selectivity observed in this system. For example, porphyrins binding horizontally on an acidic surface enriched with Co^{2+} ions would be expected to promote preferential vertical crystal growth along the observed [001] direction. Alternatively, growth along directions such as the [100], a direction not observed in the diffraction in Figure 21a, would be selected against in this system, as this would require nucleation on the unlikely configuration of multiple bipyridines bound to the functionalized surface, oriented parallel to each other and separated exactly 1 unit cell apart. The exact mechanisms responsible for the observed preferential crystal growth are likely complex, and it is not the intention of this paper to discuss those mechanisms in detail. Still, it is apparent from the observations presented here that the acid functionalized surface not only promotes crystal nucleation, but also influences the crystallographic orientation of the nucleating PPF-5 crystal nanostacks.

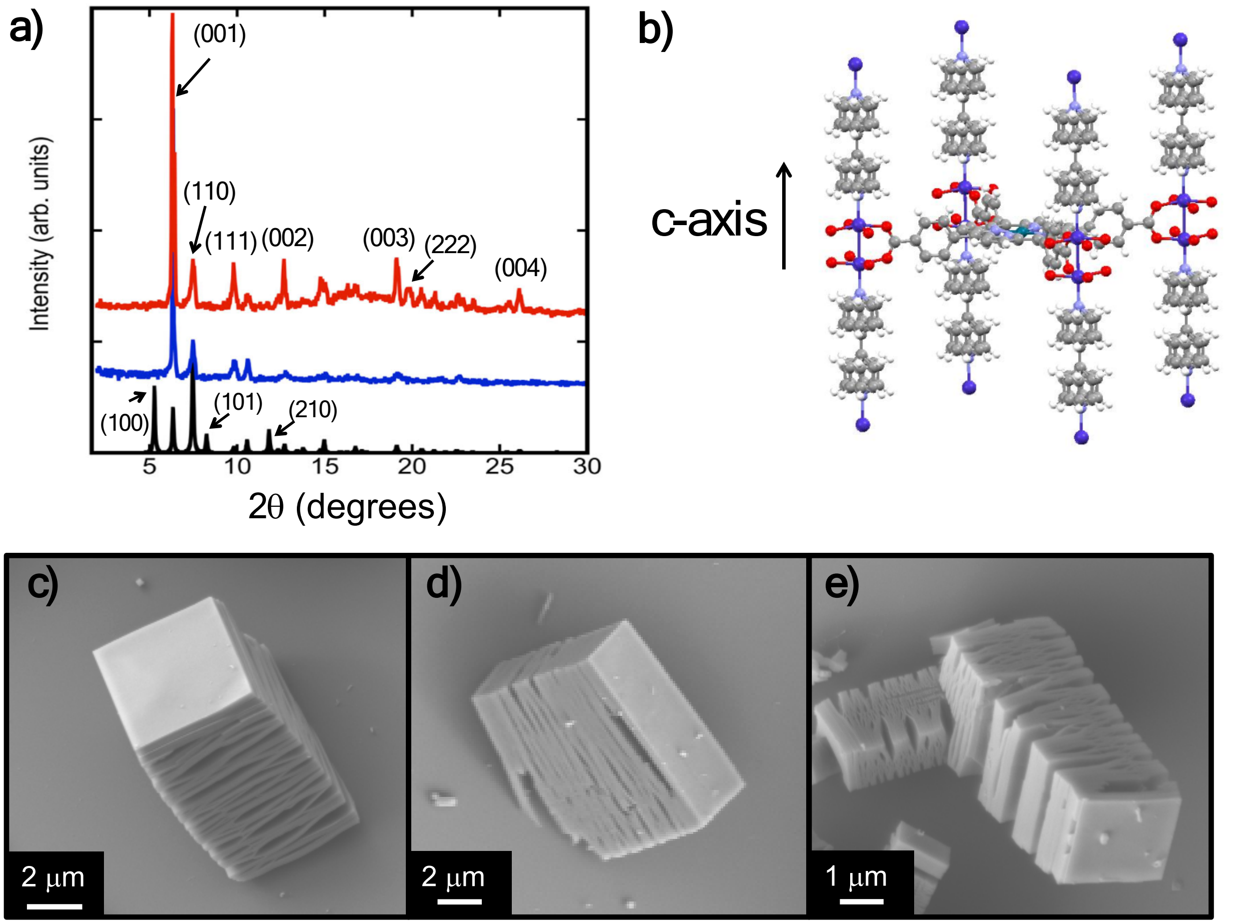

Figure 21. (a) Grazing incidence X-ray diffraction patterns for PPF-5 grown on carboxyphenyl-modified Si (blue) and DHBA-modified titania (red) shown with the calculated pattern for PPF-5 (black). Strong or enhanced reflections are labeled above, while peaks absent in the measured data are indicated on the calculated pattern below. (b) Schematic PPF-5 crystal structure and c-axis orientation. Dark blue spheres are cobalt, red spheres are oxygen, lavendar spheres are nitrogen, gray spheres are carbon, white spheres are hydrogen, and green sphere is palladium. (c-e) SEM image of PPF-5 crystals grown at 80°C on DHBA-modified titania, the vertical stack growing along the [001] direction (c), the [111] direction (d), and both the [110] and [111] directions (e).

Interestingly, when the PPF-5 growth temperature is increased to 100°C, the morphology of PPF-5 crystals changes. The SEM images in Figure 22 show structures typical of those seen on both carboxyphenyl-modified Si and DHBA-modified titania. These structures still form as stacks of PPF-5 sheets, but at the center of the structures, fine sheets pack together to create a dense, corrugated core. Extending from this core are more coarse, ribbon-like sheets packed much less densely together. Fluorescence imaging (Figure 22a inset) shows uniform fluorescence from the PPF-5 crystals, indicating that the Pd-containing metalloporphyrin is present throughout both low- and high-density regions of the crystals and GIXRD confirms that the PPF-5 grown at 100°C exhibits the same orientational preference displayed at 80°C. The synthetic mechanisms responsible for the dual morphology in these materials are not clear at this time, but we postulate that these structures may have formed in a two-stage growth process in which rapid initial crystal nucleation to form the dense core is followed by a steady-state growth phase that produces the more coarse, loosely packed sheets.

Controlling crystal size and nanoscale morphology are important to regulating the properties and functions of MOFs. In some instances, this control can be achieved by incorporating additives during crystal growth.[154-158] Alternatively, Stavila, et al.[153] recently showed that film morphology and roughness of HKUST-1 can be influenced by the composition of the substrate, with smoother films produced on silica substrates than on alumina. The present work indicates that surface-nucleated PPF-5 crystal morphology can be tuned simply by controlling growth temperature.

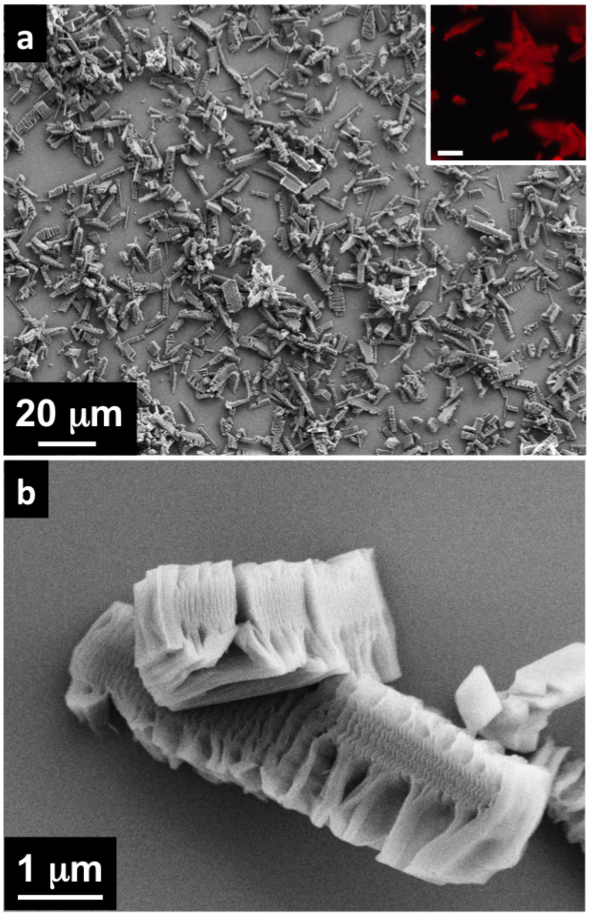

Figure 22. Scanning electron micrographs of PPF-5 grown for 24 hours at 100 °C on carboxyphenyl-modified Si. (Inset: Fluorescence image of PPF-5 crystals; inset scale bar correspond to 10μm.)

As an illustration of how the nanoscale morphology of these surface-nucleated MOFs may influence macroscopic properties, changes in the optical response of the photoactive PPF-5 structures were explored. Figure 23 illustrates how the photoluminescence (broad excitation between 510-550 nm) for PPF-5 crystals grown on carboxyphenyl-functionalized Si can be influenced by growth temperature and the associated morphology change. The black curve shows the photoluminesence of the Pd metalloporphyrin, the primary luminescent species in these MOFs. This spectrum shows a maximum emission at 622 nm and a shoulder just below 600 nm. When this porphyrin is incorporated into the crystalline environment of PPF-5, the shoulder disappears, and the maximum emission blue shifts. Crystals prepared at 80 °C show a blue shift of the maximum to 617 nm, while a further shift to 612 nm is observed for crystals grown at 100 °C. The molecular environment surrounding the porphyrins in the more densely-packed structures created at 100 °C appears to have further blue-shifted the photoluminescent emission. Although this is a relatively subtle change, it is nonetheless easily measured and is to our knowledge the first example of a microstructure-induced change in a MOF optical property.

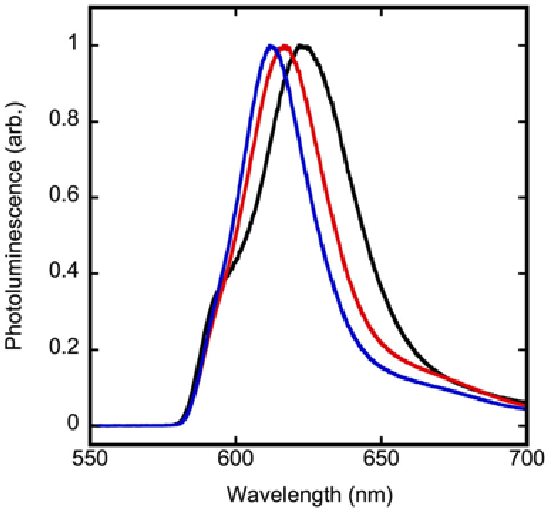

Figure 23. Fluorescence emission spectra for PPF-5 crystals grown on carboxyphenyl-functionalized Si substrates at 80 (red) and 100°C (blue) compared to Pd-TCPP (black).

5.4. Conclusions

The heterogeneous solvothermal crystal growth of pillared porphyrin framework 5 (PPF-5) was explored on Si and titania surfaces modified with widely applicable chemistries: p-carboxyphenyldiazonium tetrafluoroborate and 3,4-dihydroxybenzoic acid. Vertical PPF-5 stacks of rectangular sheets, showing preferential (001), (110) and (111) crystallographic orientation, grew selectively on acid-modified surfaces. Crystal size, morphology and density were nominally identical for both surface modification approaches. Furthermore, the morphology of PPF-5 crystals grown on these modified surfaces was demonstrated to be thermally tunable, as increasing crystal growth temperature influenced the morphology of the structures, producing PPF-5 stacks with a densely-packed core, connected to a loosely packed stack exterior. This change in morphology was correlated with a blue shift in photoluminescence, revealing tunable variation not only of structure, but also of properties. This demonstration of surface-induced growth of an optically active porphyrin paddlewheel framework on semiconducting surfaces may enable broader applicability of these functional materials in emerging optoelectronic systems.

Although the results discussed above demonstrate that solvothermal approaches can be successfully used to incorporate PPF-5 crystals into a solar energy conversion devices [159], the surface coverage and film morphology requires additional optimization. An attractive alternative to the solvothermal approach is to synthesize MOFs as supported thin films directly onto desired devices. Several methods have been developed, including *in situ* and *ex situ* approaches [3, 160]. One of the most versatile approaches used to date is the is the step-by-step liquid-phase approach that deposits alternating solutions of structural components onto functionalized substrates. The metal ions bind to the upper layers of ligands and *vice versa*, allowing the building of the 3D MOF structure. The film thickness is usually directly proportional to the number of immersion cycles and the resulting coatings are often ultrathin, oriented, and low surface roughness [161, 162]. The generality and simplicity of the method allow for its exploitation for the preparation of functional devices.

We investigated the step-by-step growth of films of porphyrin-based PPF-5 to form films of controlled thickness, orientation, and porosity. The synthesis of oriented PPF-5 films was achieved on functionalized alumina and ZnO surfaces. The oxide surfaces were cleaned and hydroxylated using oxygen plasma treatment. The film growth was monitored using a Quartz Crystal Microbalance (QCM) from SRS (model # SRS-200) operating at a fundamental resonance frequency of 5.0 MHz was used to monitor the frequency changes during the MOF growth. The QCM measurements were made in flow cells with one electrode in direct contact with the liquid phase. A schematic representation of the MOF growth setup is shown in Figure 24.

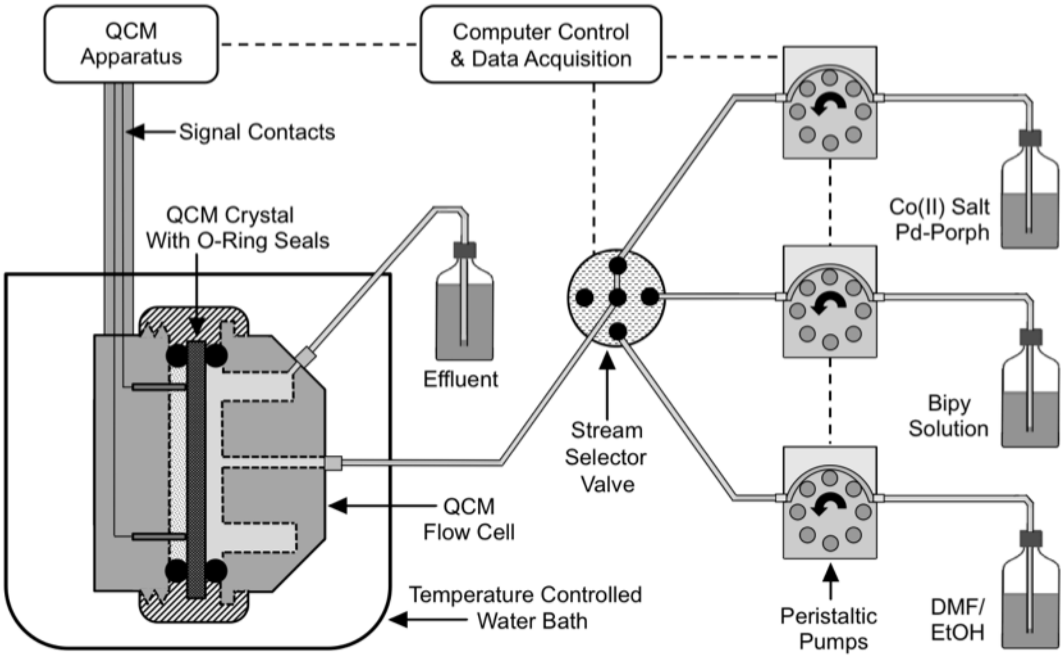

Figure 24. Schematic representation of the MOF fabrication setup coupled with a QCM apparatus to monitor the frequency changes during the step-by-step growth.

In a typical procedure, the QCM electrodes are initially saturated with a 0.5 M solution of cobalt(II) nitrate in 10:1 (vv) ethanol/dimethylformamide (DMF) at 30 °C. Next, a 0.2 M solution of palladium(II) meso-tetra(4-carboxyphenyl)porphine premixed in a 1:1 ratio with a 0.2 M solution of $Co(NO_3)_2$ was passed over the QCM crystal for 5 minutes. This step is followed by a surface wash step (10 min) with 1:10 DMF/EtOH. Finally, the QCM electrode was exposed to a 0.2 M solution of bipyridine in 1:10 DMF/EtOH for 5 min, followed by the surface wash for 10 min. The entire 30 min cycle was repeated from start for a total of 60 cycles and the frequency changes were monitored using the QCM apparatus (Figure 25). Subsequently flowing the metal, porphyrin and bipy pillar linker solutions over the QCM crystal results in a definite frequency change, which suggests certain species are deposited on the surface of the QCM electrode. A relatively simple relationship between the frequency change and mass uptake is given by the Sauerbrey equation, which correlates the observed frequency shifts to the deposited mass:

$$\Delta m = \frac{A\sqrt{\rho_q G_q}}{-2 f_0^2}\Delta f$$

where Δm is the change in mass, A is the surface area of the resonator, ρ_q and G_q are the density and shear modulus of the quartz, f_0 is the resonance frequency of the unloaded resonator and Δf is the change in resonance frequency. We previously reported that Sauerbrey equation is valid for HKUST-1 deposition on surfaces, as the energy dissipation of the deposited films is negligible [153]. The initial growth on both Al_2O_3 and ZnO surfaces is almost liner, however, after the initial 4-6 cycles, the rate of material deposition on the surface is slowed down.

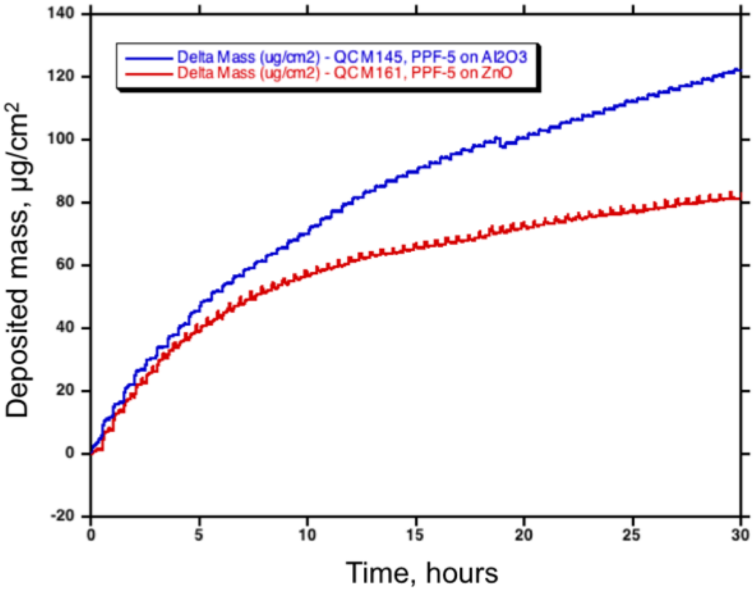

Figure 25. Step-by-step growth of PPF-5 on Al_2O_3 (QCM145, blue curve) and ZnO (QCM161, red curve) monitored by the QCM technique.

The morphology of the as-deposited films was investigated using scanning electron microscopy (SEM, Hitachi S-4500), while their identity was confirmed by the grazing incidence X-ray diffraction (GIXRD, Empyrean sytem). The GIXRD measurements were carried out using Cu *Kα* radiation (λ= 1.5418 Å) generated from an X-ray tube operated at 45 kV and 40 kA. The SEM image (Figure 26, left) of the as-deposited film reveals fairly uniform films, which seem to be composed of small intergrown particles. GIXRD measurements indicate that the PPF-5 film is highly oriented along the {001} direction of growth (Figure 26, right). The black curve indicates the experimental GIXRD pattern, while the blue and red curves indicate the calculated patterns mimicking the epitaxial growth along the {001} direction and polycrystalline PPF-5, respectively.

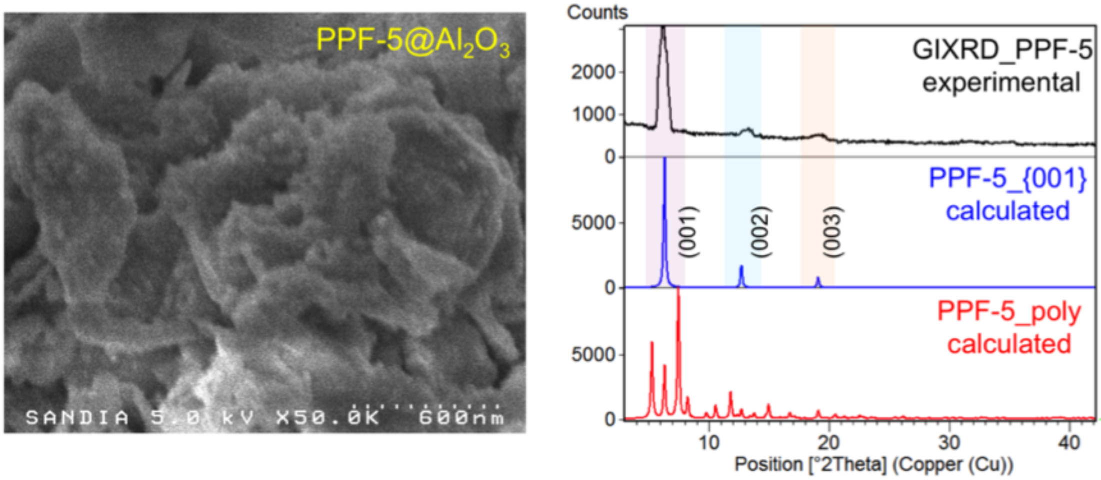

Figure 26. Step-by-step growth of PPF-5 on Al_2O_3 (QCM145, blue curve) and ZnO (QCM161, red curve) monitored by the QCM technique.

6. INTEGRATION OF METAL ORGANIC FRAMEWORKS FOR DYE-SENSITIZED SOLAR CELLS

The ability to grow MOF photoactive MOF architectures on titania surfaces as described in the previous chapter created an opportunity to exploit these materials in dye-sensitized solar cells.[163] (DSSCs). Figure 27 below schematically illustrates how a DSSC works. In a typical DSSC, a photoactive dye molecule is adsorbed onto a mesoporous layer of titania, which has been deposited or grown on a transparent conductive current collector, such as indium tin oxide (ITO) or fluorine-doped tin oxide (FTO). Opposite this dye-coated working electrode structure is a counter electrode, typically platinum or conductive carbon. Critically, separating these two electrodes is an electrically insulating organic liquid electrolyte containing a redox-active species, such as iodide-triiodide. As schematically shown in Figure 27 below, when the device is illuminated, the dye absorbs the light and transfers an electron to the TiO_2. The, now oxidized, dye is reduced by the redox active species. The oxidized redox species then effectively diffuses to the platinum counter electrode where it is catalytically regenerated through electron injection from, for example, the platinum. The cooperative transfer of charge between the counter-electrode, the redox-couple, the dye, the TiO_2 and the working electrode completes the electrical circuit needed to extract current from these cells.

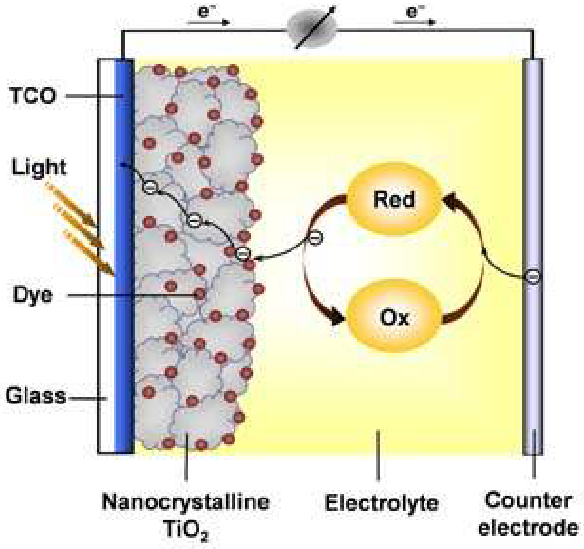

Figure 27. Schematic illustration of a typical DSSC. Image adapted from http://staff.bath.ac.uk/pysabw/abwmod.html

Based on this model, it was anticipated that a MOF, containing optically absorbing components, could be used as an active material in a DSSC, replacing or collaborating with traditional dye molecules. Figure 28 shows the optical absorbance for PPF-5 and a schematic depiction of how the highly ordered, porous structure of PPF-5 would be incorporated into a prototype device structure. The absorbance data indicate that the MOF is capable of significant visible light absorbance, important for terrestrial PV applications.

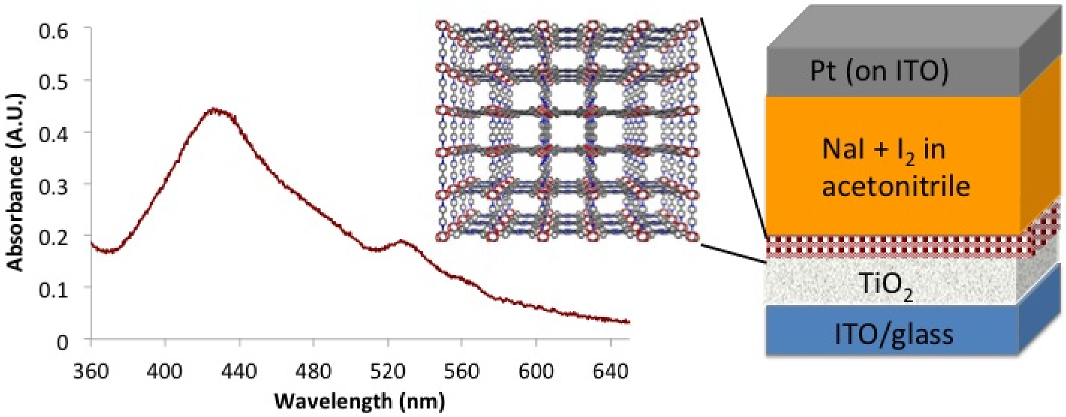

Figure 28. Optical absorbance of PPF-5 and illustration of MOF incorporation as an active layer in a DSSC architecture.

Using a MOF as an active material in a DSSC offers a number of potential advantages over more traditional dyes. Among the factors limiting the performance of these devices is the amount of dye that can be adsorbed onto the TiO_2. The more dye that can be incorporated into the device and still actively transport charge to the underlying TiO_2 working electrode, the more current can be generated by the device. Efforts to apply a high density of traditional dyes to these systems, however, suffer from dye aggregation, poor electrolyte access, and reduced charge transfer that all degrade device performance. Assembling the dye molecules in the organized framework of a MOF, however, could allow for introduction of increased dye density without dye aggregation. Properly engineered, the MOF could even be used to promote efficient energy or charge transfer through ordered molecular pathways to access charge generated in dye molecules not immediate adjacent to the TiO_2. Moreover, the open framework of the MOF would be expected to improve electrolyte (and redox mediator) access to the dye molecules and could provide space for complementary of supplementary absorbers. This latter concept could be used to expand the range of optical absorbance beyond what is possible with a single dye system. Other potential benefits of the MOF structure including possible improvements in dye stability, could be realized if MOFs were to be successfully integrated into DSSCs.

The absorbance shown in Figure 28 is substantially determined by the band gap (energy difference between the highest occupied molecular orbital (HOMO) and lowest unoccupied molecular orbital (LUMO)) of the dye. Just as important as the difference between the HOMO and LUMO levels of the dye, however, is the relative positions of these energy levels with respect to the various components shown in Figure 27. For example, the lowest unoccupied molecular orbital (LUMO) of the dye must be slightly higher than the conduction band of the TiO_2 to promote photo-excited electron transfer. At the same time, the highest occupied molecular orbital (HOMO) of the dye must lie slightly below the energy level of the redox mediator to allow for efficient regeneration of the dye. (Figure 29).

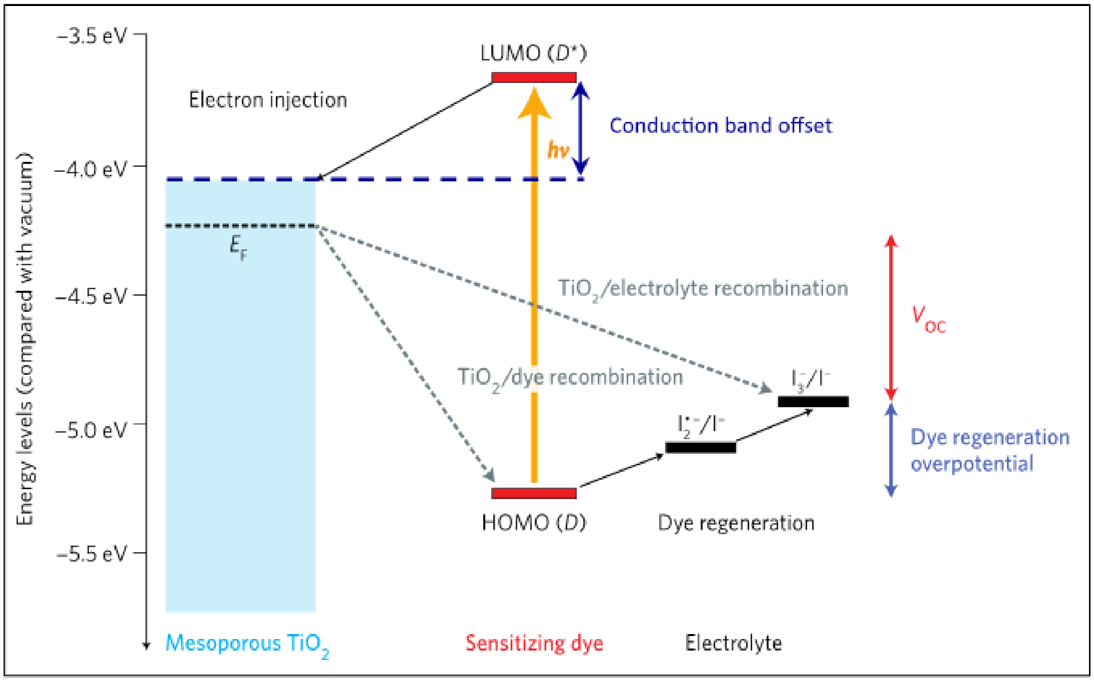

Figure 29. Schematic depiction of optoelectronic band structure of a DSSC using iodide-triiodide as a redox mediator. Image adapted from Hardin, *et al.*[164]

Using density function theory calculations, the approximate relative band alignments of the photoactive porphyrin linker used to make PPF-5 in the previous chapter were determined. An estimate of the relative positions of the porphyrin linker, the TiO_2, and the redox mediator are shown in Figure 30 below.

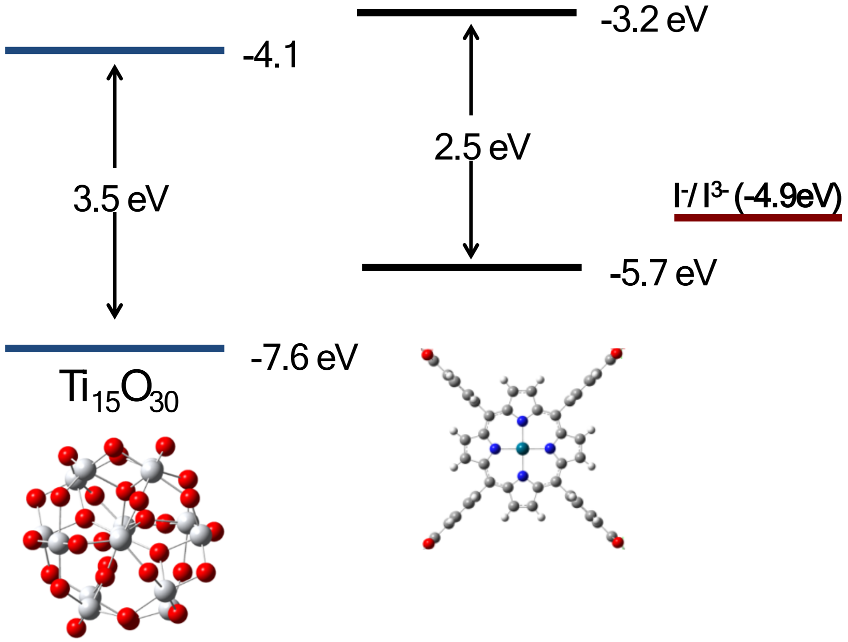

Figure 30. Relative band positions for a TiO_2 cluster, the porphyrin from PPF-5, and the I^-/I_3^- redox couple. Values for TiO_2 and the porphyrin linker determined using DFT (B3LYP/LanL2DZ) and DFT(B3LYP/ CEP-31G), respectively. Band energy values shown relative to vacuum.

Based on these predicted values, it was believed that PPF-5, containing this porphyrin linker, should be a viable candidate for use as a supramolecular dye construct in a prototype DSSC. Photoexcited electrons in the porphyrin would be expected to transfer to TiO_2, and the iodide-triiodide redox mediator should be capable of regenerating the porphoryin dye.

To evaluate the feasibility of such a system, prototype DSSC devices were constructed, using typical methods employed for DSSC construction.[165] For initial prototype devices, PPF-5 was grown on mesoporous TiO_2 using the solvothermal approach described in the previous chapter.[166] A slurry of TiO_2 (3.5g Degussa P25 TiO_2, 0.5mL titanium(IV) tetraisopropoxide in 15 mL ethanol)[167] was prepared and deposited either by doctor blading or spin-coating onto ITO substrates. Dried onto the TiO_2 substrates, an electrode area was defined by removing excess TiO_2. Substrates were annealed at 300°C for 10 minutes. Cooled to room temperature, these samples were then immersed in PPF-5 growth solution (9.2 mg Pd meso-tetra(carboxyphenyl) porphine, 8.8 mg $Co(NO_3)_2$ 6 H_2O, 2.8 mg 4,4'-bipyridine, 1.5 mL DEF, and 0.5 mL ethanol) and grown for 24 hours at 80°C. Samples were then washed with ethanol and slowly air-dried. Figure 31 shows an optical micrograph of a PPF-5 nanostack grown on the TiO_2 substrate.

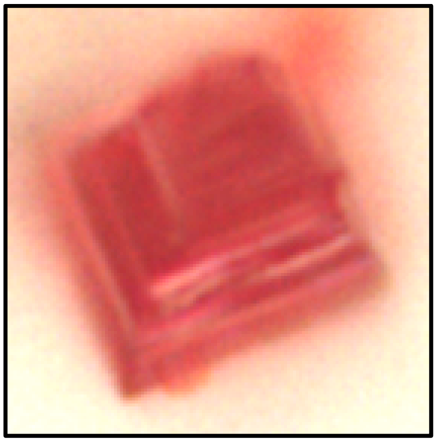

Figure 31. Optical micrograph of PPF-5 crystal nanostack grown on TiO_2. Red coloring due to light-absorbing porphyrin linker in PPF-5.

Double-sided adhesive tape was then applied around the edges of the TiO_2 active area, and an overlapping counter electrode was sealed over the tape, leaving a small gap for electrolyte injection between the working and counter electrodes. The counter electrodes consisted of a platinum coating (~80 nm thick) sputtered over an piece of ITO-coated glass. The electrolyte used consisted of 0.5 M LiI, 0.05 M I_2, and 0.5 M tert-butylpyridine in dissolved in acetonitrile. This electrolyte was injected to fill the inter-electrode space and a final piece of glass was used to cover the injection site.

Devices were then placed over a modified microscope stage where either white, green, blue, or UV light could be selectively and controllably used to excite the device using a mercury arc lamp. Electrical leads were connected to the ITO substrates used to form the counter and working electrodes. In both dark and illuminated conditions, these samples were then probed using cyclic voltammetry, monitoring the current response as a function of varied voltage. The device performance of these prototype samples, illuminated with white light (brightfield illumination) is shown in Figure 32 below.

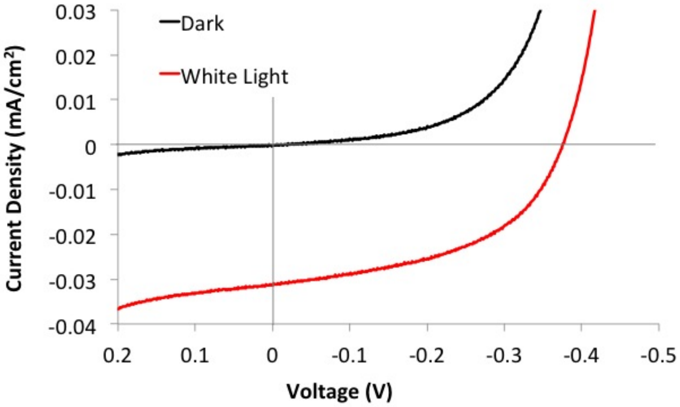

Figure 32. Current-voltage profiles for PPF-5 DSSC under dark and white light illumination.

The relatively rectangular shape of the current-voltage profiles is typical of a diode, such as one would expect in a photovoltaic cell. The data intercept with the x-axis yields the open circuit voltage, the intercept with the y-axis yields the short circuit current, and the effective "squareness" of the curve, determined by the ratio of maximum measured power to maximum theoretical power (Jsc x Voc), provided the fill factor (FF) of the device. Collectively, these three factors determine the efficiency of the device when normalized by the incident illumination power.

$$\eta = \frac{V_{OC} \times J_{SC} \times FF}{P_{in}}$$

From these data, it is apparent that this initial prototype device produced a Voc of 375mV, a fill factor of 0.48, and a Jsc of 0.031mA/cm^2. The plots in Figure 32 also include the current-voltage response for the device without illumination. Although the response is still consistent with diode behavior, there is no measurable Jsc or Voc. Similar control experiments with TiO_2 only showed negligible photocurrent generated (Jsc ~ 0.005 mA/cm^2), likely produced from the TiO_2 semiconductor in the working electrode.

With respect to the MOF-based device, although the Voc and the FF are respectable initial values, the relatively low value for the Jsc limits the efficiency of this device to considerably less than 1%. Nevertheless, this preliminary demonstration represents proof of principle for the application of this MOF-enabled device. Interestingly, when the illuminated light was filtered to promote high intensity illumination with green light (510-550nm) that corresponds strongly with the specific absorbance of the PPF-5 shown in Figure 28 above, the relevant metrics increased to a Voc of 442mV, a fill factor of 0.59, and a Jsc of 0.14mA/cm^2. By biasing the number of incident photons to the specific absorbance of the PPF-5, the photovoltaic performance increased considerably. This wavelength-selective result is of particular note because it confirms that the photocurrent generated is derived from the porphyrin species used to make the MOF. One area of important future work will be developing a characterization tool to distinguish between photocurrent generated by porphyrin contained within the MOF and porphyrin adsorbed independently to the TiO_2 surface.

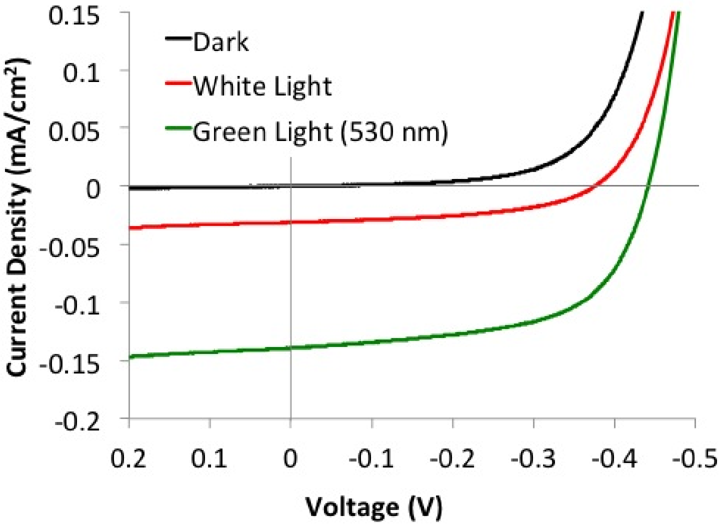

Figure 33. Current-voltage profiles for PPF-5 DSSC showing increase in PV performance under selective green light illumination.

7. REFERENCES

1. McGehee, M.D., *Nanostructured Organic-Inorganic Hybrid Solar Cells.* MRS Bull., 2009. **34**(2): p. 95-100.
2. Hardin, B.E., H.J. Snaith, and M.D. McGehee, *The renaissance of dye-sensitized solar cells.* Nature Photon., 2012. **6**(3): p. 162-169.
3. Allendorf, M.D., et al., *A Roadmap to Implementing Metal-Organic Frameworks in Electronic Devices: Challenges and Critical Directions.* Chem. Eur. J., 2011. **17**(41): p. 11372-11388.
4. Janssen, R.A.J. and J. Nelson, *Factors Limiting Device Efficiency in Organic Photovoltaics.* Adv. Mater., 2013. **25**(13): p. 1847-1858.
5. Liu, Y.-X., et al., *Resonance energy transfer from organic chromophores to fullerene molecules.* J. Appl. Phys. , 2006. **99**(9): p. 093521-4.
6. Ward, A.J., A. Ruseckas, and I.D.W. Samuel, *A Shift from Diffusion Assisted to Energy Transfer Controlled Fluorescence Quenching in Polymer-Fullerene Photovoltaic Blends.* J. Phys. Chem. C, 2012. **116**(45): p. 23931-23937.
7. Kirchartz, T., K. Taretto, and U. Rau, *Efficiency Limits of Organic Bulk Heterojunction Solar Cells.* J. Phys. Chem. C, 2009. **113**(41): p. 17958-17966.
8. Huynh, W.U., J.J. Dittmer, and A.P. Alivisatos, *Hybrid Nanorod-Polymer Solar Cells.* Science, 2002. **295**(5564): p. 2425-2427.
9. Shaheen, S.E., et al., *2.5% efficient organic plastic solar cells.* Appl. Phys. Lett., 2001. **78**(6): p. 841-843.
10. Wienk, M.M., et al., *Efficient Methano[70]fullerene/MDMO-PPV Bulk Heterojunction Photovoltaic Cells.* Angew. Chem. Int. Ed., 2003. **42**(29): p. 3371-3375.
11. Yi, Y., V. Coropceanu, and J.-L. Brédas, *Exciton-Dissociation and Charge-Recombination Processes in Pentacene/C60 Solar Cells: Theoretical Insight into the Impact of Interface Geometry.* J. Am. Chem. Soc., 2009. **131**(43): p. 15777-15783.
12. Peumans, P., S. Uchida, and S.R. Forrest, *Efficient bulk heterojunction photovoltaic cells using small-molecular-weight organic thin films.* Nature, 2003. **425**(6954): p. 158-162.
13. Schmidt-Mende, L., et al., *Self-Organized Discotic Liquid Crystals for High-Efficiency Organic Photovoltaics.* Science, 2001. **293**(5532): p. 1119-1122.
14. Thompson, B.C. and J.M.J. Fréchet, *Polymer–Fullerene Composite Solar Cells.* Angew. Chem. Int. Ed., 2008. **47**(1): p. 58-77.
15. Ferey, G., *Hybrid porous solids: past, present, future.* Chem. Soc. Rev., 2008. **37**(1): p. 191-214.
16. Li, H., et al., *Design and synthesis of an exceptionally stable and highly porous metal-organic framework.* Nature, 1999. **402**(6759): p. 276-279.
17. Murray, L.J., M. Dinca, and J.R. Long, *Hydrogen storage in metal-organic frameworks.* Chem. Soc. Rev., 2009. **38**(5): p. 1294-1314.
18. Banerjee, R., et al., *Control of Pore Size and Functionality in Isoreticular Zeolitic Imidazolate Frameworks and their Carbon Dioxide Selective Capture Properties.* J. Am. Chem. Soc., 2009. **131**(11): p. 3875-3877.
19. Cui, Y., et al., *Luminescent Functional Metal–Organic Frameworks.* Chem. Rev., 2011. **112**(2): p. 1126-1162.

20. Eddaoudi, M., et al., *Systematic Design of Pore Size and Functionality in Isoreticular MOFs and Their Application in Methane Storage.* Science, 2002. **295**(5554): p. 469-472.
21. Son, H.-J., et al., *Light-Harvesting and Ultrafast Energy Migration in Porphyrin-Based Metal–Organic Frameworks.* J. Am. Chem. Soc., 2012. **135**(2): p. 862-869.
22. Khajavi, H., et al., *Unraveling the Optoelectronic and Photochemical Behavior of Zn4O-Based Metal Organic Frameworks.* J. Phys. Chem. C, 2011. **115**(25): p. 12487-12493.
23. Yang, L.-M., et al., *Formation of an intermediate band in isoreticular metal-organic framework-993 (IRMOF-993) and metal-substituted analogues M-IRMOF-993.* J. Mater. Chem. , 2012. **22**(32): p. 16324-16335.
24. Fuentes-Cabrera, M., et al., *Electronic structure and properties of isoreticular metal-organic frameworks: The case of M-IRMOF1 (M = Zn, Cd, Be, Mg, and Ca).* J. Chem. Phys., 2005. **123**(12): p. 124713-5.
25. Gascon, J., et al., *Isoreticular MOFs as Efficient Photocatalysts with Tunable Band Gap: An Operando FTIR Study of the Photoinduced Oxidation of Propylene.* ChemSusChem, 2008. **1**(12): p. 981-983.
26. Allendorf, M.D., et al., *Luminescent metal-organic frameworks.* Chem. Soc. Rev., 2009. **38**(5): p. 1330-1352.
27. Kent, C.A., et al., *Amplified Luminescence Quenching of Phosphorescent Metal–Organic Frameworks.* J. Am. Chem. Soc., 2012. **134**(9): p. 3991-3994.
28. Kent, C.A., et al., *Energy Transfer Dynamics in Metal−Organic Frameworks.* J. Am. Chem. Soc., 2010. **132**(37): p. 12767-12769.
29. Wang, C. and W. Lin, *Diffusion-Controlled Luminescence Quenching in Metal−Organic Frameworks.* J. Am. Chem. Soc., 2011. **133**(12): p. 4232-4235.
30. Jin, S., et al., *Energy Transfer from Quantum Dots to Metal–Organic Frameworks for Enhanced Light Harvesting.* J. Am. Chem. Soc., 2013. **135**(3): p. 955-958.
31. Streit, H.C., et al., *Surface-Anchored MOF-Based Photonic Antennae.* Chemphyschem, 2012. **13**(11): p. 2699-2702.
32. Chae, H.K., et al., *A route to high surface area, porosity and inclusion of large molecules in crystals.* Nature, 2004. **427**(6974): p. 523-527.
33. Porezag, D., et al., *Construction of tight-binding-like potentials on the basis of density-functional theory: Application to carbon.* Physical Review B, 1995. **51**(19): p. 12947-12957.
34. Seifert, G., D. Porezag, and T. Frauenheim, *Calculations of molecules, clusters, and solids with a simplified LCAO-DFT-LDA scheme.* International Journal of Quantum Chemistry, 1996. **58**(2): p. 185-192.
35. Elstner, M., et al., *Self-consistent-charge density-functional tight-binding method for simulations of complex materials properties.* Physical Review B, 1998. **58**(11): p. 7260-7268.
36. Moreira, N.H., et al., *Toward an Accurate Density-Functional Tight-Binding Description of Zinc-Containing Compounds.* Journal of Chemical Theory and Computation, 2009. **5**(3): p. 605-614.
37. Aradi, B., B. Hourahine, and T. Frauenheim, *DFTB+, a sparse matrix-based implementation of the DFTB method.* J. Phys. Chem. A, 2007. **111**(26): p. 5678-5684.
38. Chai, J.-D. and M. Head-Gordon, *Long-range corrected hybrid density functionals with damped atom-atom dispersion corrections.* Physical Chemistry Chemical Physics, 2008. **10**(44): p. 6615-6620.

39. M. J. Frisch, G.W.T., H. B. Schlegel, G. E. Scuseria, M. A. Robb, J. R. Cheeseman, G. Scalmani, V. Barone, B. Mennucci, G. A. Petersson, H. Nakatsuji, M. Caricato, X. Li, H. P. Hratchian, A. F. Izmaylov, J. Bloino, G. Zheng, J. L. Sonnenberg, M. Hada, M. Ehara, K. Toyota, R. Fukuda, J. Hasegawa, M. Ishida, T. Nakajima, Y. Honda, O. Kitao, H. Nakai, T. Vreven, J. A. Montgomery, Jr., J. E. Peralta, F. Ogliaro, M. Bearpark, J. J. Heyd, E. Brothers, K. N. Kudin, V. N. Staroverov, R. Kobayashi, J. Normand, K. Raghavachari, A. Rendell, J. C. Burant, S. S. Iyengar, J. Tomasi, M. Cossi, N. Rega, J. M. Millam, M. Klene, J. E. Knox, J. B. Cross, V. Bakken, C. Adamo, J. Jaramillo, R. Gomperts, R. E. Stratmann, O. Yazyev, A. J. Austin, R. Cammi, C. Pomelli, J. W. Ochterski, R. L. Martin, K. Morokuma, V. G. Zakrzewski, G. A. Voth, P. Salvador, J. J. Dannenberg, S. Dapprich, A. D. Daniels, Ö. Farkas, J. B. Foresman, J. V. Ortiz, J. Cioslowski, D. J. Fox, *Gaussian 09, Revision C.01*. 2009, Gaussian, Inc.: Wallingford CT.
40. Millward, A.R. and O.M. Yaghi, *Metal−Organic Frameworks with Exceptionally High Capacity for Storage of Carbon Dioxide at Room Temperature.* J. Am. Chem. Soc., 2005. **127**(51): p. 17998-17999.
41. Perry Iv, J.J., et al., *Connecting structure with function in metal-organic frameworks to design novel photo- and radioluminescent materials.* J. Mater. Chem. , 2012. **22**(20): p. 10235-10248.
42. Bauer, C.A., et al., *Influence of Connectivity and Porosity on Ligand-Based Luminescence in Zinc Metal−Organic Frameworks.* J. Am. Chem. Soc., 2007. **129**(22): p. 7136-7144.
43. Cook, S., et al., *A photophysical study of PCBM thin films.* Chem. Phys. Lett., 2007. **445**(4–6): p. 276-280.
44. Lakowicz, J.R., *Principles of Fluorescence Spectroscopy, Third Edition.* J. Biomed. Optics, 2008. **13**(2): p. 029901-029901.
45. Yassar, A., et al., *Exciton Coupling Effects in the Absorption and Photoluminescence of Sexithiophene Derivatives.* J. Phys. Chem., 1995. **99**: p. 9155-9159.
46. Sun, M., *Control of structure and photophysical properties by protonation and subsequent intramolecular hydrogen bonding.* The Journal of Chemical Physics, 2006. **124**(5): p. 054903.
47. McCarthy, B.D., et al., *Charge Transfer or J-Coupling? Assignment of an Unexpected Red-Shifted Absorption Band in a Naphthalenediimide-Based Metal-Organic Framework.* J. Phys. Chem. Lett., 2013. **4**(3): p. 453-458.
48. Rowsell, J.L.C., et al., *Hydrogen Sorption in Functionalized Metal−Organic Frameworks.* Journal of the American Chemical Society, 2004. **126**(18): p. 5666-5667.
49. Millward, A.R. and O.M. Yaghi, *Metal−Organic Frameworks with Exceptionally High Capacity for Storage of Carbon Dioxide at Room Temperature.* Journal of the American Chemical Society, 2005. **127**(51): p. 17998-17999.
50. Wu, H., et al., *Metal–Organic Frameworks with Exceptionally High Methane Uptake: Where and How is Methane Stored?* Chemistry – A European Journal, 2010. **16**(17): p. 5205-5214.
51. Yang, Q., et al., *CH4 storage and CO2 capture in highly porous zirconium oxide based metal-organic frameworks.* Chemical Communications, 2012. **48**(79): p. 9831-9833.
52. Seo, J.S., et al., *A homochiral metal-organic porous material for enantioselective separation and catalysis.* Nature, 2000. **404**(6781): p. 982-986.

53. Li, J.-R., R.J. Kuppler, and H.-C. Zhou, *Selective gas adsorption and separation in metal-organic frameworks.* Chemical Society Reviews, 2009. **38**(5): p. 1477-1504.
54. Nijem, N., et al., *Tuning the Gate Opening Pressure of Metal–Organic Frameworks (MOFs) for the Selective Separation of Hydrocarbons.* Journal of the American Chemical Society, 2012. **134**(37): p. 15201-15204.
55. Shigematsu, A., T. Yamada, and H. Kitagawa, *Selective Separation of Water, Methanol, and Ethanol by a Porous Coordination Polymer Built with a Flexible Tetrahedral Ligand.* Journal of the American Chemical Society, 2012. **134**(32): p. 13145-13147.
56. Xie, S.-M., et al., *Chiral Metal–Organic Frameworks for High-Resolution Gas Chromatographic Separations.* Journal of the American Chemical Society, 2011. **133**(31): p. 11892-11895.
57. Kreno, L.E., et al., *Metal–Organic Framework Materials as Chemical Sensors.* Chemical Reviews, 2011. **112**(2): p. 1105-1125.
58. Allendorf, M.D., et al., *Stress-Induced Chemical Detection Using Flexible Metal−Organic Frameworks.* Journal of the American Chemical Society, 2008. **130**(44): p. 14404-14405.
59. Lan, A., et al., *A Luminescent Microporous Metal–Organic Framework for the Fast and Reversible Detection of High Explosives.* Angewandte Chemie International Edition, 2009. **48**(13): p. 2334-2338.
60. Farrusseng, D., S. Aguado, and C. Pinel, *Metal–Organic Frameworks: Opportunities for Catalysis.* Angewandte Chemie International Edition, 2009. **48**(41): p. 7502-7513.
61. Wu, C.-D. and W. Lin, *Heterogeneous Asymmetric Catalysis with Homochiral Metal–Organic Frameworks: Network-Structure-Dependent Catalytic Activity.* Angewandte Chemie International Edition, 2007. **46**(7): p. 1075-1078.
62. Vermoortele, F., et al., *Electronic Effects of Linker Substitution on Lewis Acid Catalysis with Metal–Organic Frameworks.* Angewandte Chemie International Edition, 2012. **51**(20): p. 4887-4890.
63. Lopez, H.A., et al., *Photochemical Response of Commercial MOFs: Al2(BDC)3 and Its Use As Active Material in Photovoltaic Devices.* The Journal of Physical Chemistry C, 2011. **115**(45): p. 22200-22206.
64. Son, H.-J., et al., *Light-Harvesting and Ultrafast Energy Migration in Porphyrin-Based Metal–Organic Frameworks.* Journal of the American Chemical Society, 2012. **135**(2): p. 862-869.
65. Narayan, T.C., et al., *High Charge Mobility in a Tetrathiafulvalene-Based Microporous Metal–Organic Framework.* Journal of the American Chemical Society, 2012. **134**(31): p. 12932-12935.
66. Sun, L., et al., *Mn2(2,5-disulfhydrylbenzene-1,4-dicarboxylate): A Microporous Metal–Organic Framework with Infinite (−Mn–S−)∞ Chains and High Intrinsic Charge Mobility.* Journal of the American Chemical Society, 2013. **135**(22): p. 8185-8188.
67. Lee, D.Y., et al., *Cu-Based Metal–Organic Frameworks for Photovoltaic Application.* The Journal of Physical Chemistry C, 2013.
68. Talin, A.A., et al., *Tunable Electrical Conductivity in Metal-Organic Framework Thin-Film Devices.* Science, 2014. **343**(6166): p. 66-69.
69. Leong, K., et al., *Energy and Charge Transfer by Donor-Acceptors Pairs Confined in a Metal-Organic Framework: A Spectroscopic and Computational Investigation.* J. Mater. Chem. A, 2014: p. DOI:10.1039/C3TA14328G.

70. Lunt, R.R., J.B. Benziger, and S.R. Forrest, *Relationship between Crystalline Order and Exciton Diffusion Length in Molecular Organic Semiconductors.* Advanced Materials, 2010. **22**(11): p. 1233-1236.
71. Clarke, T.M. and J.R. Durrant, *Charge Photogeneration in Organic Solar Cells.* Chemical Reviews, 2010. **110**(11): p. 6736-6767.
72. Janssen, R.A.J. and J. Nelson, *Factors Limiting Device Efficiency in Organic Photovoltaics.* Advanced Materials, 2013. **25**(13): p. 1847-1858.
73. Thompson, B.C. and J.M.J. Fréchet, *Polymer–Fullerene Composite Solar Cells.* Angewandte Chemie International Edition, 2008. **47**(1): p. 58-77.
74. Hendon, C.H., D. Tiana, and A. Walsh, *Conductive metal-organic frameworks and networks: fact or fantasy?* Physical Chemistry Chemical Physics, 2012. **14**(38): p. 13120-13132.
75. D'Alessandro, D.M., J.R.R. Kanga, and J.S. Caddy, *Towards Conducting Metal-Organic Frameworks.* Australian J. Chem., 2011. **64**(6): p. 718-722.
76. Kobayashi, Y., et al., *Conductivity, Doping, and Redox Chemistry of a Microporous Dithiolene-Based Metal−Organic Framework.* Chemistry of Materials, 2010. **22**(14): p. 4120-4122.
77. Rosi, N.L., et al., *Rod Packings and Metal−Organic Frameworks Constructed from Rod-Shaped Secondary Building Units.* Journal of the American Chemical Society, 2005. **127**(5): p. 1504-1518.
78. McDonald, T.M., et al., *Capture of Carbon Dioxide from Air and Flue Gas in the Alkylamine-Appended Metal–Organic Framework mmen-Mg2(dobpdc).* Journal of the American Chemical Society, 2012. **134**(16): p. 7056-7065.
79. Dietzel, P.D.C., R. Blom, and H. Fjellvåg, *Base-Induced Formation of Two Magnesium Metal-Organic Framework Compounds with a Bifunctional Tetratopic Ligand.* European Journal of Inorganic Chemistry, 2008. **2008**(23): p. 3624-3632.
80. Yaghi, O.M., et al., *Reticular synthesis and the design of new materials.* Nature, 2003. **423**(6941): p. 705-714.
81. Deng, H., et al., *Large-Pore Apertures in a Series of Metal-Organic Frameworks.* Science, 2012. **336**(6084): p. 1018-1023.
82. Dietzel, P.D.C., et al., *An In Situ High-Temperature Single-Crystal Investigation of a Dehydrated Metal–Organic Framework Compound and Field-Induced Magnetization of One-Dimensional Metal–Oxygen Chains.* Angewandte Chemie International Edition, 2005. **44**(39): p. 6354-6358.
83. Foster, M.E. and B.M. Wong, *Nonempirically Tuned Range-Separated DFT Accurately Predicts Both Fundamental and Excitation Gaps in DNA and RNA Nucleobases.* Journal of Chemical Theory and Computation, 2012. **8**(8): p. 2682-2687.
84. Kronik, L., et al., *Excitation Gaps of Finite-Sized Systems from Optimally Tuned Range-Separated Hybrid Functionals.* Journal of Chemical Theory and Computation, 2012. **8**(5): p. 1515-1531.
85. Refaely-Abramson, S., R. Baer, and L. Kronik, *Fundamental and excitation gaps in molecules of relevance for organic photovoltaics from an optimally tuned range-separated hybrid functional.* Physical Review B, 2011. **84**(7): p. 075144.
86. Stein, T., L. Kronik, and R. Baer, *Reliable Prediction of Charge Transfer Excitations in Molecular Complexes Using Time-Dependent Density Functional Theory.* Journal of the American Chemical Society, 2009. **131**(8): p. 2818-2820.

87. Iikura, H., et al., *A long-range correction scheme for generalized-gradient-approximation exchange functionals.* The Journal of Chemical Physics, 2001. **115**(8): p. 3540-3544.
88. Stein, T., L. Kronik, and R. Baer, *Prediction of charge-transfer excitations in coumarin-based dyes using a range-separated functional tuned from first principles.* The Journal of Chemical Physics, 2009. **131**(24): p. 244119.
89. Wong, B.M., M. Piacenza, and F. Della Sala, *Absorption and fluorescence properties of oligothiophene biomarkers from long-range-corrected time-dependent density functional theory.* Physical Chemistry Chemical Physics, 2009. **11**(22): p. 4498-4508.
90. Baer, R., E. Livshits, and U. Salzner, *Tuned Range-Separated Hybrids in Density Functional Theory.* Annual Review of Physical Chemistry, 2010. **61**(1): p. 85-109.
91. Tawada, Y., et al., *A long-range-corrected time-dependent density functional theory.* Journal of Chemical Physics, 2004. **120**(18): p. 8425-8433.
92. Janak, J.F., *Proof that ∂E/∂n_{i}=ε in density-functional theory.* Physical Review B, 1978. **18**(12): p. 7165-7168.
93. García, G., et al., *A Tuned LRC-DFT Design of Ambipolar Diketopyrrolopyrrole-Containing Quinoidal Molecules Interesting for Molecular Electronics.* Journal of Chemical Theory and Computation, 2013. **9**(6): p. 2591-2601.
94. M. J. Frisch, G.W.T., H. B. Schlegel, G. E. Scuseria, M. A. Robb, J. R. Cheeseman, G. Scalmani, V. Barone, B. Mennucci, G. A. Petersson, H. Nakatsuji, M. Caricato, X. Li, H. P. Hratchian, A. F. Izmaylov, J. Bloino, G. Zheng, J. L. Sonnenberg, M. Hada, M. Ehara, K. Toyota, R. Fukuda, J. Hasegawa, M. Ishida, T. Nakajima, Y. Honda, O. Kitao, H. Nakai, T. Vreven, J. A. Montgomery, Jr., J. E. Peralta, F. Ogliaro, M. Bearpark, J. J. Heyd, E. Brothers, K. N. Kudin, V. N. Staroverov, R. Kobayashi, J. Normand, K. Raghavachari, A. Rendell, J. C. Burant, S. S. Iyengar, J. Tomasi, M. Cossi, N. Rega, J. M. Millam, M. Klene, J. E. Knox, J. B. Cross, V. Bakken, C. Adamo, J. Jaramillo, R. Gomperts, R. E. Stratmann, O. Yazyev, A. J. Austin, R. Cammi, C. Pomelli, J. W. Ochterski, R. L. Martin, K. Morokuma, V. G. Zakrzewski, G. A. Voth, P. Salvador, J. J. Dannenberg, S. Dapprich, A. D. Daniels, Ö. Farkas, J. B. Foresman, J. V. Ortiz, J. Cioslowski, D. J. Fox, *GAUSSIAN 09 (Revision D.01)*. 2009, *GAUSSIAN 09 (Revision D.01)*, Gaussian, Inc.: Wallingford CT.
95. Grimme, S., *Semiempirical GGA-type density functional constructed with a long-range dispersion correction.* Journal of Computational Chemistry, 2006. **27**(15): p. 1787-1799.
96. Kresse, G. and J. Hafner, *Ab initio molecular dynamics for liquid metals.* Phys. Rev. B, 1993. **47**(1): p. 558-561.
97. Kresse, G. and J. Hafner, *Ab initio molecular-dynamics simulation of the liquid-metal–amorphous-semiconductor transition in germanium.* Phys. Rev. B, 1994. **49**(20): p. 14251-14269.
98. Kresse, G. and J. Furthmüller, *Efficiency of ab-initio total energy calculations for metals and semiconductors using a plane-wave basis set.* Comp. Mater. Sci., 1996. **6**(1): p. 15-50.
99. Kresse, G. and J. Furthmüller, *Efficient iterative schemes for ab initio total-energy calculations using a plane-wave basis set.* Phys. Rev. B, 1996. **54**(16): p. 11169-11186.
100. Perdew, J.P., K. Burke, and Y. Wang, *Generalized gradient approximation for the exchange-correlation hole of a many-electron system.* Physical Review B, 1996. **54**(23): p. 16533-16539.

101. Blöchl, P.E., *Projector augmented-wave method.* Phys. Rev. B, 1994. **50**(24): p. 17953-17979.
102. Kresse, G. and D. Joubert, *From ultrasoft pseudopotentials to the projector augmented-wave method.* Phys. Rev. B, 1999. **59**(3): p. 1758-1775.
103. Monkhorst, H.J. and J.D. Pack, *Special points for Brillouin-zone integrations.* Physical Review B, 1976. **13**(12): p. 5188-5192.
104. Blöchl, P.E., O. Jepsen, and O.K. Andersen, *Improved tetrahedron method for Brillouin-zone integrations.* Physical Review B, 1994. **49**(23): p. 16223-16233.
105. Krukau, A.V., et al., *Influence of the exchange screening parameter on the performance of screened hybrid functionals.* The Journal of Chemical Physics, 2006. **125**(22): p. 224106.
106. Heyd, J., G.E. Scuseria, and M. Ernzerhof, *Hybrid functionals based on a screened Coulomb potential.* The Journal of Chemical Physics, 2003. **118**(18): p. 8207-8215.
107. Muntwiler, M. and X. Zhu, *Exciton Formation and Decay at Surfaces and Interfaces*, in *Dynamics at Solid State Surfaces and Interfaces: Volume 1 - Current Developments*, U. Bovensiepen, H. Petek, and M. Wolf, Editors. 2010, Wiley.
108. Li, Y., et al., *High mobility diketopyrrolopyrrole (DPP)-based organic semiconductor materials for organic thin film transistors and photovoltaics.* Energy & Environmental Science, 2013. **6**(6): p. 1684-1710.
109. Dennler, G., M.C. Scharber, and C.J. Brabec, *Polymer-Fullerene Bulk-Heterojunction Solar Cells.* Advanced Materials, 2009. **21**(13): p. 1323-1338.
110. Bundgaard, E. and F.C. Krebs, *Low-Band-Gap Conjugated Polymers Based on Thiophene, Benzothiadiazole, and Benzobis(thiadiazole).* Macromolecules, 2006. **39**(8): p. 2823-2831.
111. Lim, Z.B., et al., *New moderate bandgap polymers containing alkoxysubstituted-benzo[c][1,2,5]thiadiazole and thiophene-based units.* Journal of Polymer Science Part A: Polymer Chemistry, 2011. **49**(20): p. 4387-4397.
112. Xiang, Z., et al., *Multiscale simulation and modelling of adsorptive processes for energy gas storage and carbon dioxide capture in porous coordination frameworks.* Energy & Environmental Science, 2010. **3**(10): p. 1469-1487.
113. Usov, P.M., C. Fabian, and D.M. D'Alessandro, *Rapid determination of the optical and redox properties of a metal-organic framework via in situ solid state spectroelectrochemistry.* Chemical Communications, 2012. **48**(33): p. 3945-3947.
114. McCarthy, B.D., et al., *Charge Transfer or J-Coupling? Assignment of an Unexpected Red-Shifted Absorption Band in a Naphthalenediimide-Based Metal–Organic Framework.* The Journal of Physical Chemistry Letters, 2013. **4**(3): p. 453-458.
115. Kung, C.-W., et al., *Metal–Organic Framework Thin Films Composed of Free-Standing Acicular Nanorods Exhibiting Reversible Electrochromism.* Chemistry of Materials, 2013. **25**(24): p. 5012-5017.
116. Wade, C.R., M. Li, and M. Dincă, *Facile Deposition of Multicolored Electrochromic Metal–Organic Framework Thin Films.* Angewandte Chemie International Edition, 2013. **52**(50): p. 13377-13381.
117. Butler, K.T., C.H. Hendon, and A. Walsh, *Electronic Chemical Potentials of Porous Metal–Organic Frameworks.* Journal of the American Chemical Society, 2014. **136**(7): p. 2703-2706.

118. Rodovsky, D.B., et al., *Quantifying the Relationship between the Maximum Achievable Voltage and Current Levels in Low-Bandgap Polymer Photovoltaics.* The Journal of Physical Chemistry C, 2013.
119. Sumida, K., et al., *Carbon Dioxide Capture in Metal-Organic Frameworks.* Chem. Rev. , 2012. **112**(2): p. 724-781.
120. Kreno, L.E., et al., *Metal-Organic Framework Materials as Chemical Sensors.* Chem. Rev., 2012. **112**(2): p. 1105-1125.
121. Shekhah, O., et al., *MOF thin films: existing and future applications.* Chem. Soc. Rev. , 2011. **40**(2): p. 1081-1106.
122. Lee, J., et al., *Metal-organic framework materials as catalysts.* Chem. Soc. Rev., 2009. **38**(5): p. 1450-1459.
123. Allendorf, M.D., et al., *A Roadmap to Implementing Metal-Organic Frameworks in Electronic Devices: Challenges and Critical Directions.* Chem.-Eur. J., 2011. **17**(41): p. 11372-11388.
124. Choi, E.Y., et al., *Pillared Porphyrin Homologous Series: Intergrowth in Metal-Organic Frameworks.* Inorg. Chem. , 2009. **48**(2): p. 426-428.
125. Makiura, R. and H. Kitagawa, *Porous Porphyrin Nanoarchitectures on Surfaces.* Eur. J. Inorg. Chem. , 2010(24): p. 3715-3724.
126. Abrahams, B.F., et al., *Assembly of Porphyrin Building-Blocks into Network Structures with Large Channels.* Nature, 1994. **369**(6483): p. 727-729.
127. Goldberg, I., *Crystal engineering of porphyrin framework solids.* Chem. Comm. , 2005(10): p. 1243-1254.
128. Farha, O.K., et al., *Active-Site-Accessible, Porphyrinic Metal-Organic Framework Materials.* J. Am. Chem. Soc. , 2011. **133**(15): p. 5652-5655.
129. Wang, X.S., et al., *Three-Dimensional Porous Metal-Metalloporphyrin Framework Consisting of Nanoscopic Polyhedral Cages.* J. Am. Chem. Soc. , 2011. **133**(41): p. 16322-16325.
130. Kosal, M.E., et al., *A functional zeolite analogue assembled from metalloporphyrins.* Nat. Mater. , 2002. **1**(2): p. 118-121.
131. Shultz, A.M., et al., *A Catalytically Active, Permanently Microporous MOF with Metalloporphyrin Struts.* J. Am. Chem. Soc. , 2009. **131**(12): p. 4204-+.
132. Son, H.J., et al., *Light-Harvesting and Ultrafast Energy Migration in Porphyrin-Based Metal-Organic Frameworks.* J. Am. Chem. Soc. , 2013. **135**(2): p. 862-869.
133. Matsunaga, S., N. Endo, and W. Mori, *A New Metal Carboxylate Framework Based on Porphyrin with Extended pi-Conjugation.* Eur. J. Inorg. Chem. , 2011(29): p. 4550-4557.
134. Betard, A. and R.A. Fischer, *Metal-Organic Framework Thin Films: From Fundamentals to Applications.* Chem. Rev., 2012. **112**(2): p. 1055-1083.
135. Motoyama, S., et al., *Highly Crystalline Nanofilm by Layering of Porphyrin Metal-Organic Framework Sheets.* J. Am. Chem. Soc. , 2011. **133**(15): p. 5640-5643.
136. Shekhah, O., et al., *Controlling interpenetration in metal-organic frameworks by liquid-phase epitaxy.* Nat. Mater. , 2009. **8**(6): p. 481-484.
137. Shekhah, O., et al., *Step-by-step route for the synthesis of metal-organic frameworks.* J. Am. Chem. Soc. , 2007. **129**(49): p. 15118-+.
138. Zacher, D., et al., *Surface Chemistry of Metal-Organic Frameworks at the Liquid-Solid Interface.* Angew. Chem., Int. Ed. , 2011. **50**(1): p. 176-199.

139. Biemmi, E., C. Scherb, and T. Bein, *Oriented growth of the metal organic framework Cu-3(BTC)(2)(H2O)(3)center dot xH(2)O tunable with functionalized self-assembled monolayers.* J. Am. Chem. Soc. , 2007. **129**(26): p. 8054-+.
140. Zhuang, J.-L., et al., *Rapid Room-Temperature Synthesis of Metal–Organic Framework HKUST-1 Crystals in Bulk and as Oriented and Patterned Thin Films.* Adv. Funct. Mater., 2011. **21**(8): p. 1442-1447.
141. Hermes, S., et al., *Selective nucleation and growth of metal-organic open framework thin films on patterned COOH/CF3-terminated self-assembled monolayers on Au(111).* J. Am. Chem. Soc. , 2005. **127**(40): p. 13744-13745.
142. Hinterholzinger, F., et al., *Oriented growth of the functionalized metal-organic framework CAU-1 on -OH- and -COOH-terminated self-assembled monolayers.* Phys. Chem. Chem. Phys., 2010. **12**(17): p. 4515-4520.
143. Scherb, C., A. Schodel, and T. Bein, *Directing the structure of metal-organic frameworks by oriented surface growth on an organic monolayer.* Ang. Chem., Int. Ed. , 2008. **47**(31): p. 5777-5779.
144. Stewart, M.P., et al., *Direct covalent grafting of conjugated molecules onto Si, GaAs, and Pd surfaces from aryidiazonium salts.* J. Am. Chem. Soc. , 2004. **126**(1): p. 370-378.
145. Dalsin, J.L., et al., *Mussel adhesive protein mimetic polymers for the preparation of nonfouling surfaces.* J. Am. Chem. Soc. , 2003. **125**(14): p. 4253-4258.
146. deVilleneuve, C.H., et al., *Electrochemical formation of close-packed phenyl layers on Si(111).* J. Phys. Chem. B. , 1997. **101**(14): p. 2415-2420.
147. Rice, C.R., et al., *Catechol as an efficient anchoring group for attachment of ruthenium-polypyridine photosensitisers to solar cells based on nanocrystalline* TiO_2 *films.* New J. Chem., 2000. **24**(9): p. 651-652.
148. Rodriguez, R., M.A. Blesa, and A.E. Regazzoni, *Surface complexation at the* TiO_2 *(anatase) aqueous solution interface: Chemisorption of catechol.* J. Colloid Interface Sci. , 1996. **177**(1): p. 122-131.
149. Ting, G.G., et al., *Study on the Formation of Self-Assembled Monolayers on Sol-Gel Processed Hafnium Oxide as Dielectric Layers.* Langmuir, 2009. **25**(4): p. 2140-2147.
150. Han, S., et al., *Adsorption Characteristics of Anthraquinone-2-carboxylic Acid on Gold.* J. Phys. Chem. B., 2000. **104**: p. 11987-11995.
151. Schnadt, J., et al., *Structural study of adsorption of isonicotinic acid and related molecules on rutile TiO2 (110) II: XPS.* Surf. Sci., 2003. **544**: p. 74-86.
152. Wells, M., et al., *Interactions between Organized, Surface-Confined Monolayers and Vapor-Phase Probe Molecules. 9. Structure/Reactivity Relationship between Three Surface-Confined Isomers of Mercaptobenzoic Acid and Vapor-Phase Decylamine.* Langmuir, 1996. **12**: p. 1989-1996.
153. Stavila, V., et al., *Kinetics and mechanism of metal-organic framework thin film growth: systematic investigation of HKUST-1 deposition on QCM electrodes.* Chem. Sci., 2012. **3**(5): p. 1531-1540.
154. Li, Y.S., et al., *Controllable Synthesis of Metal-Organic Frameworks: From MOF Nanorods to Oriented MOF Membranes.* Adv. Mater., 2010. **22**(30): p. 3322-+.
155. Pham, M.H., et al., *Rational Synthesis of Metal-Organic Framework Nanocubes and Nanosheets Using Selective Modulators and Their Morphology-Dependent Gas-Sorption Properties.* Cryst. Growth Des. , 2012. **12**(6): p. 3091-3095.

156. Umemura, A., et al., *Morphology Design of Porous Coordination Polymer Crystals by Coordination Modulation.* J. Am. Chem. Soc. , 2011. **133**(39): p. 15506-15513.
157. Pham, M.H., et al., *Novel Route to Size-Controlled Fe-MIL-88B-NH2 Metal-Organic Framework Nanocrystals.* Langmuir, 2011. **27**(24): p. 15261-15267.
158. McCarthy, M.C., et al., *Synthesis of Zeolitic Imidazolate Framework Films and Membranes with Controlled Microstructures.* Langmuir, 2010. **26**(18): p. 14636-14641.
159. Van Gough, D., et al., *Controlled Nucleation and Growth of Pillared Paddlewheel Framework Nanostacks onto Chemically Modified Surfaces.* Acs Applied Materials & Interfaces, 2014. **6**(3): p. 1509-1514.
160. Stavila, V., A.A. Talin, and M.D. Allendorf, *MOF-based electronic and opto-electronic devices.* Chemical Society reviews, 2014. **43**(16): p. 5994-6010.
161. Bétard, A. and R.A. Fischer, *Metal–Organic Framework Thin Films: From Fundamentals to Applications.* Chem. Rev., 2012. **112**(2): p. 1055-1083.
162. Zacher, D., et al., *Thin films of metal-organic frameworks.* Chem. Soc. Rev., 2009. **38**(5): p. 1418-1429.
163. O'Regan, B. and M. Graetzel, *A Low-Cost, High Efficiency Solar Cell Based on Dye-Sensitized Colloidal TiO2 Films.* Nature, 1991. **353**: p. 737-740.
164. Hardin, B., H. Snaith, and M. McGehee, *The renaissance of dye-sensitized solar cells.* Nat. Photon. , 2012. **6**: p. 162-169.
165. Martineau, D., *Dye Solar Cells For Real: The Assembly Guide for Making Your Own Solar Cells*. 2012, Solaronix SA: Aubonne, Switzerland.
166. Gough, D., et al., *Controlled nucleation and growth of pillared paddlewheel framework nanostacks onto chemically modified surfaces.* ACS Appl. Mater. Inter., 2014. **6**(3): p. 1509-1514.
167. Zhang, D., et al., *Room-temperature synthesis of porous nanoparticular TiO2 films for flexible dye-sensitized solar cells.* Adv. Funct. Mater., 2006. **16**: p. 1228-1234.
168. Biradha, K., Y. Hongo, and M. Fujita, *Open Square-Grid Coordination Polymers of the Dimensions 20×20Å: Remarkably Stable and Crystalline Solids Even after Guest Removal.* Angewandte Chemie International Edition, 2000. **39**(21): p. 3843-3845.
169. Karagiaridi, O., et al., *Opening Metal–Organic Frameworks Vol. 2: Inserting Longer Pillars into Pillared-Paddlewheel Structures through Solvent-Assisted Linker Exchange.* Chemistry of Materials, 2013. **25**(17): p. 3499-3503.
170. Chung, H., et al., *Structural Variation in Porphyrin Pillared Homologous Series: Influence of Distinct Coordination Centers for Pillars on Framework Topology.* Crystal Growth & Design, 2009. **9**(7): p. 3327-3332.
171. Griggino, K.P., et al., *Modulating Electron Transfer in a Simple Bichromophoric System Employing Axial-Ligation as an Organizing Precept.* Journal of Inclusion Phenomena and Macrocyclic Chemistry, 2004. **49**(1-2): p. 27-32.
172. Röger, C. and F. Würthner, *Core-Tetrasubstituted Naphthalene Diimides:□ Synthesis, Optical Properties, and Redox Characteristics.* The Journal of Organic Chemistry, 2007. **72**(21): p. 8070-8075.
173. Krüger, H., et al., *Hybrid Supramolecular Naphthalene Diimide-thiophene Structures and their Application in Polymer Electronics.* Advanced Functional Materials, 2007. **17**(18): p. 3715-3723.

APPENDIX A: SYNTHETIC METHODS FOR MOF LINKERS

Figure A1, Compounds **2**-**6** were synthesized in order to evaluate them as possible replacements for the bipyridine (bpy) **1** linkers in Pillared Paddlewheel Frameworks, both as single MOF crystals or as films. Compounds **2**[168] and **3**[169] were specifically synthesized to examine them for possible substitution reactions with the PPF-5 films that Vitali had prepared with layer by layer (LBL) approach (compound **5** could also be useful here as it has good solubility). Compounds **4**[170] and **5**[171] were prepared for film growth studies. Compound **5** (considerably more soluble than **4**[170]) failed to yields films.

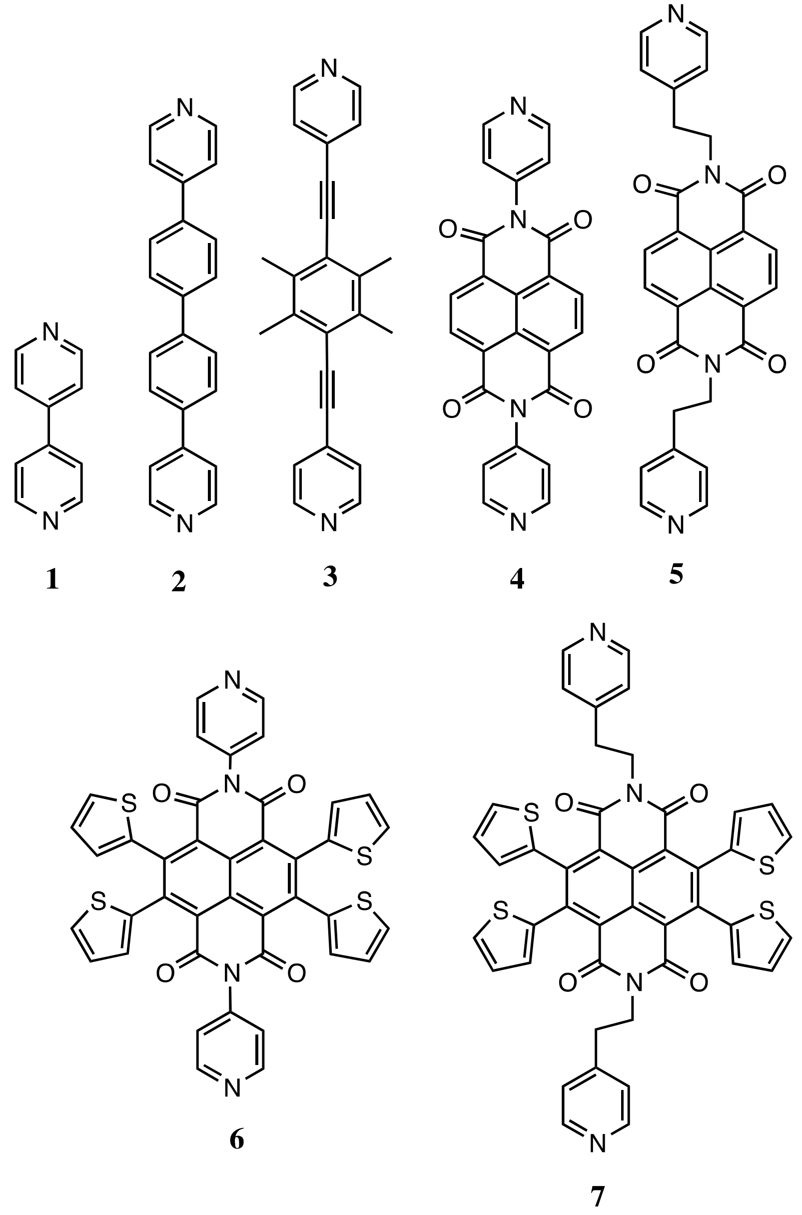

Figure A 1. Bipyridine based molecules for use as pillars in PPF MOFs

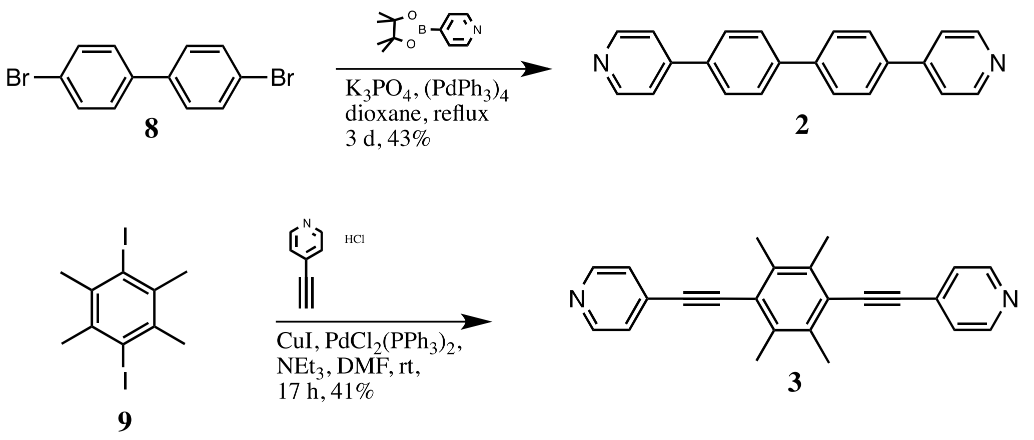

Scheme 1. Synthetic Approach for "extended" bipyridine molecules **2**[168] and **3**[169]

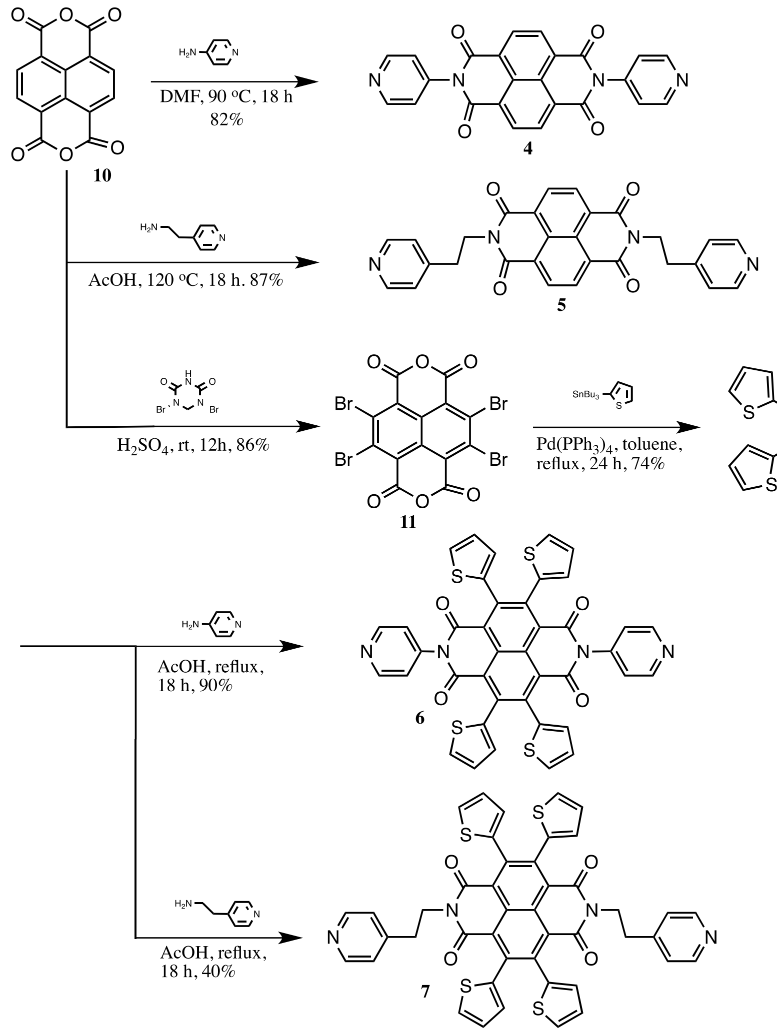

Scheme 2. Synthetic Approach for DPNI based pillars **4**[170], **5**,[ref] **6** and **7**

Synthetic Approach towards **6** and **7**.

2,3,6,7-Tetrabromo-1,4,5,8-naphthalenetetrqacarboxylic Acid (**11**) was prepared in 86% yield by treating 1,4,5,8-naphthalenetetracarboxylic acid dianhydride (**10**) with dibromoisocyanuric acid in oleum.[172] Stille coupling between **11** and 2-tributylstannyl-thiophene gave 2,3,6,7-tetra-(2-thienyl)-1,4,5,8-naphthalenetetracarboxylic acid dianhydride (**12**)[173] in 74% yield. Imidization was then performed with 4-aminopyridine and 4-(2-aminoethyl)-pyridine as follows:

N,N'-Di-(4-pyridyl)-2,3,6,7-tetra-(2-thienyl)-1,4,5,8-naphthalenetetracarboxydiimide (6). Glacial acetic acid (3 mL) was added to of 2,3,6,7-tetra-(2-thienyl)-1,4,5,8-naphthalenetetracarboxylic acid dianhydride (**12**) (0.024 g, 0.0402 mmol) and 4-aminopyridine (0.041 g, 0.436 mmol) and the mixture was refluxed under argon for 18h after which time the solvent was removed *in vacuo*. At this time $CHCl_3$ was added but the compound was found to not be very soluble in $CHCl_3$. The $CHCl_3$ was removed *in vacuo* and the solid residue was layered with MeOH and placed in the fridge. The soluble fraction was carefully removed with a pipette, $CHCl_3$ (to aid MeOH removal) was added and the solvents were removed *in vacuo* to obtain 0.0272 g of (**6**) as a red solid. Compound was highly insoluble and not characterized.

N,N'-Di-[(4-(2-aminoethyl)-pyridyl)]-2,3,6,7-tetra-(2-thienyl)-1,4,5,8-naphthalenetetracarboxydiimide (6). Glacial acetic acid (25 mL) was added to of 2,3,6,7-tetra-(2-thienyl)-1,4,5,8-naphthalenetetracarboxylic acid dianhydride (**12**) (0.279 g, 0.467 mmol) and 4-(2-aminoethyl)-pyridine (0.573 g, 4.67 mmol) and the mixture was refluxed under argon for 18h after which time the solvent was removed *in vacuo*. The residue was dissolved in $CHCl_3$ (50 mL) and washed with sat. NH_4Cl (2 x 50 mL), sat. $NaHCO_3$ (50 mL), dried (Na_2SO_4), filtered and the solvents removed *in vacuo* to obtain 0.542 g of crude material. Silica gel chromatography, eluting with 50:50:1 (v:v:v) $CHCl_3$:EtOAc:MeOH (200 mL), 50:50:3 (v:v:v) $CHCl_3$:EtOAc:MeOH (200 mL) and then 50:50:5 (v:v:v) $CHCl_3$:EtOAc:MeOH (until done) gave 0.156g of product with trace impurities, as judged by NMR. The compound was recrystallized from MeOH to obtain 0.136 g (40%) of **7**. **^{1}H NMR** (500 MHz, $CDCl_3$, 298 K): δ 8.45 (d, J = 5.8 Hz, 4H); 7.40 (d, J = 5.0 Hz, 4H); 7.10 (d, J = 5.7 Hz, 4H); 6.98 (dd, J = 3.6 Hz each, 4H); 6.60 (d, J = 3.4 Hz, 4H); 4.25 (t, J = 7.5 Hz, 4H); 2.89 (t, J = 7.5 Hz, 4H).

Synthetic Approach towards **15** and **16**.

Molecules **14** (BT-TT-BT), **15** (BT) and **16** (TT) are being developed in order to utilize them in a MOF-74 type framework. These molecules are shown in Figure 2. **13** was prepared externally by BroadPharm under contract and then cleaved at SNL (by Ryan utilizing his 1. TFA/CH_2Cl_2, 2. NaOH, THF/H_2O, route). The synthetic route to compound **15** has been demonstrated but sufficient quantities of this still need to be made from the protected molecule **18**, which has been prepared in multi-gram quantities. Ryan's procedure for the double de-protection to prepare **15** failed as significant decomposition occurs *prior* to debenzylation in the TFA/CH_2Cl_2 step. De-benzylation occurs fully and the addition of 20 equivalents of thioanisole failed to prevent this decomposition. While this is somewhat unexpected the electronics of this molecule are likely quite different than that of the BT-TT-BT, due to the presence of only the strongly electron withdrawing BT group between the hydroxybenzoates. This notion is consistent with that fact that the TFA reaction seems to be less rapid for this molecule then as reported in the literature. Hence, the alternate, effective, two step procedure (hydrolysis followed by TMSI induced debenzylation was developed. The TT molecule **24** has been synthesized but needs to be purified. It is anticipated that Ryan's cleavage methodology would be the most straightforward method of de-protection for this molecule.

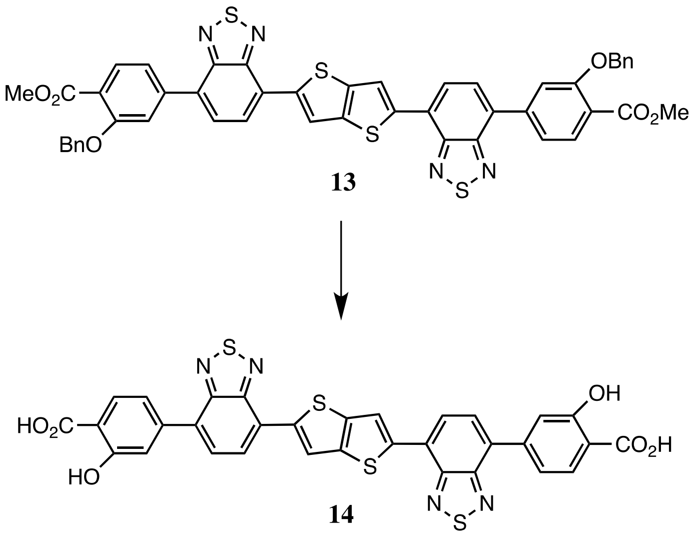

13

14

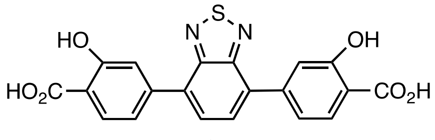

15

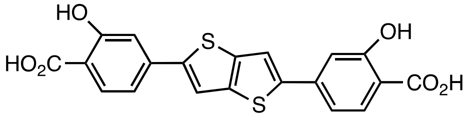

16

Figure A 2. Hydroxybenzoic acid based molecules for use as pillars in MOF-74 type structures

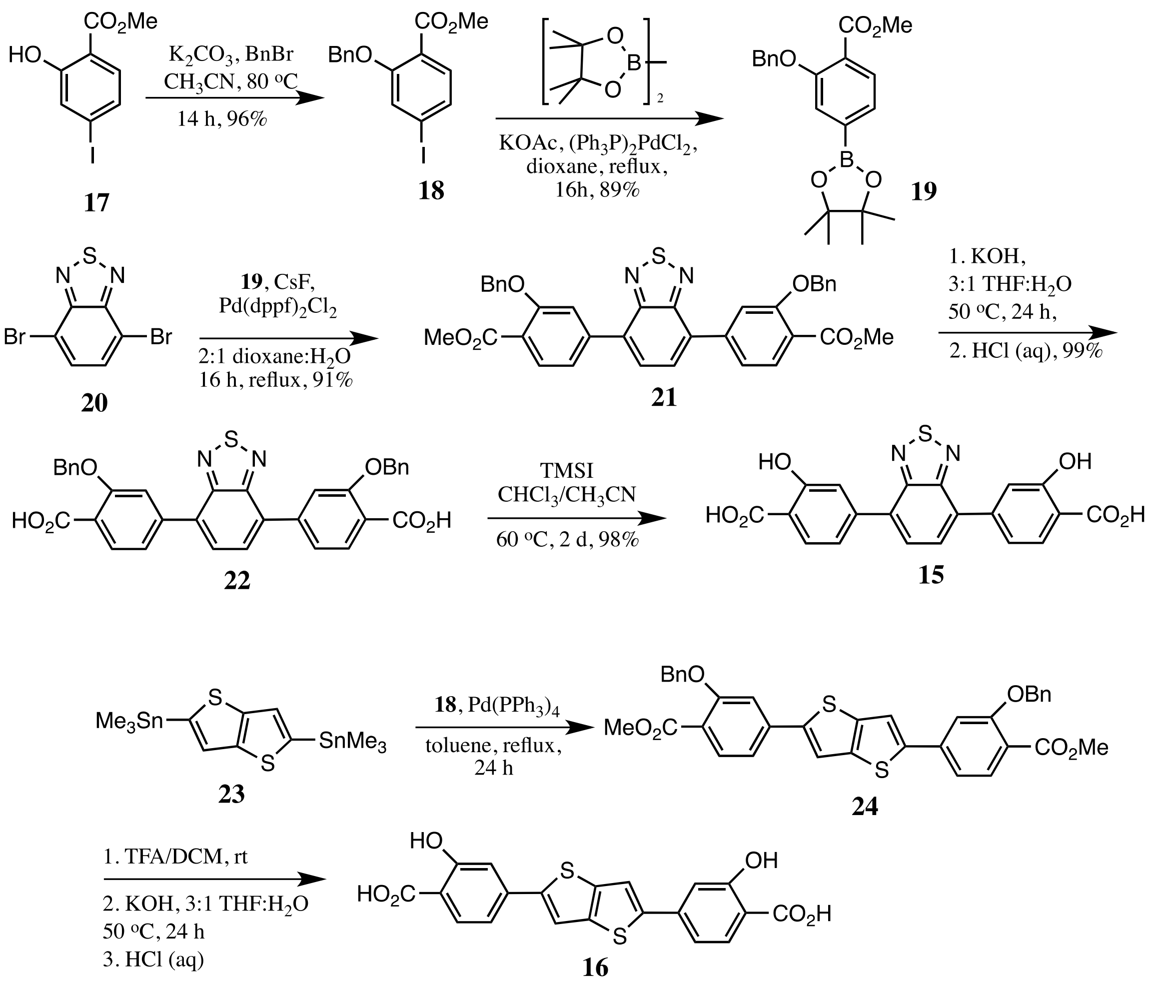

Scheme 3. Synthetic Approach for hydroxybenzoic acid based pillars **12** and **13**

Methyl 2-(benzyloxy)-4-(4,4,5,5-tetramethyl-1,3,2-dioxaborolan-2-yl)benzoate (**16**) was prepared according to previously reported procedures.[81]

*Dimethyl 4,4'-(benzo[c][1,2,5]thiadiazole-7,4-diyl))-bis(2-(benzyloxy benzoate)) (**18**).* 4,7-dibromo-5,6-benzo[*c*][1,2,5]thiadiazole **17** (2.013 g, 6.85 mmol) **,** methyl 2-(benzyloxy)-4-(4,4,5,5-tetramethyl-1,3,2-dioxaborolan-2-yl)benzoate (**16**) (5.55 g, 15.1 mmol), CsF (6.22, 40.9 mmol) and $PdCl_2$(dppf) (0.554 g, 10 mol % total) were combined with a degassed solution of dioxane:H_2O (v/v, 2:1, 150 mL) and heated at reflux under argon 16 h. The reaction solvents were removed *in vacuo* and the residue taken up in hot hexanes and filtered through a plug of celite

. The hexane solution was then washed with water (100 mL), sat. NaCl (100 mL), dried (Na_2SO_4), filtered and then the solvents were removed in *vacuo*. The compound was purified on silica gel with EtOAc/hexanes gradient elution to provide 3.85 g (87%) of the product as a yellow solid. **^{1}H NMR** (500 MHz, $CDCl_3$, 298 K): δ 8.01 (d, J = 5.0 Hz, 2H); 7.80 (s, 2H); 7.75 (s, 2H); ~ 7.58-7.45 (m, 6H); 7.42 (t, J = 7.5 Hz, 4H); 7.34 (t, J = 7.4 Hz, 2H); 5.31 (s, 4H); 3.96 (s, 6H).

*4,4'-(benzo[c][1,2,5]thiadiazole-7,4-diyl))-bis(2-(benzyloxy benzoic acid)) (**19**).* Dimethyl 4,4'-(benzo[c][1,2,5]thiadiazole-7,4-diyl))-bis(2-(benzyloxy benzoate)) (**18**) (0.0264 g, 0.0428 mmol) and KOH (~ 85%, 0.0207 g, 0.314 mmol) were added to a solution of THF (3 mL) and water (1 mL) which was then heated at 50 °C for 24 h). The solvents were removed *in vacuo*, the residue dissolved in DI H_2O (50 mL), precipitated with the addition of 6N HCl until pH < 2 and then extracted into EtOAc (1 x 50 mL, 2 x 25 mL). The combined EtOAc extracts were dried (Na_2SO_4), filtered and the solvent removed *in vacuo* to obtain 0.0249 g (99%) of **19** as a yellow solid. **^{1}H NMR** (500 MHz, $CDCl_3$, 298 K): δ 10.70 (br s, 2H); 8.38 (d, *J* = 8.2 Hz, 2H); 7.99 (s, 2H); 7.90 (s, 2H); 7.68 (d, *J* = 8.2 Hz, 2H); 7.55-7.40 (m, 10H); 5.44 (s, 4H).

Note: this compound is not really that soluble in EtOAc, so on scale up it would be better to precipitate the compound as above and then isolate by vacuum filtration. 9:36 AM This solid could then be dissolved in THF, dried w/ Na_2SO_4 and then filtered to obtain the product.

*4,4'-(benzo[c][1,2,5]thiadiazole-7,4-diyl))-bis(2-(hydroxy benzoic acid)) (**12**).* Trimethylsilyl iodide (0.0703 g, 0.351 mmol) was added to 4,4'-(benzo[c][1,2,5]thiadiazole-7,4-diyl))-bis(2-(benzyloxy benzoic acid)) (**19**) in CH_3CN (anhydrous, 1 mL) and $CHCl_3$ (anhydrous, ~ 2 mL) under argon. The reaction was fitted with a reflux condenser and heated at 60 °C under argon for 2 d after which time it was cooled to rt, MeOH was added and it was allowed to stir for 1 h. The solvents were removed *in vacuo* and the residue was suspended in MeOH (~3 mL) and sat NaHCO3 (~ 0.5 mL) and stirred for a few minutes before diluting with H_2O (~ 80 mL) to obtain a clear solution. The aqueous solution was extracted with hexanes (2 x 30 mL) and then the product was precipitated from the aqueous solution with the addition of 6 N HCl until a pH < 2 was achieved. The yellow solids were isolated by vacuum filtration, rinsed with water and then re-dissolved in EtOAc, dried (Na_2SO_4) and filtered. The solvents were removed *in vacuo* to obtain the 0.0172 g (98%) of the product as a yellow solid. **^{1}H NMR** (500 MHz, DMSO, 298 K): δ 8.06-8.0 (m, 2H); 7.93-7.86 (m, 2H); 7.63-7.52 (m, 2H); 7.52-7.44 (m, 2H). Note: Spectra was not well resolved and at low concentration – use d-THF as NMR solvent.

Note: This compound is more soluble in THF than EtOAc, for scale up this should be used to isolate the solid as for the precursor.

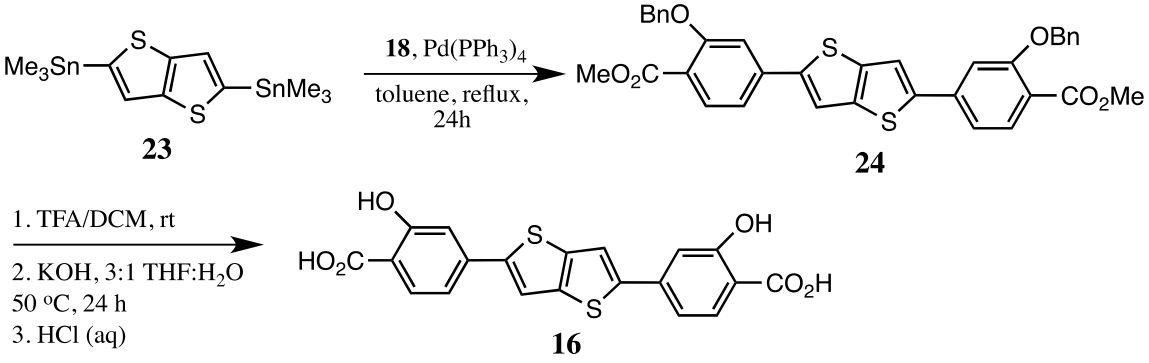

Scheme 4. Synthetic Approach for hydroxybenzoic acid based TT pillar **16**.

*Dimethyl 4,4'-(thieno[3,2-b]thiophene-2,5-diyl)-bis(2-(benzyloxy benzoate) (**24**).*
Methyl 2-(benzyloxy)-4-iodobenzoate (**14**) (0.892 g, 2.42 mmol), 2,5-bis(trimethylstannyl)thieno[3,2-*b*]thiophene (**20**) (0.505 g, 1.08 mmol) and Pd(PPh$_3$)$_4$ (0.130 g, 0.1125 mmol, 10 mol %) were added to toluene (anhydrous, 40 mL) and then heated at reflux under argon for 24 h after which time the reaction was cooled to rt, quenched with the addition of 2N HCl (aq.) and extracted twice with $CHCl_3$ (1 x 50 mL, 1 x 25 mL) using sat. NaCl to prevent an emulsion as needed. The combined $CHCl_3$ layers were washed with 2 N HCl, sat. $NaHCO_3$, and then dried (Na_2SO_4), filtered and then dried *in vacuo* to obtain 0.912 g of crude product. 1H NMR indicates the product is the predominate species. *NEED TO PURIFY.*
^{1}H NMR (500 MHz, $CDCl_3$, 298 K): δ 7.90 (d, J = 8.0 Hz, 2H); 7.57-7.54 (m, 6H); 7.42 (t, J = 7.6 Hz, 2H); 7.34 (t, J = 7.3 Hz, 2H); 7.28-7.24 (m, 4H).

APPENDIX B: PUBLICATIONS AND PRESENTATIONS

Publications

V. Stavila, A. A. Talin, and M. D. Allendorf "MOF-Based Electronic and Opto-Electronic Devices," *Chem. Soc. Rev.*, 2014, 43 (16), 5994 - 6010.

M. E. Foster, J. D. Azoulay, B. M. Wong, M. D. Allendorf "Novel Metal-Organic Framework Linkers for Light Harvesting Applications: A First-Principles Perspective," *Chem. Sci.* **5** (2014) 2081.

K. Leong, M. E. Foster, B. M. Wong, E. D. Spoerke, D. Gough, J. C. Deaton, M. D. Allendorf "Energy and Charge Transfer by Donor-Acceptors Pairs Confined in a Metal-Organic Framework: A Spectroscopic and Computational Investigation," *J. Mater. Chem. A*, **2** (2014), 3389.

Van Gough, Dara; Lambert, Timothy; Wheeler, David; Rodriguez, Mark; Allendorf, Mark; Spoerke, Erik "Controlled Nucleation and Growth of Pillared Paddlewheel Framework Nanostacks onto Chemically Modified Surfaces," *ACS Appl. Mater. Interfaces* **6** (2014), 1509.

A. Alec Talin, Andrea Centrone, Paul Haney, Vitalie Stavila, Alexandra C. Ford, Michael E. Foster, R. Adam Kinney, Veronika Szalai, Heayoung P. Yoon, François Léonard, Mark D. Allendorf "Tunable Electrical Conductivity in Metal-Organic Framework Thin Film Devices," *Science*, **343** (2014), 66.

K. Leong, M. E. Foster, B. M. Wong, E. D. Spoerke, D. Gough, J. C. Deaton, M. D. Allendorf "Nano-Ordering of Donor-Acceptor Interactions Using Metal-Organic Frameworks as Scaffolds" *Photovoltaics for the 21st Century 9, ECS Transactions,* **58** (2013), 21.

Invited presentations

M. D. Allendorf "Luminescent metal-organic frameworks (MOFs): a Nanolaboratory for Photophysics," MIT Center for Excitonics Lecture Series," Cambridge, Massachusetts, February 7, 2012.

M. D. Allendorf "The Power of Empty Space," *Valley Study Group,* Pleasanton, CA, June 13, 2012.

M. D. Allendorf "The Power of Empty Space: Manipulating MOFs for Device Applications," Dept. of Chemistry, Washington University, St. Louis, MO Oct. 25, 2012.

M. D. Allendorf "The Power of Empty Space: Manipulating MOFs for Device Applications," Dept. of Physics, University of Missouri, St. Louis, MO, Oct. 26, 2012.

M. D. Allendorf "Creating donor-acceptor interfaces for excitonic devices using nanoporous metal-organic frameworks," *Electronic Materials and Applications 2013 Conference,* Orlando, FL, January 23-25, 2013.

M. D. Allendorf "Manipulating MOFs for Nanoparticle, Thin Film, and Device Fabrication," University of South Florida, Tampa, FL, January 25, 2013.

M. D. Allendorf, “Nanoporosity and the Welcome Guest: Developing Metal-Organic Frameworks for Electronic Device Applications,” Dept. of Materials Science, Univ. of Cambridge, Cambridge, U.K. Sept. 9, 2013.

M. D. Allendorf, A. A. Talin, J. A. Greathouse, T. N. Lambert, E. D. Spoerke, V. Stavila, B. M. Wong “The Power of Empty Space: Metal-Organic Frameworks as Electronic Materials,” Keynote lecture, *EuroMat 2013*, Seville, Spain, Sept. 9 – 13, 2013.

E.D. Spoerke, J.S. Wheeler, S. Wolf, D.V. Gough, M. E. Foster, K. Leong-Hau, V. Stavila, T.N. Lambert, and M.D. Allendorf. “Optoelectronic “Tinker Toys”:Supramolecular Nanocomposite Frameworks for Next Generation Photovoltaics.” *Composites at Lake Louise,* Lake Louise, Alberta, Canada. Nov. 2013.

M. D. Allendorf “The Power of Empty Space: Adventures in Chemistry at a National Laboratory,” Whittier College, Whittier, CA Feb. 21, 2014.

A. Alec Talin, Michael E. Foster, Vitalie Stavila, Alexandra Ford, Farid El Gabaly, François Léonard, Mark D. Allendorf “Molecule@MOF: A New Class of Electronic Materials,” invited presentation, Fall Electrochemical Society meeting, Cancun, Mexico, Oct. 2014.

M. D. Allendorf “Emergent Properties Using the Guest@MOF Concept,” invited presentation, *Metal-Organic Frameworks: Experiments and Simulations,* Telluride, CO, July 7 – 11, 2014.

M. D. Allendorf “Pleasures and Pitfalls of Guest Molecules in MOFs,” invited presentation, *Characterization of Nanoporous Materials workshop,* Stanford University, Aug. 8, 2014.

M. D. Allendorf “Nanoporosity and the Welcome Guest: Metal-Organic Frameworks as Active Components of Electronic Devices,” invited presentation, ACS Fall 2014 meeting, San Francisco, CA, Aug. 10 – 14, 2014.

M. D. Allendorf, A. A. Talin, M. E. Foster, V. Stavila, F. Leonard “Molecule meets MOF: bridging the gap between organic and inorganic electronic materials,” invited presentation, SPIE Optics + Photonics conference, San Diego, CA Aug. 17 – 21, 2014.

Contributed presentations

M. D. Allendorf, M. Foster, D. Gough, T. N. Lambert, K. Leong, S. T. Meek, E. D. Spoerke, B. Wong “Controlling donor-acceptor interfaces in excitonic devices using nanoporous metal-organic framework templates,” *ACS Fall 2012 Meeting,* Philadelphia, PA, August 20–23, 2012.

Kirsty Leong, Scott T. Meek, Bryan Wong, Erik D. Spoerke, Timothy N. Lambert, and Mark D. Allendorf "Highly Ordered Crystalline Nanoporous Frameworks for Nano-Heterojunction Photovoltaics," Nominated for Best Poster, Spring 2012 MRS Meeting, San Francisco, CA, April 2012.

Michael Foster, Bryan Wong, Kirsty Leong, Scott T. Meek, Timothy N. Lambert, Erik D. Spoerke, Mark D. Allendorf “Electronic Properties of Photovoltaic Metal Organic Frameworks from First-principles Calculations,” poster presented at Spring 2012 MRS meeting, San Francisco, CA, April 2012.

Michael E. Foster, Kirsty Leong, Bryan M. Wong, Erik D. Spoerke, Dara Gough, Scott T.Meek, Timothy N. Lambert, and Mark D. Allendorf“First-principles investigation of the energetics of infiltration and charge/energy transfer within metal-organic frameworks," presented at Spring 2013 MRS meeting, San Francisco, CA.

Kirsty Leong, Michael E. Foster, Bryan M. Wong, Erik D. Spoerke, Dara Gough, Scott T.Meek, Timothy N. Lambert, and Mark D. Allendorf "Nanoscale Phase Segregation of a Molecular System using Metal-Organic Framework for Energy Transfer," presented at Spring MRS meeting, San Francisco, CA, April 2013.

M. D. Allendorf, A. C. Ford, M. E. Foster, F. Leonard, K. Leong, A. A. Talin, B. M. Wong, D. Van Gough, E. D. Spoerke, J. C. Deaton "Nano-Ordering of Donor-Acceptor Interactions Using Metal-Organic Frameworks as Scaffolds," Fall Electrochemical Society meeting, San Francisco, CA, Oct. 2013.

E. D. Spoerke, D.V. Gough, J.S. Wheeler, D. R. Wheeler, T.N. Lambert, V. Stavila, M.D. Allendorf. "Molecular 'Popoids': Assembling Functional Supramolecular Nanocrystal Films on Chemically-Modified Surfaces." *Electronic Materials and Applications 2014*, Orlando, FL Jan. 2014.

E.D. Spoerke, D. V. Gough, J.S. Wheeler, S. Wolf, M. Foster, K. Leong, V. Stavila, and M.D. Allendorf. "Supamolecular Building Blocks for Hybrid Photovoltaics." *Electronic Materials and Applications 2014*, Orlando, FL Jan. 2014.

E.D. Spoerke, S. Wolf, J.S. Wheeler, D. V. Gough, T.N. Lambert, M. E. Foster, K. Leong-Hau, V. Stavila, and M.D. Allendorf. "Nanoporous Metal-Organic Frameworks: Functional Supramolecular Materials for Next Generation Dye-Sensitized Solar Cells." Materials Research Society Meeting, San Francisco, CA, April 2014.

Michael E. Foster, Jason D. Azoulay, and Mark D. Allendorf "Novel Metal-Organic Framework Linkers for Light Harvesting Applications: A First Principles Prospective," presented at Spring MRS meeting, San Francisco, CA, April 2014.

Technical Advances and Patent Applications

"Tunable Electrical Conductivity in Metal-Organic Framework Thin Film Devices Devices," A. A. Talin, M. D. Allendorf, V. Stavila, F. Leonard, non-provisional patent application.

"Multiaxis Sensing Using Electrically Conducting MOFs," provisional patent application.

"Reconfigurable Electronics Using Conducting Metal-Organic Frameworks," M. D. Allendorf, A. A. Talin, F. Leonard, V. Stavila, provisional patent application.

DISTRIBUTION

1	MS0734	Tim Lambert	6124
2	MS0734	Anthony Martino	6124
3	MS1411	Paul Clem	1816
4	MS1411	Erik Spoerke	1816
5	MS9052	Dan Dedrick	8367
6	MS9161	Sarah Allendorf	8650
7	MS9161	Francois Leonard	8656
8	MS9161	Neville Moody	8651
9	MS9161	Vitalie Stavila	8367
10	MS9161	John Sullivan	8656
11	MS9161	Alec Talin	8656
12	MS9403	Mike Foster	8223
13	MS9403	Adam Rowen	8223

1	MS0899	Technical Library	9536 (electronic copy)

For LDRD reports, add:

1	MS0359	D. Chavez, LDRD Office	1911

For CRADA reports add:

1	MS0115	OFA/NFE Agreements	10012

For Patent Caution reports, add:

1	MS0161	Legal Technology Transfer Center	11500

Sandia National Laboratories